Космични изследвания в България

Том 1 · София · 1978

Българска академия на науките

Address

Space Research in Bulgaria
Central Laboratory for Space Research
Bulgaria, 1000 Sofia, Blvd Rouski 1

Адрес

Космични изследвания в България
Централна лаборатория по космични изследвания
1000 София, бул. „Руски" № 1

Издателство на Българската академия на науките

629.13(05)

Коректор Техн. редактор *Д. Калинова* 9532422211
Изд. индекс 6587 Дадена за набор на 6. II 1978 г. Подп. за печат на 25. VII. 1978 г. Код 19 2332-4-78
7000×1000/16 Тираж 500 Печ. коли 6,50 Изд. коли 8,42 Цена 1,01 лв.
Печатница на БАН — 1113 София, ул. „Акад. Георги Бончев" Пор. 132

Space Research in Bulgaria

Volume 1 · Sofia · 1978

Bulgarian Academy of Sciences

Contents

Содержание

"Space Research in Bulgaria" — Its Goals, Scope and Content

Intelligent and studious, the Bulgarian people have for thousand of years been interested in the sky, the stars and in the phenomena related to them. The millenary-long history of the Protobulgarian perfect Calendar and its profound and broad astronomical foundations are only part of the vast astronomical heritage of ancient Bulgaria. The Bulgarian nation has developed this heritage for almost 1300 years now and after 1957 it established the Bulgarian participation in various modern fields of space research. The scientific results obtained in Bulgaria in the field of ionospheric physics, for instance, are well known and appreciated by contemporary science, and the investigations in such fields as cosmic rays, the magnetosphere, the hard component of the interplanetary medium, and the Sun, are advancing well in our country. The active participation by Bulgaria in the Intercosmos Programme has resulted in the launching of our equipment in space (Intercosmos-8, 12, 14 satellites, Vertical-3, 4, 6 rockets, several meteorological rockets) and has enabled the Bulgarian specialists to use abundant data from these and other space experiments.

The development of the space research in Bulgaria resulted in the setting up of the Group on Space Physics in 1969, which grew into the Central Laboratory for Space Research in 1973. The scientists of this Academic Institution have frequently contributed to leading space journals. The expansion of their activities necessitated the issue of an independent Bulgarian space journal which is already in the hands of its honourable readers. This is the first volume of the subject series *Space Research in Bulgaria.* The purpose is to offer selected scientific papers by Bulgarian authors in the following main fields:

1. Space Physics (physics of the top-side atmosphere, magnetosphere, heliophysics, cosmic rays, physical problems of the interplanetary substance, outer-atmospheric astronomy, planetary morphology, geology and geophysics etc. — data obtained by in situ measurements.

2. Techniques and means of the space equipment and problems of the space instrument design.

3. Remote sensing — aero- and space techniques for Earth survey and results from their application in theoretical and practical branches.

4. General and fundamental problems of the space investigation.

The Editorial Board will be pleased to accept original papers from foreign authors, priority being given to studies within the frameworks of the Intercosmos Programme and to authors from countries having bilateral agreements with Bulgaria.

We hope that this issue would, partially at least, reflect the modest though meaningful contribution by Bulgarian science and technology in the spatial advance of our civilization.

Professor *Kiril B. Serafimov*
(Editor-in-Chief)

BULGARIAN ACADEMY OF SCIENCES

SPACE RESEARCH IN BULGARIA, 1

Sofia · 1978

Ion Density Measurement within the Equatorial Region

K. B. Serafimov, I. S. Kutiev, J. F. Arsov, Ts. P. Dachev, G. A. Stanev, G. L. Gdalevich, V. V. Afonin, V. Gubskiy, V. Ozerov, J. Schmilauer

I. Introduction

The study of electron and ion density distribution around the magnetic equator is of considerable importance in clarifying the methods of magnetic, solar-ionizing and dynamic control of the important ionospheric processes. The well-known equatorial anomaly in the latitudinal distribution of the charged particles has been the object of studies for 30 years now [1, 2, 3, 4, 5, 6, 7, 8, 10]. The investigations continue, and further regularities and specificities of this phenomenon are being discovered. For instance, the equatorial anomaly existing at altitudes of 900—1200 km during the night and the separation of crests of proton and oxygen ion concentration has been proved in [8, 9], while in [11, 12, 13] the authors have studied the irregularities in the equatorial zone by probe methods. Considerable progress is to be observed recently in the field of theoretical investigations [7, 10] and in the related phenomenon of irregular ionizing structure [13]. However, we still do not possess sufficiently reliable experimental data about the conditions of formation and disappearance of the anomaly, particularly over the region of maximal electron concentrations in the *F*-region. We do not have sufficient information about the altitudinal manifestation of this anomaly either. The lack of data on the planetary distribution of electron and ion temperatures and on their temporal changes constitutes a major difficulty for all contemporary ionospheric models. That is why, the electron and the ion concentration measurements and the electron temperature measurements performed by the Intercosmos-8 satellite whose orbit crossed the equatorial regions at various moments of the day is of considerable interest.

II. Results from Ion Density Measurements

Ion traps described in [15, 18], Langmuir probe [16, 18], radiofrequency electron temperature probe [17], and improved electronic equipment [18] have been used on board the Intercosmos-8 satellite. This satellite performed measurements of the equatorial latitudes at geographical longitudes from 150° W to 60° E, as the transits over the magnetic equator took place at afternoon and night hours. The measurement conditions are presented in detail in Table 1.

The resulting measurements are conventionally separated into two groups, mainly from the point of view of the local time for the equatorial cross. The first group is related to the afternoon period of up to 18^h30^m LT and the second one is related to the night period (after 18^h30^m LT).

The ion concentration for the transits crossing the equator between 17^h00^m LT at altitudes of 308 km to 360 km under quiet magnetic conditions (K_p-3) are presented on Fig. 1. The distributions demonstrated are typical of the day period and coincide with the data already known about the equatorial anomaly [6, 8, 9, 29]. The two characteristic minima — $15° \div 20°$ north and south of the equator and a clearly expressed minimum in the region of the geomagnetic equator can be seen on the Figure. A definite longitudinal effect can also be observed. In order to characterize this effect we divided the longitudinal interval into two subintervals: *A* (150° W) 70° W) and *B* (70° W, 0° W). In the first subinterval the maxima are located symmetrically to the geomagnetic equator at $\pm 15°$. In subregion *B* there exists a definite deviation from the known development of the equatorial anomaly, since the trend for the south maximum is to shift towards the equator from $-15°$ to $-5°$, while the north maximum becomes considerably lower. The value of ion density in this maximum is approximately equal to the concentration of the minimum in subregion *A*. In general, the circumequatorial distribution in subregion *B* approximates the one-maximal distribution similar to that in [27].

Fig. 2 shows characteristic data for the night group which includes the transits with local time of equatorial cross between 18^h30^m and 21^h30^m. The altitude of the equatorial cross in accordance with Table 1 is between 455 and 360 km as the satellite descends from the south to the north.

At these temporal and altitudinal conditions the general trend for the equatorial minimum is to disappear within a concentration decrease in the

Table 1

Measurement Conditions

Geomagnetic latitude (deg.)	Local time (h)					Altitude (km)					Zenith angle (degrees)				
	Transit number					Transit number					Transit number				
	2	96	202	296	344	2	96	202	296	344	2	96	202	296	344
—50	19^h13^m	1800	1610	1510	1455	654	608	572	502	447	79	73	57	48	43
0	21^h34^m	2007	1828	1703	1628	455	408	360	308	267	132	114	92	73	68
50	22^h57^m	2125	1947	1822	1750	263	245	220	209	206	157	143	125	108	106

crests (for the north one almost of one order, and for the south one — 2 to 3 times), while the concentration in the minimum almost keeps its value.

The main morphological peculiarities of subregion A are the following: in the western part ($\lambda > 110°$ W) the main maximum is located in the south

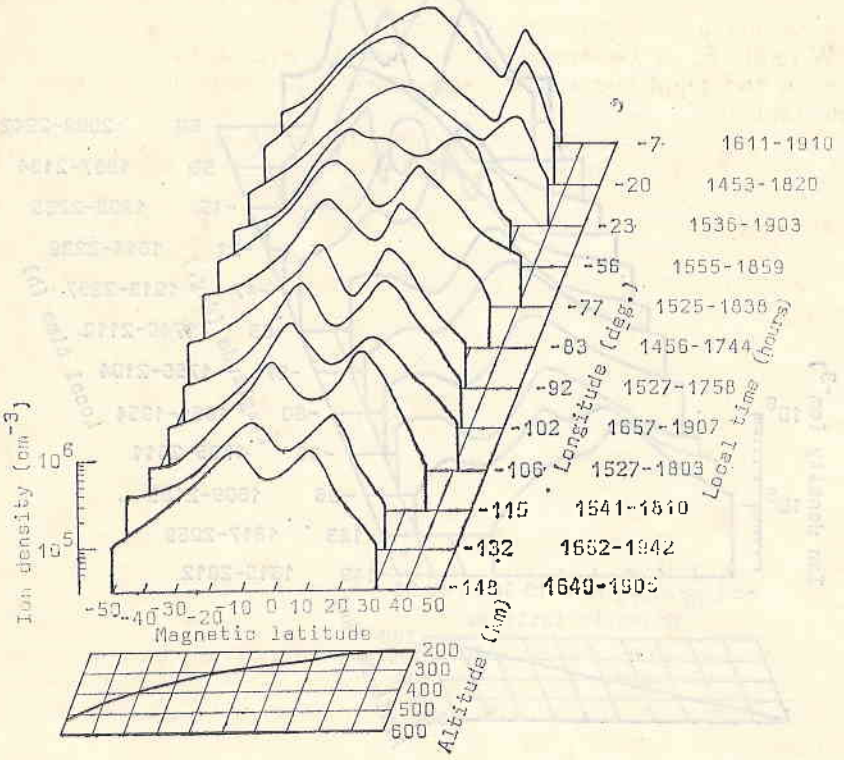

Fig. 1

hemisphere, and in the eastern part ($\lambda < 110°$—$120°$ W) the main maximum is located close to the equator. The north maximum almost disapears during this period. Because of the altitudinal decrease of the orbits, the north maximum recorded in subregion B probably is due to the satellite cross through the F maximum. The main maximum in subregion B shifts from the equator to the north to $\Phi = 15° \div 20°$ N. This main maximum comprises the whole latitudinal region from the equator to the designated boundary $\Phi = 15° \div 20°$ N. A well expressed irregular large-scale structure is to be observed in this subregion (and especially in its western part $-\lambda < 30°$ W). These irregularities are identified particularly in the region of the Brazilian magnetic anomaly. A similar behaviour has been described in [28], where a region between 60° W and 60° E with decreased concentration and large-scale irregularities has been sharply outlined.

At to transits between $\lambda = 55° \text{E} \div 60° \text{E}$, a well expressed bimaximal distribution of the ion concentration has been obtained. This fact shows that

the effects described in subregion B are of a local character and are influenced by magnetic field specificities.

The equatorial anomaly sections along the satellite orbit at day and night conditions represented here show clearly the influence of the magnetic

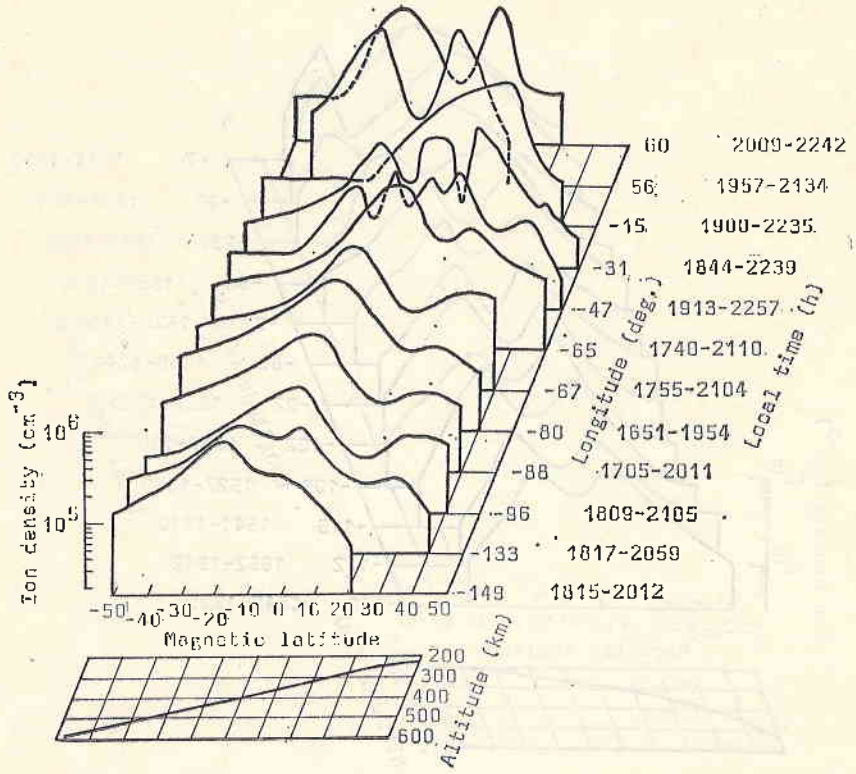

Fig. 2

field over the charged particles distribution. That can be seen particularly clear in the region of the Brazilian magnetic anomaly (about 60° W). By comparing Fig. 1 and Fig. 2 the conclusion is reached that the equatorial anomaly in the region under examination decays by 19^h00^m. In the region of the Brazilian magnetic anomaly, strongly expressed large-scale irregularities manifest themselves after 21^h00^m approximately.

III. Electron Temperature in the Equatorial Region

Fig. 3a shows the measurement results obtained by radiofrequency electron temperature probe in the interval of geomagnetic latitudes $\pm 40°$ in quiet magnetic conditions ($K_p<2+$, $\Sigma K_p=10+$). The temperature of the neutral particles T_n close to the equator (Jacchia-71 model) are shown on the lower side of the Figure. T_n-variations at this period do not exceed 20° K. Data shown on Fig. 3a relate to the morning hours $08^h00^m \div 11^h00^m$ LT, and data

in Fig. 3b relate to the night hours $20^h00^m \div 22^h00^m$ LT. Since the photoelectron flux and the electron concentration at $\chi = 85°$ attain the stationary day level [25], the results shown on Fig. 3a are characteristic of daytime, and those on Fig. 3b — for the night, since $\chi = 110°$.

During $08^h00^m \div 11^h00^m$ LT (Fig. 3a) in the geomagnetic equator region there exists a deep temperature trough near the geomagnetic equator with values close to T_n. T_e smoothly decreases to its approximation of a minimum.

Even when there exists a region with T_e independent on the latitude, its latitudinal spread does not exceed several degrees. The centre of the equatorial trough is shifted to a subsolar direction of about 5° from the equator. As seen from the Sun location with regard to the equatorial trough of T_e, it actually represents a geomagnetic effect. A certain assymetry of the trough form is obviously connected with the altitudinal variation of T_e and the local time changes. At some passes T_e-variations with "amplitudes" of $300° \div 400°$ K have been observed. These T_e-variations could be provoked either by kynetic effects — plasma heating and cooling at its transfer along the field lines from one hemisphere to the other [19], or by T_e-anisotropy [26]. At any rate, the minimum T_e values in the trough centre coincide with T_n in most cases, but at some passes at $300° \div 400°$ K $T_{e\min}$ exceeds T_n.

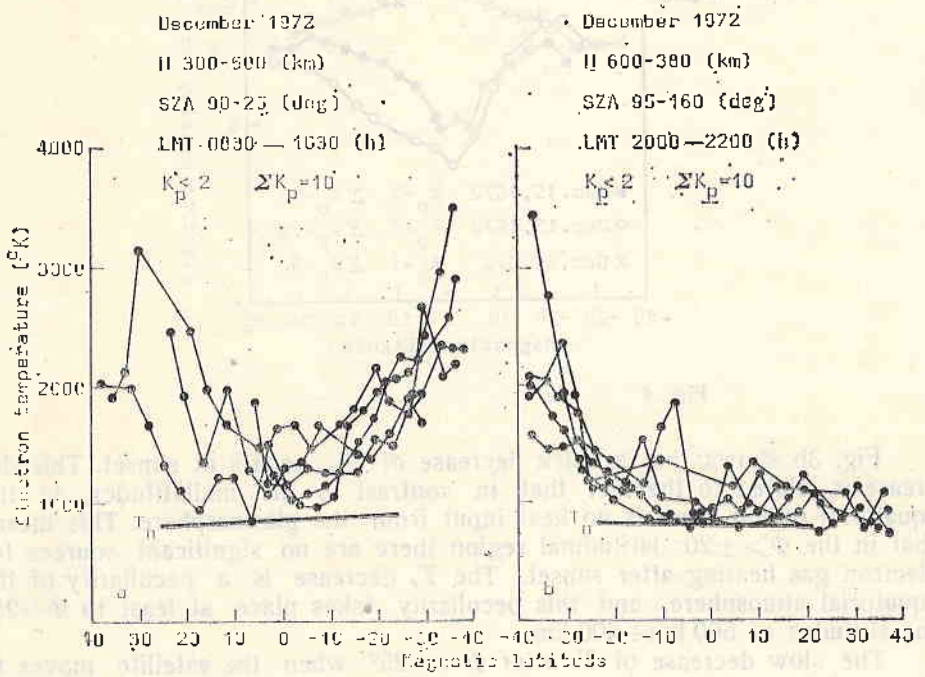

Fig. 3

Electron temperature in the trough is controlled by the ratio between the heat input and the value of n_i-concentration, which in this phase of the solar activity cycle at day is sufficiently high, for the difference between T_e and T_n should not exceed $300° \div 400°$ K.

At nightfall (Fig. 3b) T_e decreases fast from 2000°÷3000° K at $\Phi=-40°$ to 1200°±100° K at $\Phi=-25°$, and after that decreases monotonously to 900°±100° K at $\Phi=-40°$. The initial fast decrease of T_e takes place during 30^m LT. The sunset had occurred for the setellite at the represented passes in the latitudinal interval of 20°÷30°.

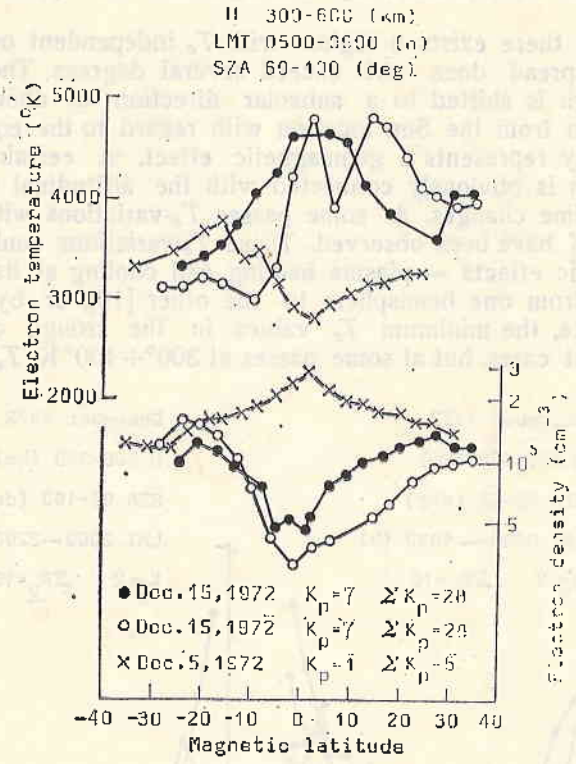

Fig. 4

Fig. 3b shows that a quick decrease of T_e occurs at sunset. This decrease is related to the fact that in contrast to the midlatitudes, in the equatorial region there is no heat input from the plasmasphere. This means that in the $\Phi>\pm20°$ latitudinal region there are no significant sources for electron gas heating after sunset. The T_e decrease is a peculiarity of the equatorial atmosphere, and this peculiarity takes place at least to $\Phi\approx25°$ for altitudes of 500 km÷600 km.

The slow decrease of T_e after $\Phi=-25°$ when the satellite moves to the north is probably connected with the altitudinal decrease. Moreover, since T_e is close to T_n, a T_n-decrease of about 100° K at the transition from 20^{h}00^m LT and $\Phi=-30°$ in the summer hemisphere to 22^{h}00^m LT and $\Phi=+30°$ in the winter hemisphere (Jacchia-71) plays a certain role.

The behaviour of T_e and n_e in the transition time from night to day (5^{h}00^m÷9^{h}00^m LT, i. e. during the sunrise period and the first hours after it),

is shown on Fig. 4. This behaviour has been established according to Langmuir probe data. The Figure represents the results from three satellite passes — one performed in continuous quiet magnetic period and two passes in a magnetically strongly disturbed period. The main characteristic of these curves is the high T_e value. $T_e > 2000°$ K in quiet conditions over the geomagnetic equator at 500 km and attains 3800° K in a magnetically disturbed period. Moreover, both in quiet and disturbed periods there exists clearly expressed, up to the smallest details, an inverse proportional dependence between T_e and n_e. T_e considerably exceeds T_n in the geomagnetic equator region at $H = 400 \div 500$ km. Therefore at this time the heat input exceeds the electron cooling by the ions (at these altitudes mainly O^+, which decreases sharply). During this time the heat input has already attained the stable day level and after $2 \div 3$ hours (Fig. 3a) T_e again decreases to values close to T_n.

The midlatitudes of the northern hemisphere have been crossed by the satellite at the night before sunrise (Fig. 4 — $\chi > 100°$). At that time T_e should be close to $T_n < 1000°$ K (Fig. 3b), because the heating influx from the magnetosphere at the end of the night before sunrise cannot ensure a considerable difference $T_e - T_n$ [20]. Therefore, the values of $T_e > 2000°$ K at midlatitudes in the north hemisphere in the given case are determined by the only significant heating source — the photoelectron flux from the magnetically conjugated region of the ionosphere, which was lit up during the time ($\chi < 87°$).

Discussion

The time development of the equatorial anomaly for the altitudinal and longitudinal regions examined shows a decay of the equatorial trough after about 19^h00^m LT. It has been found in [6] that over the American continent it is difficult to determine the period of the equatorial anomaly decay because of the appearance of intense F-spread after 22^h00^m. The beginning of the anomaly decay obtained here clarifies this problem, though only for the altitudinal part examined. In 3a we have shown that the equatorial anomaly for altitudes over 900—1200 km remains during night for the regions around the Brazilian magnetic anomaly. Therefore, a complete clarification of the temporal and spacial conditions for the equatorial anomaly decay calls for measurements in the whole region of the maximal electron concentration of the F-region.

The deviation of the equatorial trough in the ion density from the geomagnetic equator is connected mainly with the deviations of the real geomagnetic field from the dipole one used in this study.

In the region over the Brazilian magnetic anomaly after sunset an intensification of the irregular structure has been determined which is connected with the ionizing influence of the intense corpuscular fluxes [30]. The electron temperature T_e in the geomagnetic equator region at altitudes higher than the F_2-region maximum to at least 600 km during the winter of 1972-1973 for more than 50 days, excluding the several hours near the sunrise period, is close to the temperature of the neutral particles. During the day, in the latitudinal T_e-variations this decrease takes the form of a trough with a minimum, shifted at $\approx 5°$ in the subsolar direction and expand-

ing to 20°÷30° on both sides. During nighttime in the altitudinal interval of 300-500 km $T_e = T_n$. Because of the absence of heating sources in the latitudinal variation of T_e, there exists a plateau $T_e = T_n$ up to $\Phi \approx 40°$. The deviation from this ratio takes place in these ionospheric regions where at least at one end of the field line, passing over the equator in the examined altitudinal interval, there occurs sunrise.

References

1. Appleton, E. V. Nature, 157, 1946, 691.
2. Burcard, O. 1950 Proceed. Mixed Commission on Ionosphere, 1951, 145.
3. Maeda, H. Rep. Ionsph. Res., Japan, 9, 1955, 59.
4. Керблай, Т. С. Исследования ионосферы, М., 1960, 5, 74.
5. Rao, B. C. N. J. Geophys. Res., 68, 1963, 2541.
6. Eccels, D., J. W. King. PIEEE, 57, 1969, 1012.
7. Goldberg, R. A. PIEEE, 57, 1969, 1119.
8. Гдалевич, Г. Л., Б. Н. Горожанкин, Й. С. Кутиев, Д. Т. Самарджиев, К. Б. Серафимов. Космические исследования, 11, 1973, 2, 245.
9. Serafimov, K. B., J. S. Kutiev, S. K. Chapkunov, Ts. P. Dachev, K. J. Gringauz, G. L. Gdalevich, B. N. Gorojankin. Rep., Days of Bulgarian Sci. and Techn., India, 1973.
10. Anderson, D. W. Planet Space Sci., 21, 1973, 421.
11. Dyson, P. L., J. Geophys. Res., 74, 1969, 6291.
12. McClure, J. P., W. B. Manson. J. Geophys. Res., 78, 1973, 7431.
13. Sagalin, R. G., M. Smiddy, M. Aboned. J. Geophys. Res., 79, 1974, 4255.
14. Гершман, Б. Н. Динамика ионосферной плазмы. М., Наука, 1974.
15. Гринтауз, К. Й., К. Б. Серафимов, К. Г. Шмеловски, Я. Шмилауер. Космические исследования, 11, 1973, 1, 95.
16. Бишов, К., Г. Л. Гдалевич, В. С. Губски, Я. Д. Дмитриева, Г. З. Циммерман. Космические исследования, 11, 1973, 2, 267.
17. Афонин, В. В., Г. Л. Гдалевич, К. Й. Гринтауз, Я. Кайнарова, Я. Шмилауер. Космические исследования, 11, 1973, 2, 254.
18. Серафимов, К. Б., С. К. Чапкънов. Военна техника, 7, 1973, 4, 1618.
19. Hanson, W. B., A. S. Nagy, R. T. Moffet. J. Geophys. Res., 78, 1973, 751.
20. Шмилауер, Я., К. Й. Гринтауз, В. В. Афонин. Геомагнетизм и аэрономия, 15, 1975, 4 (в печати).
21. McClure, J. P. J. Geophys. Res., 74, 1969, 289.
22. McClure, J. P. J. Geophys. Res., 76, 1971, 3106.
23. McClure, J. P., B. E. Troy. J. Geophys. Res., 76, 1971, 4534.
24. Brace, L. H., B. M. Reddy. J. Geophys. Res., 70, 1965, 5783.
25. Bauer, L. P. Planet. Space Sci., 18, 1970, 1447.
26. Clark, D. H., W. J. Raitt, A. P. Willmore. J. Atmos. Terr. Phys., 35, 1973, 63.
27. Hopkins, H. D. Planet. Space Sci., 20, 1972, 2093.
28. Пономарев, В. Н. Космические исследования, 9, 1971, 6, 878.
29. Rao, B. C. N. Scientific Report No 30, NPL, 1966.
30. Knudsen, W. C. J. Geophys. Res., 73, 1968, 841.

Измерение ионной концентрации в экваториальном районе

К. Б. Серафимов, И. С. Кутиев, Й. Ф. Арсов, Ц. П. Дачев, Г. А. Станев, Г. Л. Гдалевич, В. В. Афонин, В. Губский, В. Озеров, Я. Шмилауер

(Резюме)

По полученным данным от сферичных ионных ловушек и от радиочастотного электронного зонда, которые были монтированы на спутнике „Интеркосмос-8", в работе исследуется поведение экваториальной аномалии в послеполуденные и вечерние часы, на высотах 300—500 km. Результаты, полученные в долготном интервале 150°—0°, показывают аномальное распределение ионной концентрации, что тесно связано с реальным геомагнитным полем. В послеполуденные часы наблюдается ясно выраженное двухмаксимумное распределение. В районе Бразильской магнитной аномалии северный максимум выражен сильнее и смещается к магнитному экватору. В вечерние часы (от 18^h30^m до 21^h08^m местного времени) наблюдается исчезновение двухмаксимумного распределения для того же долготного интервала. В районе Бразильской магнитной аномалии наблюдаются крупномасштабные ионосферные неоднородности. Электронная температура, измеренная при вышеуказанных условиях, не различается сильно от температуры нейтральной атмосферы в широтном районе $\pm 40°$.

BULGARIAN ACADEMY OF SCIENCES

SPACE RESEARCH IN BULGARIA, 1

Sofia · 1978

Preliminary Results of Ion Density Measurements Obtained by Intercosmos-12 Satellites

I. S. Kutiev, Ts. P. Dachev, G. A. Stanev, K. B. Serafimov

The Intercosmos-12 satellite was launched on October 31, 1974, with apogee 718 km, perigee 250 km and inclination 74°. The measurements of ion and electron density and of electron temperature are described in [1]. Some measurement results of ion density at the satellite pass through the north and south polar regions are shown in this paper.

The orbital conditions are such that the satellite crosses the north polar region from its day towards its night side at 250-430 km altitude and attains invariant latitude of $\Lambda = 73°$. The south polar region from its day is crossed by the satellite during the night from midnight towards downside close to its apogee about 718 km, and attains invariant latitude of $\Lambda = 73°$.

The ion concentrations are obtained from the records of the volt-ampere curves of the two spherical ion traps situated symmetrically with respect to the satellite axis. In the orbital parts around the apogee two slopes are recorded in the volt-ampere curves, which, according to the results of our previous studies [2, 3], are interpreted as O^+ and H^+ ions. In view of the fact that mass separation is somewhat approximate, He^+ and N^+ ions are not taken into consideration.

The results obtained from the first Intercosmos-12 orbits show one and the same behaviour of the satellite orbits. Therefore, we present here one typical distribution obtained from the 34th orbit on November 1, 1974, from 12^h02^m UT — a magnetically quiet day with $K_p = 1$. The ion density measured is shown on Fig. 1, when the satellite passed through the north (to the right) and through the south (to the left) polar regions.

At the north passage (Fig. 1a) the quick reduction of the O^+ density is due mainly to altitudinal change; from 257 km to about 320 km the satellite comes over F_{max}.

Thereafter, a sharp decrease of the O density almost of an order of magnitude has been observed, and the minimum is at $\Lambda = 67°$. On the top of the diagram are plotted the satellite transits through the north and, respectively, through the south polar region. The hatched area represents the

soft electron precipitation zone taken from [4]. The average situation of the midlatitudinal trough shown with a dotted line is taken from [5]. The stagnation point from 4 is marked with open circle. The minimum in O^+ density appears when the stagnation point is reached. Thereafter the O^+ den-

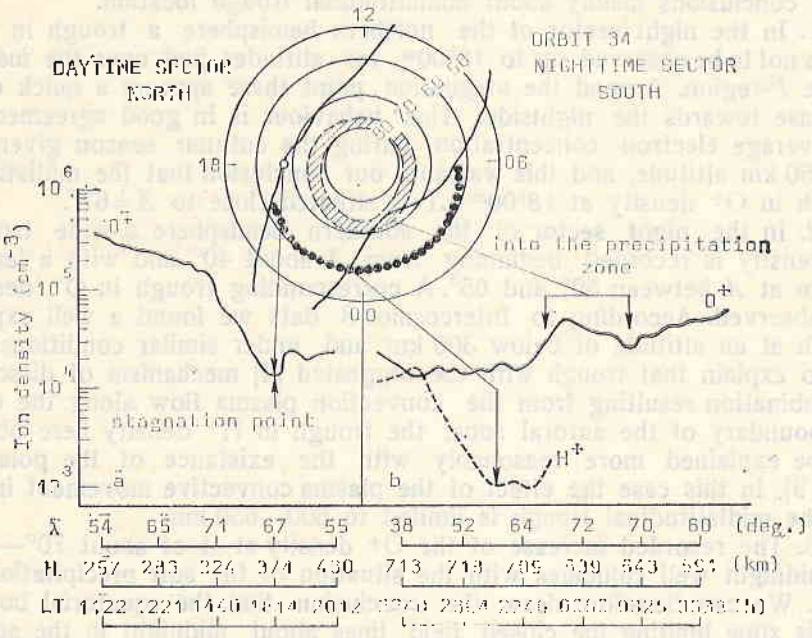

Fig. 1

sity remains low and this probably depends not so much on the satellite introduction in the night ionosphere but on the fact that the satellite is moving along the trough.

Fig. 1b shows the ion concentration distribution along the satellite orbit in the nightside of south polar region. Close to the apogee H has a deep minimum between 60° and 67° just on the spot where the midlatitudinal trough is demonstrated. Here the O^+ density has the lowest value of about 1×10^4 cm^{-3} and forms a broad minimum from $\Lambda=40°$ to $\Lambda=64°$. Here the trough at O^+ density is not to be observed. The O^+ maximum separated by arrows is recorded just at the moment when the satellite passes through the soft electron precipitation zone, as shown on the diagram. It this maximum is indeed due to increased ionization caused by soft energetic electrons, then the equatorial boundary of this zone in the southern hemisphere should be about $\Lambda=55°$ during midnight. However, the O^+ density increase in this region does enable us to follow the H^+ behaviour. In view of the method used, H^+ ions with density lower than one-tenth of the O^+ density cannot be determined. In any case, however, the H^+ density in this zone does not exceed 5×10^3 cm^{-3}. During morning hours in the sunlit ionosphere no trough in O^+ density at about 600 km altitude is to be observed.

This paper is a continuation of the polar ionosphere studies performed by the Intercosmos-12 satellite shown in [6]. Thanks to the other conditions along the Intercosmos-12 orbits, it became possible to draw certain additional conclusions mainly about midlatitudinal trough location.

1. In the night sector of the northern hemisphere a trough in ionization is not to be observed up to 18^h00^m for altitudes just over the maximum of the *F*-region. Around the stagnation point there appears a quick density decrease towards the nightside. This behaviour is in good agreement with the average electron concentration during the autumn season given in [7] for 350 km altitude, and this warrants our conclusion that the midlatitudinal trough in O^+ density at 18^h00^m LT is situated close to $\Lambda = 67°$.

2. In the night sector of the southern hemisphere a wide trough in H^+ density is recorded beginning from Λ about 40° and with a large minimum at Λ between 59° and 65°. A corresponding trough in O^+ density is not observed. According to Intercosmos-8 data we found a well expressed trough at an altitude of below 300 km and under similar conditions. If we are to explain that trough with the suggested [4] mechanism of dissociative recombination resulting from the convection plasma flow along the equatorial boundary of the auroral zone, the trough in H^+ density here observed can be explained more reasonably with the existance of the polar wind [7, 8, 9]. In this case the effect of the plasma convective movement in creating the midlatitudinal trough is limited to 600—650 km.

3. The recorded increase of the O^+ density at Λ of about 70°—72° after midnight well coincides with the situation of the soft precipitation zone in [4]. We can therefore draw the conclusion that the equatorial boundary of this zone limiting the closed field lines about midnight in the southern hemisphere is at about 65°, where a sharp increase of O^+ density is to be established (Fig. 1b).

4. In the morning sector of the southern hemisphere and at altitudes of about 560-600 km, no trough was to be observed in the O^+ density.

References

1. Chapkunov, S. K., T. N. Ivanova, M. Ch. Petrunova, K. B. Serafimov. Preprint B. 3. 10, XVIII Plenary Mtg. of COSPAR, Varna, 1975
2. Gdalevich, G. L., B. N. Gorozhankin, S. P. Dachev, I. S. Kutiev, K. B. Serafimov. Compt. rend. Acad. Bulg. Sci., 26, 1973, 6, 755.
3. Гдалевич, Г. Л., Б. Н. Горожанкин, И. С. Кутиев, Д. Т. Самарджиев, К. Б. Серафимов. Космические исследования, 11, 1973, 2, 245.
4. Knudsen, W. C. J. Geophys. Res., 79, 7, 1974, 1046.
5. Jelly, D. H., L. E. Petrie. PIEEE, 57, 1969, 1005-1012.
6. Serafimov, K. B., A. Z. Bochev, T. P. Dachev, I. S. Kutiev, J Schmilauer, K. I. Gringaus, V. V. Afonin, G. L. Gdalevich, V. F. Gubskiy, V. D. Ozerov. Preprint IV. C. 7, XVIII Plenary Mtg. of COSPAR, Varna, 1975.
7. Nishada, A. J. Geophys. Res., 72, 1967, 6051.
8. Banks, P. M., T. E. Holzer. J. Geophys. Res., 74, 1969, 26, 6317.
9. Taylor, H. A. Planet. Space Sci., 20, 1972, 1593.

Предварительные результаты о ионной концентрации, полученные от спутника „Интеркосмос-12“

И. С. Кутиев, Цв. Г. Дачев, Г. А. Станев, К. Б. Серафимов

(Резюме)

Описано поведение ионных концентраций, измеренных в полярном районе вдоль орбиты спутника „Интеркосмос-12“. В северном полушарии, на высотах F слоя, наблюдается резкий минимум в концентрации, который соответствует точке стегнации магнитосферного плазменного потока. В южном полушарии, на высотах около 700 km, имеется глубокий провал в концентрации водородных ионов. Аналогичный провал (для инвариантных широт 59—65°) не наблюдается в концентрации кислородных ионов. Объяснение этого явления связано с полярным ветром, который на высотах около 700 m является важнейшим фактором в формировании провала, в то время как в F слое его влияние пренебрежимо. В утреннем секторе южного полушария провал в концентрации кислородных ионов не наблюдается.

BULGARIAN ACADEMY OF SCIENCES

SPACE RESEARCH IN BULGARIA, 1

Sofia · 1978

An Exact Method for Determination of the 6300 Å Oxygen Line Intensity by the Use of $N(h)$ Ionospheric Profiles

K. B. Serafimov, M. M. Gogoshev

1. Introduction

It has been established that, at undisturbed geomagnetic conditions during the night, the general mechanism leading to the red oxygen line emission is the dissociative recombination of O_2^+ ions and, to a significantly lower degree, that of NO^+ ions [1-4]. In 1959 a semi-empirical formula had been deduced [5], relating the 6300 Å intensity to some measured ionospheric parameters — f_0F, $h'F$. This formula reflects in general the behaviour of the intensity of the red emission during the night, but we do not have sufficient coincidence between the values observed and those theoretically calculated. A theoretically established relation on the basis of a new theory of F-region was given in 1972 [6], which reflects far better the relationship between the red emission and the radio-measured parameters of the F-region. In addition to the parameters used by Barbier, we include the thickness of the layer Z, the density scale H and the parameter of the exponent p, at an exponential decrease of the electron density in the overmaximal part of the F-region. An attempt at simultaneous measurement of the 6300 Å emission and of the parameters of the F-region was made [7], in which we obtained very good agreement between the theoretical and experimental data.

The following formula has been used for the theoretical calculation of the intensity of the 6300 Å emission by dissociative recombination:

$$I_{6300} = 0.076 \int_{150}^{500} \frac{\varepsilon . K_1[O_2] . R . N_e . dh}{1 + \frac{K_2[N_2]}{A}} \tag{1}$$

where ε is the effective number of the atoms $O(^1D)$ produced at each action of recombination. If we take into account the cascade transition $^1S - ^1D$, we could assume that $\varepsilon \approx 1$. K_1 is the rate constant of the exchange reaction:

(2) $$O^+ + O_2 \rightarrow O_2^+ + O \quad K_1$$

A is Einstein's coefficient; $A = 0.0091\ s^{-1}$, K_2 is the quenching rate constant of the de-excitative reaction:

(3) $$O(^1D) + N_2 \rightarrow N_2 + O(^3P) \quad K_2$$

R is the ratio O^+/N_e, which changes with the height.

The concentrations of O_2 and N_2 are taken from a model, and $N_e(h)$ is measured directly by ionograms or by rocket measurements.

This formula has, however, an essential defect; it requires the knowledge of the ratio R at every height and this can be obtained by rocket experiments only. Consequently, it can hardly be used for practical calculations.

In the present paper a new method of calculating I_{6300} is given, in which only data from ionosonds and atmospheric models are used.

2. Method

Let us present formula (1) in the following form:

(4) $$I_{6300} = 0.076 \int_{150}^{500} \frac{\varepsilon \cdot K_1[O^+] \cdot [O_2] \cdot dh}{1 + \frac{K_2[N_2]}{A}}.$$

In the above formula the concentration of $O^+(h)$ can be obtained in the following way:

For the range of 150—500 km, in which the red line is emitted, we can write the following equation:

(5) $$[O^+] + [NO^+] + [O_2^+] = N_e,$$

expressing the quasi-neutrality of the plasma in this region.

At these night conditions the equilibrium concentration of O_2^+ is given by:

(6) $$[O_2^+] \approx \frac{K_1[O^+][O_2] + K_6[N_2^+][O_2]}{\alpha_D(O_2^+) \cdot N_e}$$

where $\alpha_D(O_2^+)$ is the rate constant of the dissociative recombination for O_2^+ ions, and K_6 is the rate constant of the exchange reaction between N_2^+ and O_2. It was shown [8] that $K_1 \approx 4 \times 10^{-11}\ cm^3\ s^{-1}$ and $K_6 \approx 2 \times 10^{-18}\ cm^3 s^{-1}$. Taking also into account that $[O^+] \gg [N_2^+]$, we could neglect the second term in the numerator of (6), and therefore equation (6) takes the form:

(7) $$[O_2^+] \approx \frac{K_1 \cdot [O^+] \cdot [O_2]}{\alpha_D(O_2^+) N_e}.$$

The equilibrium concentration of NO^+ is

(8) $$[NO^+] \approx \frac{K_3[O^+][N_2] + K_4[N_2^+][O] + K_5[N^+][O_2]}{\alpha_D(NO^+) N_e}$$

where K_3, K_4 and K_5 are the rate constants of the corresponding exchange reactions, and $\alpha_D(NO^+)$ is the velocity of the dissociative recombination of NO^+ ions.

In the range of 180—300 km, where about 90 per cent of the integral value of 6300 Å line is emitted [9], we have:

$$[N_2] > [O_2] \approx [O], \tag{9}$$

$$[O^+] \gg [N_2^+] > [N^+]. \tag{10}$$

We assume that $K_3 \approx 10^{-10} \div 10^{-12}$ cm^3 s^{-1}; K_4 2.5×10^{-10} cm^{3}s^{-1} and $K_5 \approx 2\ 2 \times 10^{-10}$ cm^{3}s^{-1} [10]. At these values of the rate constants and according to (9) and (10) we make the following evaluations:

$$K_4[O][N_2^+] \quad K_5[N^+][O_2] \ll K_3[N_2][O^+] \tag{11}$$

and the expression (8) is reduced to

$$[NO^+] \approx \frac{K_3[N_2][O^+]}{\alpha_D(NO^+) \cdot N_e}. \tag{12}$$

The substitution of (7) and (12) in (5) leads to

$$[O^+] = \frac{\alpha_D(NO^+) \cdot \alpha_D(O_2^+) \cdot N_e^2}{\alpha_D(NO^+) \cdot \alpha_D(O_2^+) \cdot N_e + \alpha_D(O_2^+) K_3[N_2] + \alpha_D(NO^+) K_1[O_2]}. \tag{13}$$

In this manner formula (13) expresses the behaviour of $[O^+]$ by the behaviour of the concentration of the most frequently and most easily measured ionospheric parameter — the electron density N_e. We know that the variations in the concentration of the neutral compounds and the rate constants depend mainly on the temperature and consequently, under undisturbed geomagnetic and solar conditions, they can be determined from the known models.

The substitution of the expression (13) in (4) leads to the following formula for λ 6300 Å intensity:

$$I_{6300} = 0{,}076 \cdot A \cdot \varepsilon \int_{150}^{500} \frac{K_1 \alpha_D(NO^+) \cdot \alpha_D(O_2^+)[O_2] N_e^2 \cdot dh}{(\alpha_D(NO^+) \cdot \alpha_D(O_2^+) N_e + \alpha_D(O_2^+) \cdot K_3[N_2] + \alpha_D(NO^+) K_1[O_2])(A + K_2[N_2])} \tag{14}$$

The expression (14) reflects the behaviour of the λ 6300 Å line intensity as a function only of the electron density at a given atmospheric model. This formula can easily be reduced to a convenient form for numerical integration.

3. Experimental Verification of the Method

As an example of the application of the method to the experimental observations, the initial data are shown in Fig. 1. The intensity of the line 6300 Å is determined in the Observatory at Stara Zagora, Bulgaria ($\varphi = 42°27$ N, $\Lambda = 23°41$ E), by a zenith tilting-filter photometer. The accuracy of the registration of λ 6300 is about 5 per cent. Two moments were selected on October 29, 1973, at 21^h00^m and 22^h00^m LT. The observations of the ionosphere were performed at the ionospheric station near Sofia

($\varphi = 42°41$ N, $\Lambda - 23°21$ E). The distance between the two points of observation is about 200 km. The calculation of the $N_e(h)$ profiles is done by a laminar method [11]. Fig. 1 shows also the three atmospheric models used at exospheric temperatures of 500°K, 800°K and 1000°K, according to Jacchia's revised model [12].

Since from the $N_e(h)$ profiles the distribution of electron density is obtained up to the maximum of the F-layer, in the over-maximal part of the same layer the parabolic distribution to Z_m-level is used, the exponential distribution being used above it. Here Z_m is the semi-thickness of the F-layer.

The following rate constants were used for the calculations:

$\alpha_D(O_2^+) = 2.2\times10^{-7}$ cm^3 s^{-1}, $\alpha_D(NO^+) = 4.5\times10^{-7}$ cm^3 s^{-1}, $A = 0.0091$ s^{-1}, $K_3 = 21\times0^{-12}$ cm^3 s^{-1} and two different values for K_1:

$$K_1' = 4\times10^{-11}\ \text{cm}^3\ \text{s}^{-1}\ [13] \text{ and}$$

$$K_1'' = 2\times10^{-1}\ \text{cm}^3\ \text{s}^{-1}\ [14].$$

With these constants and according to the data from Fig. 1, the following results were obtained, as presented in Table 1 and in Fig. 1:

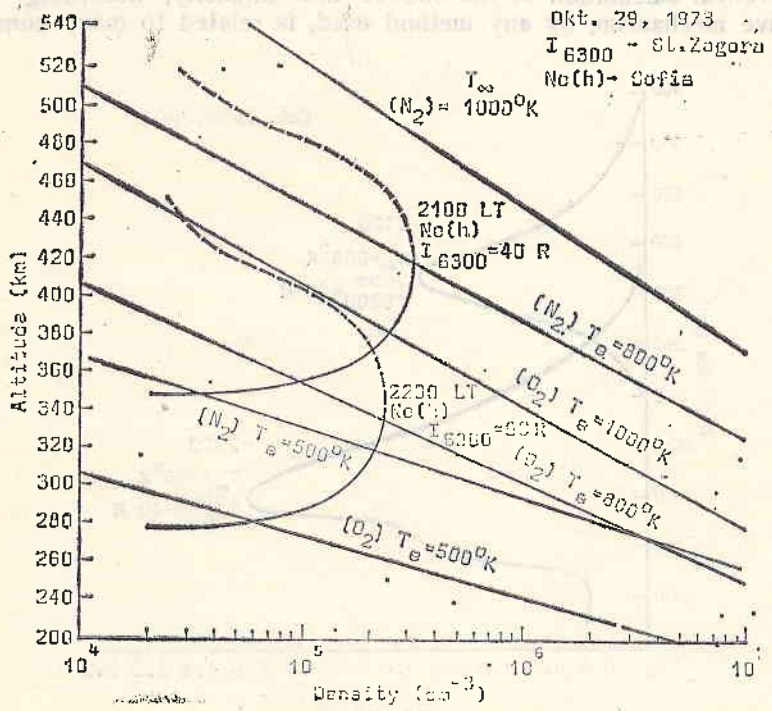

Fig. 1

It is obvious from the Table that at $T_\infty = 500$°K the model gives extremely low values and is, in general, unfit in this case for the very low values of the atmospheric density. In the two other cases, however, the coincidence is very good. One of them is at T_∞ 800° K and $K_1 = 4\times10^{-11}$ cm^{3}s^{-1},

Table 1

T	21^h00^m LT 6300=40 R		22^h00^m LT 6300=90 R	
°K	$K_1'=4\times10^{-11}$	$K_1''=2\times10^{-11}$	$K_1'=4\times10^{-11}$	$K_1''=2\times10^{-11}$
500°K	0.5 R	0.2 R	1.1 R	0.6 R
800°K	[38 R]	21 R	[89 R]	44 R
1000°K	79 R	[43 R]	181 R	[96 R]

and the other one at $T_\infty = 1000$°K and $K_1 = 2\times10^{-11}$cm^{3}s^{-1}. Besides, it has been found that the most essential contribution in the intensity of the 6300 Å emission is that of the terms $\alpha_D(NO^+).\alpha_D(O_2^+)N_e$ and, at lower heights, the term $(A+K_1N_2)$.

4. Estimation of the Precision of the Method

The theoretical calculation of the 6300 Å line intensity, according to the dissociative mechanism, by any method used, is related to many conditions.

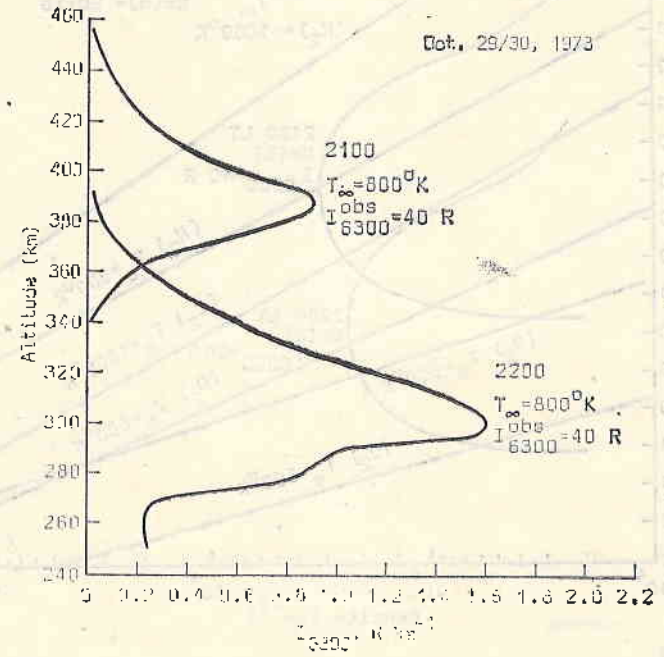

Fig. 2

In the first place this refers to the choice of the rate constants of the reactions. It follows from the calculations in the example given above that a change by a factor of 2 only in the value of the very important constant K_1 of reaction (2) leads to an equal change in the red line intensity. The

analysis of formula (14) and the example given in Fig. 1, Table 1 and Fig. 2 show that the choice of this constant is of essential importance. Besides that it is accepted that the values of $\alpha_D(O_2^+)$ and $\alpha_D(NO^+)$ are known with greater confidence, while on the other hand the inaccuracy in their measurement plays a small part in the calculation of the 6300 Å line intensity.

Another source of errors is the unknown exact temperature dependences of the rate constants of the dissociative and exchange reactions which, in combination with the lack of sufficient knowledge on the temperature distribution at the given moment, could also lead to uncertain results.

Notice should also be taken of the fact that the problem of exact calculation of the products from the dissociative recombination is reduced to the choice of the most reliable atmospheric model at a given case. On the other hand, as in the case of rate constants of the temperature dependence reactions, this is connected with the knowledge of the value T_∞.

In the case presented in Fig. 1, Table 1 and Fig. 2, the calculations are in best agreement with the experimental data at $T_\infty = 800°K$ and $K_1 = 4 \times 10^{-11}$ cm^{3}s^{-1}, and also at $T_\infty = 1000°K$ and $K_1 = 2 \times 10^{-11}$ cm^{3}s^{-1}. Of course, it is hardly possible to overcome this difficulty only by the use of photometric and ground-based ionospheric data.

It may be recommended that the choice of the atmospheric model for the calculation of the 6300 Å line intensity, at a given night, be done according to some of the lowest values of the red oxygen line, for which we must be sure that there exist no other generative mechanisms besides the dissociative recombination. By the model thus chosen, in which we have the best coincidence, we make the calculations for all other points during the night.

References

1. Chamberlan, J. W. Physics of .the Aurora and Airglow. New York-London, 1961.
2. Серафимов, К. Б., М. М. Гогошев. В: Доклади на Юбилейната научна сесия. Стара Загора, 1971, 75.
3. Гогошев, М. М. Кандидатска дисертация. С., БАН, 1973.
4. Гогошев, М. М., К. Б. Серафимов. Геомагнетизм и аэрономия, 13, 1973, 95.
5. Barbier, D. Géophysique extérieure. New York-London, 1963.
6. Serafimov, K. B., M. M. Gogoshev. Compt. rend. Acad. Bulg. Sci., 25, 1972, 2.
7. Gogoshev, M. M., K. B. Serafimov. Compt. rend. Acad. Bulg. Sci., 25, 1972, 609.
8. Серафимов, К. Б. Физика средней ионосферы. С., БАН. 1970.
9. Gogoshev, M. M. Compt. rend. Acad. Bulg. Sci., 25, 1972, 487.
10. Swartz, W. E. Ionospher. Res. Scien. Rep. 381, PenSt. Univ., 1972.
11. Кутиев, И. Кандидатска дисертация. С., БАН, 1973.
12. Jacchia, L. G. Revised static models of thermosphere and exosphere with empirical temperature profiles. Smithson. Sp. Rep., 332, 1972.
13. Fehsenfeld, F. C., P. D. Goldan, A. L. Schmeltekopf, E. E. Ferguson. Plan. Sp. Sci., 13, 1965, 579.
14. Copsey, M. J., D. Smith, J. Sayers. Plan. Sp. Sci., 14, 1966, 1047.

Точный метод определения интенсивности красной кислородной линии 6300 Å посредством использования ионосферных профилей

К. Б. Серафимов, М. М. Гогошев

(Резюме)

Описан точный метод определения интенсивности красной кислородной линии 6300 Å. Этот метод позволяет определить λ_{6300} как функцию только электронной концентрации, которая легко получается по данным ионосферной станции. Полученные теоретические результаты с достаточной точностью совпадают с экспериментальными данными, полученными в Обсерватории по изучению свечения ночного неба в г. Стара-Загора. Рассмотрены возможные источники ошибок и сделаны предложения для будущих измерений.

BULGARIAN ACADEMY OF SCIENCES

SPACE RESEARCH IN BULGARIA, 1

Sofia · 1978

Informational Characteristics of Some Natural Formations

D. N. Mishev, V. S. Djepa, T. K. Yanev

The spectrum of the electromagnetic radiation reflected by the natural formations is continuous. In practice, however, a finite number of wavelengths, mainly in the visible range, are chosen for investigation purposes. The set of the reflexion index values for these wavelengths forms a sampled reflective characteristic. Even thus sampled the reflective characteristic contains considerable information which allows the natural formations to be divided in classes of objects with similar reflective characteristics. The degree of the similarity in a given class is conditioned by the extent of the confidence limits of the reflective characteristic. For some wavelengths, however, it is possible to obtain non-empty cross-sections between the confidence intervals of the different classes of objects. In such cases the methods of the pattern recognition theory are applied for the identification of the different classes of objects. It would be of importance to solve the following problem: for which wavelengths the uncertainty obtained from the distribution cross-sections is the greatest and by which classes it is mainly determined. If the answer to these questions is available, more experimental efforts could be concentrated on the respective wavelengths and classes of objects. The solution of these problems will therefore be in the focus of our attention.

1. The Formulation of the Problem

Each natural formation is described by a sampled reflective characteristic $r(\lambda_i)$, r_i — reflection index, λ_i — wavelength, $i=1,\ldots,m$. Formations with similar reflective characteristics $r(\lambda_i)$ form a class of objects. This similarity is expressed by the statistical proximity of $r(\lambda_i)$, i. e. in the presence of $r(\lambda_i)$ distribution around an average reflective characteristic $\bar{r}(\lambda_i)$ (we shall henceforth designate this characteristic by $r(\lambda_i)$ alone). The experience obtained

so far furnishes grounds for such an assumption, and even the existence of a normal distribution [1] can be assumed.

Let the set $M \equiv \{r_j(\lambda_i)\}$ from $j=1,\ldots,N$ classes of objects be given. The appearance of an object within the limits of the class $r_j(\lambda_i)$ with a fixed wavelength λ_i will be considered verified if the reflective characteristic obtained is within the confidence limits $r_j(\lambda_i) \pm \Delta r_j(\lambda_i)$ of $r_j(\lambda_i)$. But there exists a certain probability that this object should belong to each one of the other $N-1$ classes of M. In this case, these are the conditional probabilities $p_{ijk}(r_{ik}/r_{ij})$ that at a fixed λ_i and in the presence of indications for r in the confidence interval of the j class, in reality there is an object from the k class. It is obvious that the presence of probabilities $p_{ijk} \neq 0$ for $j \neq k$ leads to uncertainty at the data processing, the total uncertainty of the set being characterized by the matrices $A_i = \| p_{ijk} \|$ of the conditional probabilities p_{ijk}. But the matrices A_i can have different dimensions and, accordingly, a different number of probabilities p_{ijk}. For the purposes of comparative analysis it is necessary to normalize p_{ijk} in such a way that the normalized values should satisfy the condition $\sum_{(k)} p_{ijk}^{(n)} = 1$. The substitution

$$p_{ijk}^{(n)} = \frac{p_{ijk}}{\sum_{(k)} p_{ijk}}, \tag{1}$$

is suitable for the purpose.

The events of "appearance of a jth class object in the ith wavelength" form a full event system, i. e.

$$\sum_{(j)} p_{ij}^{(n)} = 1 \tag{2}$$

if we assume that the set M exhausts all probable classes of objects (or at least those of them which are of interest to the analysis). Further on we shall consider this assumption realized. The problem solved in the course of the work done is the following: an indication for r in the confidential limits of a given class has been obtained. It is necessary at a fixed wavelength to evaluate the average uncertainty which has been introduced by the distributions of the other classes from the set under consideration, if the evidence is accepted as belonging to the class in which it has been obtained. For such an evaluation the quantity of "information" is suitable.

2. Method

The uncertainty contained in matrix A_i when (1) and (2) are fulfilled is evaluated by:

$$I_i = H_i(p_j) - \tilde{H}_{ij}(r_{ik}/r_{ij}), \tag{3}$$

where $H_i(p_j) = -\sum_{(j)} p_{ij} \log p_{ij}$ is the unconditional entropy of the p_{ij} probabilities for the appearance of the j object in the wavelength,

$\tilde{H}_i = -\sum_{(j)} p_{ij} \sum_{(k)} p^{(n)}_{ijk} \log p^{(n)}_{ijk}$ is the conditional entropy of the probabilities $p^{(n)}_{ijk} = p(r_{ik}/r_{ij})$.

The coefficient

$$\delta_i = \frac{I_i}{H_i} = 1 - \frac{\tilde{H}_i}{H_i} \tag{3a}$$

can be used for the comparative analysis as being more convènient.

The magnitude δ_i is suitable because it varies in the interval $0 \leq \delta_i \leq 1$. Equations (3) and (3a) provide a solution to the problem of the uncertainty of evaluation at the identification of the objects from M. An answer to the question what is the contribution of the separate classes from M to the total uncertainty, can be obtained when applying (3) and (3a) for different additional subsets M_l, obtained from M by excluding subsets M_l, $l = 1, \ldots, L$.

3. Conclusions

These two problems: $H_i^{(M)}$ and $\delta_i^{(M)}$ determination for $r_j(\lambda_i) \in M$ and, respectively, $H_i^{(M_l)}$ and $\delta_i^{(M_l)}$ for $r_j(\lambda_i) \in M_l$ can be extended by the introduction of various confidential intervals $\pm \Delta r_j(\lambda_i)$ corresponding to the various distribution dispersions of the objects from M. With a given confidence coefficient of the confidence intervals, the quantity I of information, the part δ it represents from the maximum information $I_{max} = H_i$ and the subset M_l with the greatest contribution to the reduction of I, or δ_i respectively, can thus be determined.

Table 1

No of object	Name of object	Characteristic of the objects at azimuth 225° and canted shooting angle of 45°	
1	birch	young tree	winter species
2	"	"	young leaf
3	"	"	full leaf
4	"	"	late verdure
5	"	old tree	winter species
6	"	"	full leaf
7	"	"	late verdure
8	"	"	fresh bark
9	elm	old tree	young leaf
10	"	"	full leaf
11	oak	young tree	winter species
12	"	old tree	full leaf
13	"	"	during the autumn
14	lime	"	winter species
15	"	"	full leaf
16	"	"	during the autumn
17	aspen	young tree	winter species
18	"	"	young leaf
19	"	"	full leaf
20	"	old tree	young leaf
21	"	"	full leaf
22	"	"	late verdure
23	"	"	during the autumn

Table 2

Spectral Intensity Coefficients of the Natural Formations Examined

λ (nm) \ Class N°	1	2	3	4	5	6	7	8	9	10	11
400	0.058	0.047	0.026	0.059	0.072	0.033	0.084	0.202	0.026	0.033	0.050
410	0.057	0.048	0.027	0.060	0.073	0.034	0.086	0.203	0.027	0.033	0.050
420	0.056	0.049	0.030	0.061	0.074	0.037	0.086	0.204	0.027	0.033	0.050
430	0.054	0.050	0.031	0.062	0.074	0.039	0.091	0.205	0.027	0.035	0.050
440	0.052	0.052	0.034	0.061	0.074	0.044	0.097	0.209	0.030	0.037	0.050
450	0.050	0.056	0 036	0.065	0.073	0.046	0.101	0.210	0.031	0.039	0.050
460	0.049	0.059	0.036	0.073	0.072	0.044	0.109	0.211	0.032	0.040	0.050
470	0.047	0.060	0.037	0.076	0.071	0.042	0.115	0.211	0.034	0.040	0.050
480	0.045	0.060	0.037	0.075	0.070	0.044	0.123	0.212	0.036	0.039	0,050
490	0.045	0.061	0.039	0.087	0.070	0.048	0.131	0.214	0.038	0.037	0.050
500	0.044	0.063	0.040	0.095	0.071	0.045	0.144	0.215	0.043	0.039	0.050
510	0.044	0.071	0.042	0.106	0.073	0.048	0.161	0.215	0.054	0.046	0.051
520	0.044	0.090	0.052	0.120	0.077	0.065	0.185	0.215	0.072	0.058	0.053
530	0.045	0.119	0.070	0.149	0.080	0.087	0.213	0.214	0.092	0.078	0.056
540	0.047	0.138	0.085	0.169	0.082	0.106	0.233	0.213	0.109	0.096	0.059
550	0.050	0.147	0.091	0.176	0.087	0.113	0.245	0.213	0.118	0.108	0.060
560	0.052	0.142	0.088	0.178	0.090	0.110	0.249	0.213	0.117	0.105	0.061
570	0.051	0.130	0 081	0.173	0.091	0.099	0.247	0.216	0.104	0.095	0.063
580	0.050	0.117	0.071	0.168	0.095	0.088	0.241	0.220	0.092	0.084	0.064
590	0 050	0.111	0.071	0.168	0.098	0.090	0.234	0.224	0.083	0.074	0.065
600	0.050	0.103	0.068	0.160	0.100	0.083	0.229	0.231	0.073	0.066	0.066
610	0.049	0.103	0.064	0.152	0.101	0.073	0.224	0.239	0.064	0.058	0.067
620	0.049	0.095	0.060	0.153	0.101	0.068	0.220	0.247	0.060	0.052	0.068
630	0.050	0.092	0.059	0.151	0.102	0.065	0.211	0.254	0.061	0.050	0.067
640	0.051	0.090	0.059	0.143	0.102	0.069	0.205	0.261	0.061	0.050	0.066
650	0.052	0.086	0.059	0.141	0.101	0.070	0.202	0.269	0.060	0.049	0.665

4. Example

The problems formulated above were solved under the following conditions: a set M of deciduous varieties consists of 23 classes of reflective characteristics $r_j(\lambda_i)$, $j=1,\ldots,23$, $i=1,\ldots,26$ (Tables 1,2) of oak, elm, lime, aspen, and birch-trees (Fig. 1). The characteristics are obtained under similar conditions — azimuth 225° and canted shooting angle of 45° [2].

The measurement accuracy of r is 0.01. Experimental data for relation between the confidence intervals $\Delta r_j(\lambda_i)$ and r being unavailable, we took as a first approximation the linear function:

$$\Delta r_{ij} = q r_{ij}, \tag{4}$$

We assumed that the ratio coefficient q varies within the interval $0.01 \div 0.075$ with confidence coefficient $S=0.95$. We selected the following values 0.01, 0.02, 0.04, 0.075 from the interval. The range of q-variations was adopted according to [4].

12	13	14	15	16	17	18	19	20	21	22	23
0.044	0.071	0.068	0.034	0.034	0.056	0.034	0.040	0.041	0.020	0.030	0.047
0.043	0.080	0.066	0.032	0.032	0.057	0.035	0.041	0.040	0.020	0.030	0.046
0.043	0.089	0.062	0.032	0.032	0.059	0.038	0.042	0.041	0.020	0.030	0.048
0.043	0.097	0.060	0.038	0.033	0.061	0.040	0.045	0.042	0.021	0.030	0.049
0.041	0.102	0.064	0.042	0.030	0.062	0.043	0.048	0.043	0.022	0.031	0.050
0.040	0.106	0.066	0.045	0.030	0.063	0.046	0.050	0.043	0.024	0.032	0.051
0.040	0.107	0.064	0.046	0.030	0.065	0.046	0.051	0.042	0.027	0.034	0.054
0.040	0.106	0.063	0.047	0.039	0.068	0.048	0.051	0.041	0.030	0.035	0.061
0.040	0.106	0.066	0.047	0.055	0.070	0.048	0.051	0.042	0.031	0.037	0.068
0.040	0.111	0.070	0.043	0.052	0.071	0.049	0.054	0.047	0.030	0.040	0.074
0,045	0.122	0.072	0.047	0.045	0.072	0.054	0.061	0.052	0.030	0.044	0.081
0.057	0.145	0·074	0.059	0.038	0.074	0.064	0.074	0.063	0.034	0.053	0.091
0.084	0.190	0.077	0.081	0.034	0.076	0.082	0.102	0.080	0.042	0.065	0.112
0.115	0.220	0.078	0.099	0.039	0.079	0.106	0.118	0.107	0.055	0.081	0.142
0.129	0.240	0.080	0.111	0.051	0.081	0.109	0.123	0.117	0.065	0.088	0.161
0.150	0.255	0.081	0.116	0.071	0.082	0.124	0.129	0.125	0.072	0.092	0.177
0.140	0.267	0.081	0.105	0.080	0.084	0.122	0.128	0.128	0.073	0.098	0.188
0.108	0.275	0.082	0.092	0.098	0.085	0.108	0.116	0.125	0.071	0.090	0.200
0.089	0.281	0.082	0.082	0.088	0.087	0.095	0.103	0.117	0.065	0.080	0.210
0.073	0.282	0.084	0.068	0.087	0.089	0.090	0.094	0.104	0.058	0.072	0.220
0.085	0.282	0.086	0.078	0.082	0.090	0.084	0.090	0.095	0.058	0.068	0.220
0.066	0.284	0.087	0.066	0.076	0.090	0.081	0.087	0.087	0.060	0.066	0.214
0.060	0.289	0.088	0.064	0.081	0.090	0.077	0.082	0.080	0.059	0.065	0.208
0.063	0.299	0.089	0.060	0.081	0.090	0.074	0.079	0.071	0.051	0.064	0.199
0.053	0.315	0.089	0.055	0.064	0.091	0.073	0.079	0.060	0.058	0.063	0.191
0.049	0.330	0.089	0.052	0.062	0.091	0.072	0.079	0.055	0.058	0.062	0.186

4.1. Determination of the Sampling Interval

The greatest admissible value of the sampling interval was determined under the following condition: we assume that the reconstruction of the continuous reflective characteristics is performed by Lagrange's polynomial of zero power. The considerations for this assumption are: the $\Delta\lambda$ value by means of which the reflective characteristics have been obtained is at the accuracy limit of the spectrograph we have used, and therefore we do not know anything definite about the r behaviour in the $\Delta\lambda$ interval. That is why we assumed that in this interval $r=\text{const}$ (the zero power of the Lagrange's polynomial). Then, according to [3], the admissible value of $\Delta\lambda$ is equal to

$$\Delta\lambda_{\text{adm}} \leq \varepsilon_0 / M_1 \tag{5}$$

where ε_0 is the admissible error for r and M_1 is the maximal value of $dr/d\lambda$.

We assumed that the measurement accuracy of r limits ε_0, i.e. ε_0 0.01 for the examined set of reflective characteristics M. For M we obtained the value $M_1 = \frac{0.03}{10} \frac{1}{\text{nm}}$.

Then from equation (5) we obtain $\Delta\lambda_{adm} \leq 3.4$ nm < 10 nm.

This result shows that the approximation with a zero polynomial at $\Delta\lambda = 10$ nm is insufficiently precise. Therefore, there are no formal grounds to maintain that the mean information value I between two adjacent values

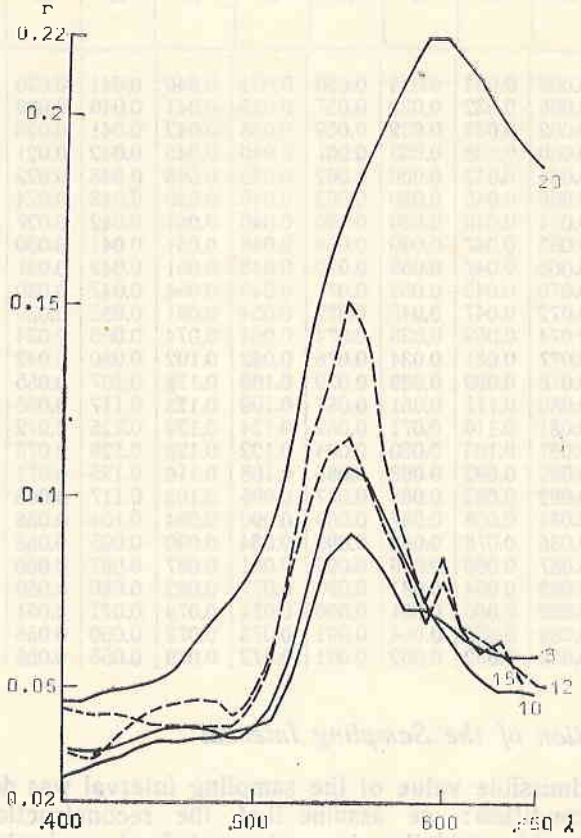

Fig. 1

λ_i and λ_{i+1} would be the arithmetic mean of I_i and I_{i+1}. As the interva $\Delta\lambda = 10$ nm is relatively small, we can assume that there exists a significant correlation in the distributions of r for λ_i and λ_{i+1}. In such a case it is probable that the mean value of I in the interval $\Delta\lambda = \lambda_{i+1} - \lambda_i$ would not differ essentially from $(I_i + I_{i+1})/2$.

4.2. Determination of Information I

The following two problems can be formulated in the study of the structural characteristics of a set of objets.

1. What is the uncertainty in the evaluation of the appurtenance of a single indication (single experiment).

2. What is the uncertainty in the evaluation of the appurtenance of all objects observed (multiple experiment).

In the first problem the appearance of any object from the set is equally probable, inasmuch as we assume that each one of the objects may

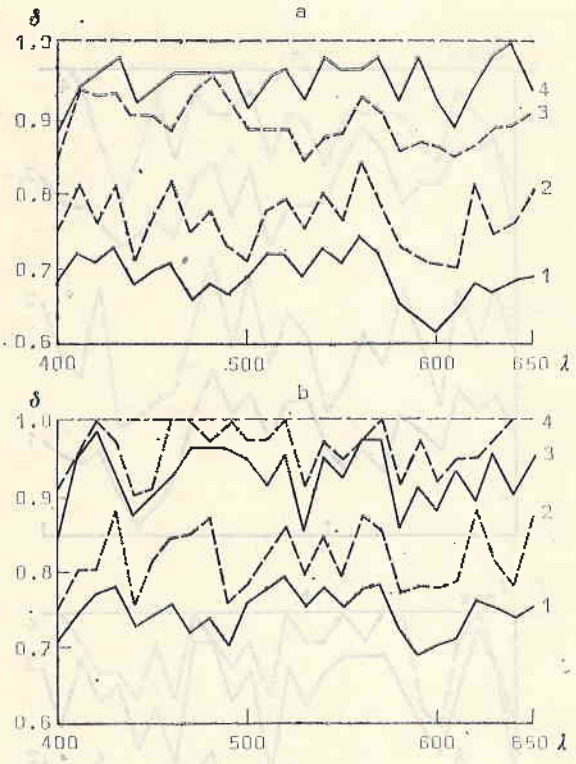

Fig. 2

appear (without being interested in how many times it would appear at a multiple repetition of the experiment), i. e. $p_{ij} = \text{const} = p = 1/N$.

In the second problem it is important that the objects can possess different a priori frequency p_{ij} of appearance under the conditions of the experiment.

In this study our attention was focused on the first problem as it is independent from the determined distribution of the a priori probabilities.

To determine the conditional probabilities $p_{i/k}$ (r_{ik}/r_{ij}) it is assumed, according to [1, 4] that the distribution of r for the different objects is normal.

In such a case the conditional probabilities are obtained according to the formula:

(6) $$p_{ijk}(r_{ik}/r_{ij}) = \Phi(z)\Big|_{z_{1ijk}}^{z_{2ijk}}$$

where

(6a) $$z_{1,2\,ijk} = \frac{\pm \Delta r_{ij} - r_{ij} + r_{ik}}{\sigma_{ij}}$$

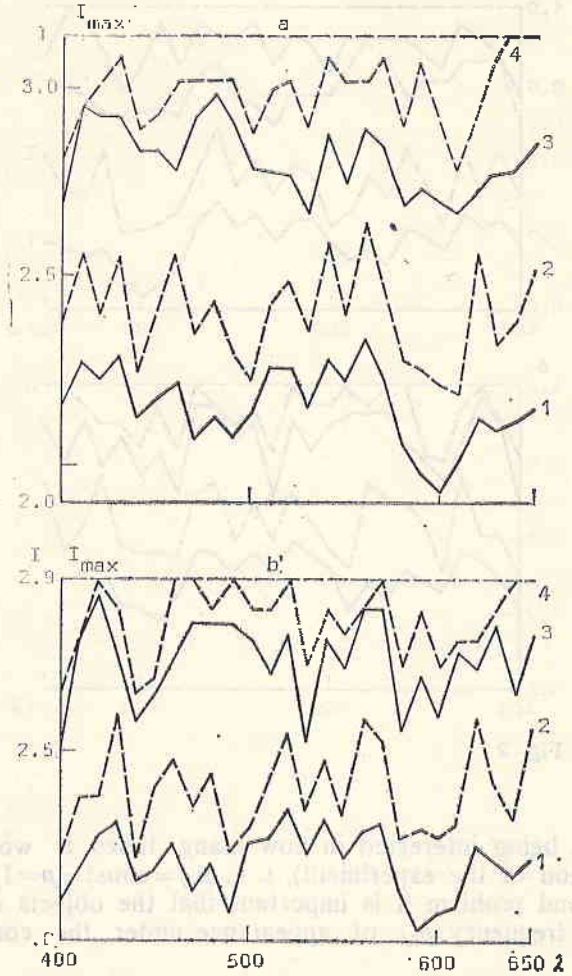

Fig. 3

is the left, the right respectively integration limit of the normalized normal distribution $\Phi(z)$. The confidence intervals Δr_{ij} are determined from equation (4). The standard deviation σ_{ij} is determined from (6a), provided $j=k$. Then $r_{ij}=r_{ik}$ and since $S=0.95$ then $z_{i_j\,1,2}=1.96$. From (4) and (6) follows that

Table 3

Dependence of the Information (I) and δ on the Wavelength (λ_i) and the Coefficient (q)

λ (nm)	q=0.075		q=0.05		q=0.02		q=0.01	
	I	$\delta=\frac{I}{I_{max}}$	I	$\delta=\frac{I}{I_{max}}$	I	$\delta=\frac{I}{I_{max}}$	I	$\delta=\frac{I}{I_{max}}$
400	2.1520	0.6864	2.3163	0.7579	2.6937	0.3591	2.8114	0.8966
410	2.2102	0.7240	2.5691	0.8194	2.9547	0.9423	2.9547	0.9423
420	2.2241	0.7093	2.3955	0.7640	2.9285	0.9340	3.0150	0.9616
430	2.2874	0.7295	2.5441	0.8114	2.9243	0.9327	3.0722	0.9808
440	2.1233	0.6772	2.2409	0.7147	2.8358	0.9044	2.8944	0.9231
450	2.1796	0.6951	2.3911	0.7626	2.8393	0.9055	2.9319	0.9351
460	2.2072	0.7039	2.5518	0.8138	2.7834	0.8877	3.0149	0.9616
470	2.0641	0.6583	2.3468	0.7485	2.9284	0.9340	3.0149	0.9616
480	2.1232	0.6771	2.4321	0.7757	2.9869	0.9526	3.0149	0.9616
490	2.0788	0.6630	2.2909	0.7306	2.9053	0.9266	0.0149	0.9616
500	2.1358	0.6812	2.2230	0.7090	2.7897	0.8897	2.8716	0.9159
510	2.2525	0.7184	2.4279	0.7743	2.7793	0.8864	2.0022	0.9543
520	2.2542	0.7189	2.4861	0.7929	2.7685	0.8829	3.0149	0.9616
530	2.1599	0·6889	2.3528	0.7504	2.6647	0.8498	2.8997	0.9248
540	2.2829	0.7281	2.5092	0.8003	2.8884	0.9212	3.0752	0.9808
550	2.2249	0.7096	2.3936	0.7634	2.7497	0.8770	3.0168	0.9621
560	2.3317	0.7436	2.6340	0.8401	2.8957	0.9235	3.0149	0.9617
570	2.2388	0.7140	2.4680	0.7872	2.8477	0.9082	3.0752	0.9808
580	2.0500	0.6538	2.2795	0.7270	2.6802	0.8548	2.8944	0.9231
590	1.9887	0.6343	2.2537	0.7188	2.7207	0.8677	3.0752	0.9808
600	1.9331	0.6165	2.2076	0.7041	2.6919	0.8585	2.8966	0.9238
610	2.0137	0.6422	2.1948	0.7000	2.6644	0.8497	2.7886	0.8894
620	2.1235	0.6772	2.5637	0.8176	2.7180	0.8668	2.9319	0.9351
630	2.0964	0.9686	2.3288	0.7427	2.7720	0.8841	3.0752	0.9808
640	2.1179	0.6755	2.3822	0.7598	0.7890	0.8895	3.1355	1.0000
650	2.1426	0.6833	2.5170	0.8020	2.8496	0.9088	2.9546	0.9423

(7) $$\sigma_{ij}=\frac{qr_{ij}}{1.96}.$$

As a result of the equation (6a) becomes

(8) $$z_{1,2_{ijk}}=1.96\frac{\pm qr_{ij}-r_{ij}+r_{ik}}{qr_{ij}}.$$

In accordance with equations (3), (3a), (6) and (8) we obtained results for $i=1,\ldots,26$ and $q=0.01$, 0.02, 0.05, 0.075 which are presented in Figs. 2, 3 and Table 3. They show that an increase larger than $q=0.05$ leads to a considerable reduction of the information I, or of δ respectively, and to a resulting increase of the uncertainty of the set identification. This effect is most pronounced at the respective wavelength in the infrared portion.

The elimination of the reflective characteristics Nos. 12, 14, 15, 22 from the M set shows that they contribute considerably to this uncertainty. Figs. 2, 3 and Table 4 show the I- and δ-values obtained after the respective characteristics have been eliminated. These conclusions are valid in ge-

Table 4

Dependence of the Information (I) and the Coefficient $\left(\delta = \frac{I}{I_{max}}\right)$ on the Wavelength (λ_i) and q for $I_{max}=2.9444$

λ (nm)	Upon elimination of the reflective characteristics Nos.=12, 14, 15, 22							
	$q=0.075$		$q=0.05$		$q=0.02$		$q=0.01$	
	I	$\delta=\frac{I}{I_{max}}$	I	$\delta=\frac{I}{I_{max}}$	I	$\delta=\frac{I}{I_{max}}$	I	$\delta=\frac{I}{I_{max}}$
400	2.0906	0.7100	2.2124	0.7514	2.5101	0.8525	2.6526	0.9009
410	2.1845	0.7419	2.3730	0.8059	2.7985	0.9504	2.7985	0.9504
420	2.2752	0.7727	2.3774	0.8074	2.9108	0.9886	2.9444	1.0000
430	2.3037	0.7824	2.6058	0.8850	2.7456	0.9325	2.8715	0.9752
440	2.1562	0.7323	2.2230	0.7550	2.5816	0.8768	2.6526	0.9009
450	2.1873	0.7428	2.4011	0.8155	2.6574	0.9025	2.6980	0.9163
460	2.2549	0.7658	2.4882	0.8450	2.7355	0.9290	2.9444	1.0000
470	2.1324	0.7242	2.3596	0.8014	2.8297	0.9644	2.9444	1.0000
480	2.2033	0.7483	2.4436	0.8299	2.8376	0.9637	2.8715	0.9752
490	2.0798	0.7063	2.2492	0.7639	2.8389	0.9642	2.9444	1.0000
500	2.2653	0.7693	2.3095	0.7844	2.7995	0.9508	2.8715	0.9752
510	2.2788	0.7739	2.4207	0.8221	2.7008	0.9173	2.8715	0.9752
520	2.3501	0.7981	2.5581	0.8688	2.8034	0.9521	2.9444	1.0000
530	2.2349	0.7590	2.3455	0.7966	2.5262	0.8579	2.7319	0.9278
540	2.3213	0.7884	2.4820	0.8430	2.7991	0.9506	2.8715	0.9752
550	2.2275	0.7565	2.3389	0.7944	2.7266	0.9260	2.8008	0.9512
560	2.2981	0.7805	2.5896	0.8795	2.8715	0.9752	2.8715	0.9752
570	2.3101	0.7846	2.5316	0.8598	2.8717	0.9753	2.9444	1.0000
580	2.1331	0.7245	2.2771	0.7734	2.5542	0.8675	2.7255	0.9257
590	2.0383	0.6922	2.2902	0.7778	2.7017	0.9175	2.8715	0.9752
600	2.0710	0.7034	2.2700	0.7709	2.5956	0.8815	2.7282	0.9266
610	2.0955	0.7117	2.3176	0.7871	2.7645	0.9389	2.7985	0.9504
620	2.2553	0.7660	2.5917	0.8802	2.6286	0.8928	2.7985	0.9504
630	2.2116	0.7511	2.4101	0.8185	2.8328	0.9621	2.8715	0.9752
640	2.1787	0.7400	2.3256	0.7898	2.6538	0.9013	2.9444	1.0000
650	2.2243	0.7554	2.5809	0.8765	2.8172	0.9568	2.9444	1.0000

neral for all examined values of q, which shows that at the specification of the real values of q for these objects special attention should be paid to the planning of the experiment.

References

1. Fu, K. S., D. A. Landgrebe, T. L. Phillips. Informational processing of agricultural data obtained through distance measurements. — TIEP, 1968, No. X.
2. Krinov, E. L. The spectral reflective capacity of the natural formations. Moscow, Acad. Sci. USSR, 1947.
3. Temnikov, F. E., V. V. Afonin, V. I. Dmitriev. Theoretical grounds of the informational technics. Moscow, Energy, 1971.
4. Kondratiev, K. Ja., A. A. Grigoriev, O. M. Pokrovskiy. The informational contents of data from space distance indication parameters of environment and natural resources. Leningrad, 1975.

Информационные характеристики природных образований

Д. Н. Мишев, В. С. Джепа, Т. К. Янев

(Резюме)

Рассматривается вопрос о неопределенности при идентификации объектов j-го класса на i-й длине волны ($j=1,\ldots,N$) по отношению к некоторому из остальных $N-1$ классов данного множества объектов $M=\{r_j(\lambda_i)\}$.

Неопределенность рассматриваемого множества выражается матрицей $A=\|p_{ijk}\|$ условных вероятностей p_{ijk}.

BULGARIAN ACADEMY OF SCIENCES
SPACE RESEARCH IN BULGARIA, 1
Sofia · 1978

Discriminant Analysis of Natural Formations Reflective Characteristics by a Minimal Number of Wavelengths

T. K. Yanev, D. N. Mishev

It has been established that the different natural formations reflect the energy of the visible and infrared ranges in different ways. As the range is comparatively broad the spectral reflective characteristics are measured in a considerable number of wavelengths. That makes the measuring process and the subsequent analysis difficult, and the information obtained contains a big amount of redundancy.

The problem to be solved here is the following: what is the minimum number of wavelengths λ_i and exactly in which wavelengths the reflection index must be measured so that the identification of the reflective characteristics $r_j(\lambda_i)$ of a set M, given in advance, from J classes of objects O_j, $j=1, \ldots, J$, can be ensured. We assume that the functions $r_j(\lambda_i)$, $i=1, \ldots, n$ are given with their confidence intervals $\pm \Delta r_j(\lambda_i)$ in the visible range of electromagnetic waves $\Delta\lambda_v=\lambda_n-\lambda_1$. It is assumed that $r_j(\lambda_i)$ are stationary random functions. The problem is solved in two ways: (1) the reflective spectral characteristics are used directly for the purposes of identification; and (2) a transformation of $r_j(\lambda_i)$ is carried out in advance by means of suitable transforming functions, after which the identification of the transformed functions is performed.

1. Identification by Means of $r_j(\lambda_i)$

The dividing surface for the identification of $r_j(\lambda_i)$ is chosen in accordance with the Bayes criterion for a minimum average risk (one-dimensional case):

$$\lambda_0=\frac{w(\lambda_i|a_k)}{w(\lambda_i|a_j)}=\frac{r_{kj}\,p(a_j)}{r_{jk}\,p(a_k)}, \tag{1}$$

where r_{jk} and r_{kj} are weighting coefficients of the j and k classes of objects, $p(a_j)$ and $p(a_k)$ are a priori probabilities of appearance in these classes. In

our case all objects will be considered as equally likely and of equal weight and then $\lambda_0 = 1$, i. e. the dividing surface of the criterion is reduced to the intersection point of the $w(\lambda_i/a_k)$ and $w(\lambda_i/a_j)$ distributions of j and k classes. If this point is out of the confidence limits $+\Delta r_j(\lambda_i)$ and $\pm\Delta r_k(\lambda_i)$ of the classes compared, these classes are identified in the wavelength λ_i. The algorithm is easily realized in the following way:

The matrix A of the relations "the ith and the kth classes are recognizable in the $r_j \pm \Delta r_j$ and $r_k \pm \Delta r_k$ intervals" (these relations are denoted here with 1). The opposite ratios of nonrecognizability (when $r_j \pm \Delta r_j$ and $r_k \pm \Delta r_k$ have a non-empty cross section) are designated by 0. The matrix A is formed for all two-element combinations C_j^2 of the O_j classes and for all wavelengths λ_i.

$A =$

λ_i \ C_J^2	O_{11}	O_{12}	. . .	O_{1n}	O_{21}	. . .	O_{2n}	. . .
λ_1	0	1	. . .	0	0	. . .	0	. . .
. . .	. . .	. . .	. . .	. . .	0	. . .	. . .	. . .
λ_n	1	1	. . .	0	1	. . .	1	. . .

A subset of M is identified in a given combination of wavelengths λ_i, if in each column of A containing the wavelengths there is at least one number 1. In this way the rule for the addition of 0 and 1 is determined: $0+0=0$; $0+1=1+0=1+1=1$. The identification of $r_j(\lambda_i)$ by means of the combination C_n^m of the wavelengths is possible only if all columns of the submatrix formed by C_n^m have a sum equal to 1.

The complete solution of the problem is obtained by studying successively the combinations C_n^m, $m = 1, \ldots, n$ until the first solutions belonging to a given class of wavelength combinations C_n^m are obtained.

2. Identification by Means of Transformation in Advance

The transformation of the original function $r_j(\lambda_i)$ is reasonable if the new function offers better possibilities of identifying $r_j(\lambda_i)$ by means of a smaller number of wavelengths. That is why it is necessary for the transformed function $z = f(r_j)$ to check whether the Bayes criterion shows better results (reducing Type I and Type II errors). For this purpose the law of the distribution of z must be determined:

$$p(z) = p[\Psi(z)] \cdot \Psi'(z), \quad r_j = \Psi(z); \quad \Psi'(z) = \frac{d\Psi}{dz}. \tag{2}$$

After that for the z_j and z_k distributions of the two classes compared the summary error of Type I and Type II is to be found:

$$p = \int_{-\infty}^{z_{cr}} p_k(z)dz + \int_{z_{cr}}^{\infty} p_j(z)dz, \tag{3}$$

where z_{cr} — internal intersection point of $p(z_j)$ and $p(z_k)$.

In general, the integral in (3) is not solvable. When the set is given it can be solved by numerical methods. In order to obtain some analytical results we examined the particular case determined by the following limiting conditions:

I. The distribution $p(r_j)$ is normal;

II. The conditions $\sigma_j \ll \mu_j$ and, in particular, $\sigma_j = q\mu_j$, $q \ll 1$, are satisfied.

III. The functions z are integral transformations which, according to r_j and r_k sampling, are replaced by their sums.

In this study the following transforming functions are examined:

a) Module-structure function:

$$C(\tau) = \int_0^T |f(x) - f(x+\pi)|\, dx \tag{4}$$

used in paper [1]. There it is proved that the function is symmetric with a symmetry axis at $x = \frac{T}{2}$. It is shown also that $C(\tau)$ and $f(x)$ are in a homomorphous relationship, i. e. different functions determined in the following way: $f(x)$, *if* $(jx+C)+D$, $i = \pm 1$, $j = \pm 1$, $C = \text{const.}$, $D = \text{const.}$ may correspond to the same function $C(\tau)$. This homomorphism is not a strong limitation, because in practice it can be easily transformed into an isomorphism by means of control characteristics of the type: $C_{contr}(\tau) = \int_0^{x_{ct}} |f(x) - f(x+\tau)| dx$ and by the $f(x)$ value for $x = x_{ct}$. For the example examined in this work it is not necessary to use such control characteristics.

b) Kolmogorov's structural function:

$$C_K(\tau) = \int_0^T [f(x) - f(x+\tau)]^2 dx; \tag{5}$$

c) Autocorrelation function;

$$K(\tau) = \int_0^T [f(x) - m][f(x+\tau) - m] dx. \tag{6}$$

In our case $f(x) = r(\lambda_i)$ and the integrals are substituted by the following sums:

$$C_j(\tau) = \sum_{(i)} [r_j(\lambda_i) - r_j(\lambda_j + \tau)], \tag{4a}$$

$$C_{kj}(\tau) = \sum_{(i)} [r_j(\lambda_i) - r_j(\lambda_i + \tau)]^2 \tag{5a}$$

$$K_j(\tau) = \sum_{(i)}' [r_j(\lambda_i) - \bar{r}_j][r_j(\lambda_i + \tau) - \bar{r}_j]. \tag{6a}$$

It follows from the limiting conditions I, II, III that the sum $C_j(\tau)$ has also a normal distribution with an arithmetic mean C_j and dispersion σ_j^2 respectively equal to:

$$(7) \qquad \overline{C_j(\tau)} \approx \sum_{(i)} [\overline{r_j(\lambda_i)} - \overline{r_j(\lambda_i+\tau)}]; \quad \sigma_j^2 \approx \sum q^2 \{[\overline{r_j(\lambda_i)}]^2 + [\overline{r_j(\lambda_i+\tau)}]^2\}.$$

For the sums C_{kj} and K_j, according to equations (5a) and (6a) and conditions I and II, after neglecting the small terms of higher order, we obtain:

$$(8) \qquad \overline{C_{kj}(\tau)} \approx \sum_{(i)} [\overline{r_j(\lambda_i)} - \overline{r_j(\lambda_i+\tau)}]^2$$

$$\sigma_{kj}^2 \approx \sum_{(i)} 4q^2 [\overline{r_j(\lambda_i)} - \overline{r_j(\lambda_i+\tau)}] \{[\overline{r_j(\lambda_i)}]^2 + [\overline{r_j(\lambda_i+\tau)}]^2\}$$

and

$$(9) \qquad K_j \approx \sum_{(i)} [\overline{r_j(\lambda_i)} - r_j][\overline{r_j(\lambda_i+\tau)} - \overline{r_j}]$$

$$\sigma_{k_j}^2 \approx \sum_{(i)} \{[\overline{r_j(\lambda_i)} - \overline{r_j}]^2 \overline{r_j(\lambda_i)^2} + [\overline{r_j(\lambda_i+\tau)} - \overline{r_j}]^2 \overline{r_j(\lambda_i+\tau)^2}\} q^2.$$

Thus the distribution of C, C_k, K from equations (4a), (5a) and (6a) proves to be normal, provided the limitations I and II are given. Then their intersection point for the j and k classes is found by means of the equation:

$$\frac{1}{\sqrt{2\pi}\,\sigma_j} e^{-\frac{(r-\mu_j)^2}{2\sigma_j^2}} = \frac{1}{\sqrt{2\pi}\,\sigma_k} e^{-\frac{(r-\mu_k)^2}{2\sigma_k^2}}$$

After calculating its logarithm the equation takes the following form:

$$-\frac{(r-\mu_j)^2}{2\sigma_j^2} = \ln \frac{\sigma_j}{\sigma_k} - \frac{(r-\mu_k)^2}{2\sigma_k^2},$$

thus

$$(10) \qquad r_{1,2} = \frac{-b \pm \sqrt{b^2-4ac}}{2a}$$

where $a = \frac{1}{\sigma_k^2} - \frac{1}{\sigma_j^2}$,

$$b = 2\left(\frac{\mu_j}{\sigma_j^2} - \frac{\mu_k}{\sigma_k^2}\right),$$

$$c = \frac{\mu_k^2}{\sigma_k^2} - \frac{\mu_j^2}{\sigma_j^2} - 2\ln\frac{\sigma_j}{\sigma_k}.$$

The efficiency of each of the transformations C, C_k, K is measured by the value of the integral in (3). In this case it may take the following form:

(3a) $$p=\int_{-\infty}^{\eta_{j\,1,2}} e^{-\frac{\eta_j^2}{2}}\,d\eta_j+\int_{\eta_{k1,2}}^{\infty} e^{-\frac{\eta_k^2}{2}}\,d\eta_k,$$

where $\eta_{j,k}=\frac{r-\mu_{j,k}}{\sigma_{j,k}}$ is the coordinate of the normalized normal distribution. The value of p will be smaller when the limit

(11) $$\eta_{1,2_{j,k}}=\frac{r_{1,2}-\mu_{j,k}}{\sigma_{j,k}}$$

is greater in absolute value. In spite of the limiting conditions I, II and III, the analytical examination of the criterion (11) is still difficult, as the expressions for $\mu_{j,k}$ and $\sigma_{j,k}$ from (7), (8) and (9) take part in (10) in a relatively complicated manner. That is why two particular problems are treated in our further work.

IV. The functions $\overline{r_j(\lambda_i)}$ and $\overline{r_k(\lambda_i)}$ are connected by the determinated functional relation:

(12) $$\overline{r_k(\lambda_i)}=(1+\theta)\overline{r_j(\lambda_i)},$$

where $\theta=\text{const}$, $|\theta|\ll 1$.

V. The functions $\overline{r_k(\lambda_i)}$ and $\overline{r_j(\lambda_i)}$ are of such a type that their differences are of a random character.

(13) $$\overline{r_k(\lambda_i)}=\overline{r_j(\lambda_i)}+\Delta r_{j,k}(\lambda_i),$$

where $\Delta r_{j,k}(\lambda_i)$ — random function;

$\overline{\Delta r_{j,k}(\lambda_j)}=0$.

We shall first examine case IV.

It follows from equations (7), (8) and (9) that for μ, σ defined by (12) and for the three transforming functions C, C_k, and K the following expressions are valid:

$$\mu_k=(1+\theta)\,\mu_j,\ \sigma_k^2=(1+\theta)^2\,\sigma_j^2.$$

Then the equation (10) takes the form

$$r=\frac{b}{a}=\mu_j\frac{2(1+\theta)}{2+\theta}$$

assuming $\ln\sigma_k/\sigma_j\approx 0$, and (11), respectively:

(11a) $$\eta_{j,k}=\frac{\mu_j}{\sigma_j}\cdot\frac{\theta}{2+\theta}=\frac{\theta}{2+\theta}\cdot\frac{1}{V_j};\quad V_j=\frac{\sigma_j}{\mu_j}.$$

Therefore in this case the efficiency of the criterion η is inversely proportional to the coefficient of variance V and the comparative analysis is to be carried out by means of V_C, V_{C_K}, V_K. For this purpose the following ratios should be formed:

$$\omega_{C,C_K}=\frac{V_{C_K}}{V_C}=\frac{\sigma_{C_K}\cdot\overline{C}}{\overline{C}_K\cdot\sigma_C},\quad \omega_{C,K}=\frac{V_K}{V_C}=\frac{\sigma_K\cdot\overline{C}}{\overline{K}\cdot\sigma_C}.$$

With a view to equations (7), (8), (9) for ω_{C,C_K}:

$$\omega_{C,C_K}=\sqrt{\frac{\left(\sum_{(i)}|X_i-Y_i|\right)^2\cdot 4\cdot\sum_{(i)}(X_i-Y_i)^2(X_i^2+Y_i^2)}{\left[\sum_{(i)}(X_i^2+Y_i^2)\right]\left[\sum_{(i)}(X_i-Y_i)^2\right]^2}} \tag{14}$$

is obtained where, for the sake of simplicity, the substitutions $X_i=\overline{r_j(\lambda_i)}$, $Y_i=\overline{r_j(\lambda_i+\tau)}$ are used. The sum $\Sigma|X_i-Y_i|$ can also be presented as follows:

$$\sum_{(i)}|X_i-Y_i|=\sum_{(M_1)}(X_i-Y_i)+\sum_{(M_2)}(Y_i-X_i),$$

where M_1 is the set of i values for which $X_i>Y_i$, and M_2 is the set of i values for which $X_i<Y_i$. This way of presenting allows $\Sigma|X_i-Y_i|$ to be differentiated with respect to X_i and Y_i respectively.

In such a case the extremums of ω_{C,C_K} are determined by the condition:

$$\frac{\partial\omega_{C,C_K}}{\partial x_i}=0, \tag{15}$$

$$\frac{\partial\omega_{C,C_K}}{\partial y_i}=0,\ i=1,\ldots,n. \tag{15a}$$

The system (15) is equivalent to the following system:

$$\begin{aligned}&\{\pm 2\Sigma|X_i-Y_i|\cdot 4\cdot\Sigma[X_i-Y_i]^2(X_i^2+Y_i^2)+\{\Sigma|X_i-Y_i|\}^2[2(X_i-Y_i)(X_i^2+Y_i^2)\\&+(X_i-Y_i)^2 2X_i\}\{\Sigma(X_i^2+Y_i^2)[\Sigma(X_i-Y_i)^2]^2\}-[\Sigma|X_i-Y_i|]^2 4\\&\times\Sigma[(X_i-Y_i)^2(X_i^2+Y_i^2)]\}\cdot\{2X_i[\Sigma(X_i-Y_i)^2]^2\\&+[\Sigma(X_i^2+Y_i^2)][2\Sigma(X_i-Y_i)^2][2(X_i-Y_i)]\}=0.\end{aligned} \tag{16}$$

In (16) all sums are identical for the equation system where $i=1,\ldots,n$. Therefore (16) is a system of equations of the third power with respect to X_i. This system is to be satisfied, i. e. the n equations of the third power must be cancelled out by their roots. As in this case all $X_i>0$, the equations of the third power have only one real positive root, i. e. $X_i=\text{const}=X$.

Similarly, the condition $Y_i=\text{const}=Y$ can be obtained which satisfies the system (15a).

Therefore ω_{C,C_K} has an extremum at $X_i=X$, $Y_i=Y$.

The value of the extremum is

$$(\omega_{C,C_K})\,\text{ext}=2. \tag{17}$$

By way of example a check with the following values of X_i and Y_i: $x_1=a$, $x_2=2a$, $x_3=3a$, $y_1=2a$, $y_2=3a$, $y_3=a$ shows that the extremum is a maximum.

The following expression is obtained for the coefficient $\omega_{C,K}$

$$\omega_{C,K}=\sqrt{\frac{\left(\sum_{(i)}|\overline{X_i-Y_i}|\right)^2\sum_{(i)}\left[X_i^2(X_i-\bar{r}_j)^2+Y_i^2(Y_i-\bar{r}_j)^2\right]}{\sum_{(i)}(X_i^2+Y_i^2)\left[\sum_{(i)}(X_i-\bar{r}_j)(Y_i-\bar{r}_j)\right]^2}}. \tag{18}$$

In a way analogous to the one used for ω_{C,C_K} it is shown that $\omega_{C,K}$ has an minimum at $X_i=X$, $Y_i=Y$. As $\sum_{(i)}X_i=\sum_{(i)}Y_i$, it follows that at the extremum $X=Y$, but then $\lim_{X_i\to Y_i}\bar{r}=\frac{x+y}{2}$ and, consequently $|x-\bar{r}|=|y-\bar{r}|=\frac{|-y+x|}{2}$. The value of the minimum in this case is

$$(\omega_{C,K})\,\mathrm{ext}=2. \tag{19}$$

Finally, let us determine the ratio $\omega_{C,r}$, measuring the efficiency of C with respect to $\bar{r}_j$. According to I and II this ratio is

$$\omega_{C,r}=\sqrt{\frac{\left(\sum_{(i)}|X_i-Y_i|\right)^2}{\sum_{(i)}(X_i^2+Y_i^2)}}. \tag{20}$$

The magnitude of $\omega_{C,r}$ depends on the concrete structure of $r_j(\lambda_i)$. For instance, for the straight line $y=x$ the module-structure characteristic is given by the expression $C(\tau)=2\tau(T-\tau)$, while for the sine-shaped curve $y=\sin x$ this expression is $C(\tau)=8\sin\frac{\tau}{2}$. It is clear that for the straight line the value of the function $C(\tau)$ becomes greater than half the area between the straight line and the abscissa when $\tau>\frac{T}{2}\left(1-\frac{1}{\sqrt{2}}\right)$ and, for the sine-shaped curve, when $\sin\frac{\tau}{2}>\frac{1}{2}$. Our experience shows that for curves of the spectral reflective characteristic type a considerable range of τ exists where the condition $\Sigma|r_j(\lambda_i)-r_j(\lambda_i+\tau)|>n\frac{\bar{r}_j}{2}$ is fulfilled. In this case, as $\sum_{(i)}X_i^2=\sum_{(i)}Y_i^2<nX_{\max}^2$ and $\bar{r}_j>\frac{X_{\max}}{2}$ for $\omega_{C,r}$ there exists a range for which

$$\omega_{C,r}>\sqrt{\frac{n}{8}}. \tag{21}$$

So far we have examined the case defined by condition IV. Let us now assess the case defined by condition V. For this purpose it is sufficient to examine the difference $C_{(K)}-C_{(J)}$, $C_{K(k)}-C_{K(j)}$ and K_K-K_J. As the reflective characteristics $\bar{r}_k$ and $\bar{r}_j$ differ only in the random function which

has arithmetic mean equal to zero for a sufficiently large set of values of i, the following is obtained for the above differences:

$$(22) \qquad C_k - C_j = \sum_{(i)} |X_{K_i} - Y_{K_i}| - \sum_{(i)} |X_{j_i} - Y_{j_i}|$$

$$= \sum_{(M_1)} [\Delta X_{j_k}(i) - \Delta Y_{j_k}(i)] + \sum_{(M_2)} [\Delta Y_{j_k}(i) - \Delta X_{j_k}(i)] = 0$$

in accordance with condition II.
Similarly we obtain:

$$(23) \qquad |C_{k(k)} - C_{k(j)}| = \sum_{(i)} [\Delta X_{jk}(i) - \Delta Y_{j_k}(i)]^2 \neq 0.$$

$$(24) \qquad |K_k - K_j| = \sum_{(i)} [\Delta X_{j_k}(i)] [\Delta Y_{j_k}(i)] \neq 0$$

Equations (22), (23) and (24) show that for functions defined by condition V the module-structure characteristics have 0 efficiency, as opposed to C_k and K. This result can be considered as a weighting property of C which C_k and K do not possess to the same degree.

Discussion

1. When the reflective characteristics are used for their identification directly the algorithm exposed in item A furnishes the answer as to what the minimum number is of wavelengths $\lambda_{i\,(\min)}$ by means of which the appurtenance of new objects to a given set M of reference classes can be recognized. If the number of these classes is not too large, the necessary number of wavelengths $\lambda_{i\,(\min)}$ in which r is to be measured is comparatively small. This simplifies the measuring process and the analysis of reflective characteristics.

2. In the case where M contains many reference classes (for instance, several hundred) it is probable that the number of $\lambda_{i\,(\min)}$ shall be commensurable with the total number n of the sampled values of r. Here it is advisable to use some of the transforming functions C, C_k, K examined above.

The equations (17), (19) and (21) contain the basic results of the three transforming functions obtained so far. They show that there is a possibility for the module-structure characteristics, defined by equation (4), to have a better efficiency than the original functions and the transformations defined by equations (5) and (6). This efficiency results in a decrease of probability for type I and type II errors using the Bayes criterion for a minimum risk when the identification of r_j is carried out. This reduction of errors leads to possibilities for the decrease also of the minimum number of $C(\tau)$ values, by means of which the identification of the set M of reference classes with given reflective characteristics is realized. A better efficiency of c is therefore to be looked for in the range of the greater values of τ where the coefficient of variance V_c decreases considerably.

Table 1

λ / c. №	5	6	9	10	11	14	21	26	53	67	68	69	74	75	85	90	94
400	0.059	0.072	0.084	0.020	0.202	0.050	0.023	0.105	0.018	0.152	0.149	0.054	0.044	0.030	0.030	0.017	0.015
410	0.060	0.073	0.086	0.020	0.203	0.050	0.024	0.100	0.019	0.153	0.149	0.050	0.046	0.033	0.038	0.018	0.015
420	0.061	0.074	0.091	0.020	0.204	0.050	0.025	0.090	0.020	0.154	0.149	0.049	0.049	0.039	0.042	0.019	0.018
430	0.062	0.074	0.097	0.021	0.205	0.050	0.027	0.096	0.024	0.159	0.150	0.056	0.051	0.040	0.048	0.020	0.020
440	0.061	0.073	0.101	0.022	0.209	0.050	0.028	0.094	0.026	0.162	0.157	0.060	0.055	0.041	0.050	0.021	0.022
450	0.065	0.072	0.109	0.024	0.210	0.050	0.026	0.092	0.024	0.171	0.163	0.061	0.059	0.042	0.051	0.025	0.025
460	0.073	0.071	0.115	0.025	0.211	0.050	0.027	0.090	0.027	0.182	0.176	0.060	0.063	0.043	0.052	0.030	0.027
470	0.076	0.070	0.125	0.026	0.211	0.050	0.026	0.090	0.029	0.200	0.190	0.059	0.068	0.044	0.053	0.036	0.029
480	0.075	0.070	0.131	0.027	0.212	0.050	0.026	0.090	0.028	0.215	0.200	0.060	0.071	0.045	0.052	0.039	0.027
490	0.087	0.071	0.144	0.027	0.214	0.050	0.026	0.091	0.027	0.222	0.209	0.066	0.075	0.045	0.052	0.040	0.026
500	0.095	0.073	0.161	0.029	0.215	0.050	0.022	0.095	0.027	0.277	0.218	0.070	0.081	0.049	0.055	0.041	0.029
510	0.106	0.077	0.185	0.034	0.215	0.051	0.031	0.100	0.027	0.230	0.222	0.070	0.089	0.059	0.062	0.044	0.035
520	0.120	0.080	0.213	0.040	0.215	0.053	0.036	0.105	0.029	0.231	0.232	0.096	0.096	0.075	0.075	0.050	0.050
530	0.149	0.082	0.233	0.053	0.214	0.056	0.041	0.111	0.033	0.232	0.226	0.110	0.103	0.087	0.093	0.060	0.072
540	0.169	0.087	0.245	0.066	0.213	0.059	0.051	0.114	0.041	0.234	0.227	0.119	0.109	0.094	0.107	0.071	0.093
550	0.176	0.090	0.249	0.070	0.213	0.060	0.049	0.114	0.045	0.235	0.228	0.120	0.112	0.098	0.112	0.095	0.104
560	0.178	0.091	0.247	0.067	0.213	0.061	0.048	0.112	0.044	0.239	0.230	0.112	0.116	0.096	0.113	0.129	0.097
570	0.173	0.095	0.241	0.053	0.216	0.063	0.050	0.108	0.042	0.243	0.232	0.111	0.118	0.088	0.111	0.154	0.084
580	0.168	0.098	0.231	0.048	0.220	0.064	0.044	0.103	0.040	0.246	0.235	0.112	0.117	0.081	0.110	0.151	0.073
590	0.168	0.100	0.229	0.050	0.224	0.065	0.043	0.100	0.039	0.248	0.238	0.105	0.115	0.081	0.109	0.143	0.067
600	0.160	0.101	0.224	0.050	0.231	0.066	0.044	0.097	0.040	0.248	0.239	0.088	0.113	0.085	0.105	0.132	0.061
610	0.152	0.101	0.220	0.049	0.239	0.067	0.042	0.094	0.050	0.246	0.239	0.078	0.118	0.085	0.101	0.128	0.060
620	0.153	0.102	0.211	0.053	0.247	0.068	0.040	0.090	0.054	0.243	0.237	0.078	0.125	0.079	0.096	0.130	0.059
630	0.151	0.102	0.205	0.051	0.254	0.067	0.043	0.087	0.052	0.239	0.231	0.078	0.132	0.073	0.091	0.131	0.052
640	0.143	0.101	0.202	0.042	0.261	0.071	0.043	0.083	0.050	0.233	0.228	0.074	0.140	0.069	0.087	0.129	0.047
650	0.141	0.100	0.208	0.036	0.269	0.080	0.035	0.080	0.048	0.229	0.222	0.082	0.142	0.075	0.085	0.121	0.040
660	0.150	0.100	0.211	0.040	0.274	0.089	0.025	0.075	0.050	0.224	0.218	0.095	0.148	0.082	0.087	0.123	0.045
670	0.161	0.100	0.218	0.055	0.280	0.097	0.022	0.072	0.053	0.228	0.224	0.101	0.151	0.105	0.089	0.138	0.045
680	0.178	0.100	0.225	0.068	0.284	0.102	0.028	0.085	0.060	0.242	0.230	0.112	0.157	0.145	0.095	0.161	0.045
690	0.210	0.100	0.241	0.088	0.288	0.106	0.030	0.122	0.070	0.251	0.245	0.132	0.165	0.182	0.105	0.201	0.042
700	0.238	0.100	0.252	0.120	0.295	0.107	0.042	0.180	0.110	0.268	0.252	0.151	0.172	0.212	0.122	0.248	0.061
710	0.264	0.100	0.271	0.141	0.298	0.106	0.050	0.245	0.122	0.298	0.261	0.180	0.185	0.148	0.141	0.308	0.072
720	0.291	0.100	0.301	0.164	0.299	0.106	0.062	0.278	0.150	0.329	0.272	0.259	0.210	0.291	0.158	0.342	0.100
730	0.332	0.100	0.310	0.187	0.301	0.111	0.070	0.328	0.161	0.343	0.303	0.342	0.232	0.301	0.184	0.395	0.125
740	0.374	0.100	0.321	0.218	0.301	0.122	0.075	0.369	0.180	0.350	0.308	0.467	0.250	0.306	0.218	0.405	0.172
750	0.418	0.100	0.351	0.270	0.300	0.145	0.079	0.397	0.200	0.350	0.306	0.542	0.252	0.305	0.269	0.470	0.205
760	0.458	0.101	0.360	0.320	0.300	0.190	0.081	0.418	0.202	0.348	0.303	0.571	0.272	0.303	0.299	0.481	0.249
770	0.512	0.102	0.370	0.342	0.299	0.220	0.082	0.437	0.201	0.339	0.300	0.591	0.281	0.309	0.322	0.491	0.292
780	0.517	0.103	0.398	0.360	0.296	0.240	0.083	0.452	0.193	0.327	0.293	0.605	0.289	0.311	0.342	0.501	0.322
790	0.526	0.104	0.405	0.375	0.293	0.255	0.084	0.470	0.189	0.311	0.283	0.615	0.293	0.313	0.359	0.520	0.342

Here it is appropriate to deal with the following cases:

a) When τ is small, a correlation between the neighbouring values of r is possible to exist, i. e. the difference $r_j(\lambda_i) - r_j(\lambda_i + \tau)$ will not be a composition of independent random quantities. Then the equations (7), (8) and (9) will not be valid. However, a similar correlation could hardly be expected for $\tau > (5 \div 8)\Delta\lambda = 50 - 80$ nm because such a τ corresponds to a transition into a zone of a new hue. Because of that most values of C, C_k, K and their dispersions remain as defined in (7), (8) and (9).

b) As the efficiency of $C(\tau)$ is expected to be considerable when the τ values are higher, the following question is to be answered: When the set M is large, will there be a sufficient number of high values of C for the identification of the classes of M? The affirmative answer to this question

95	96	97	98	99	100	101	102	105	106	107	108	109	111	112	113	143
0.022	0.020	0.022	0.022	0.022	0.022	0.020	0.023	0.030	0.021	0.028	0.037	0.040	0.059	0.050	0.027	0.019
0.022	0.020	0.022	0.022	0.022	0.022	0.020	0.023	0.031	0.021	0.028	0.037	0.042	0.061	0.050	0.032	0.024
0.023	0.020	0.023	0.023	0.023	0.023	0.021	0.026	0.037	0.022	0.029	0.037	0.045	0.069	0.050	0.035	0.027
0.024	0.020	0.024	0.024	0.024	0.028	0.023	0.028	0.045	0.023	0.030	0.038	0.049	0.077	0.051	0.035	0.029
0.026	0.022	0.026	0.028	0.028	0.032	0.026	0.031	0.043	0.024	0.031	0.039	0.050	0.100	0.053	0.035	0.029
0.027	0.023	0.027	0.030	0.030	0.035	0.029	0.033	0.047	0.025	0.032	0.040	0.053	0.150	0.057	0.037	0.030
0.029	0.025	0.029	0.032	0.032	0.039	0.030	0.035	0.053	0.026	0.034	0.041	0.056	0.180	0.060	0.038	0.028
0.028	0.026	0.028	0.034	0.034	0.040	0.030	0.035	0.058	0.029	0.036	0.042	0.058	0.192	0.061	0.041	0.033
0.032	0.028	0.032	0.038	0.038	0.039	0 031	0.035	0.056	0.030	0.038	0.043	0.060	0.181	0.062	0.040	0.028
0.035	0.030	0.035	0.040	0.040	0.040	0.033	0.038	0.058	0.031	0.039	0.047	0.063	0.163	0.068	0.039	0.030
0.040	0.041	0.041	0.045	0.045	0.049	0.038	0.042	0.068	0.035	0.045	0.052	0.070	0.149	0.072	0.041	0.035
0.049	0.059	0.052	0.060	0.062	0.070	0.050	0.056	0.086	0.041	0.053	0.064	0.088	0.127	0.074	0.054	0.044
0.066	0.079	0.074	0.082	0.092	0.105	0 078	0.090	0.124	0.055	0.070	0.080	0.120	0.125	0.115	0.089	0.050
0.086	0.098	0.101	0.115	0.123	0.149	0.112	0.119	0.172	0.076	0.089	0.101	0.159	0.116	0.167	0.116	0.055
0.102	0.111	0.119	0.128	0.143	0.182	0.129	0.134	0.202	0.090	0.108	0.121	0.180	0.104	0.192	0.126	0.058
0.115	0.103	0.121	0.129	0.151	0.198	0.133	0.145	0.225	0.095	0.118	0.134	0.184	0.096	0.210	0.131	0.061
0.110	0.092	0.117	0.123	0.147	0.182	0.131	0.142	0.224	0.090	0.112	0.131	0.173	0.087	0.199	0.121	0.062
0.096	0.080	0.105	0.111	0.127	0.161	0.120	0.131	0.221	0.081	0.103	0.122	0.159	0.072	0.173	0.114	0.061
0.087	0.072	0.092	0.100	0.110	0.141	0.107	0.114	0.204	0.073	0.096	0.111	0.147	0.076	0.155	0.093	0.059
0.078	0.065	0.083	0.090	0.095	0.134	0.098	0.103	0.185	0.069	0.090	0.103	0.134	0.085	0.152	0.084	0.057
0.070	0.061	0.077	0.082	0.088	0.133	0.094	0.100	0.186	0.063	0.082	0.097	0.126	0.145	0.161	0.073	0.055
0.065	0.057	0.071	0.077	0.081	0.110	0.091	0.097	0.176	0.060	0.079	0.090	0.119	0.238	0.146	0.079	0.053
0.061	0.050	0.069	0.073	0.079	0.095	0.084	0.094	0.161	0.059	0.073	0.087	0.112	0.318	0.131	0.077	0.051
0.056	0.045	0.065	0.070	0.057	0.100	0.079	0.089	0.157	0.057	0.070	0 082	0.107	0.385	0.117	0.068	0.052
0.054	0.042	0.064	0.070	0.077	0.092	0.073	0.082	0.152	0.055	0.068	0.080	0.101	0.510	0.105	0.070	0.053
0.057	0.045	0.065	0.070	0.078	0.096	0.071	0.077	0.150	0.054	0.066	0.079	0.100	0.570	0.094	0.067	0.054
0.062	0.048	0.073	0.080	0.081	0.102	0.075	0.081	0.155	0.058	0.072	0.085	0.105	0.620	0.098	0.069	0.057
0.069	0.055	0.082	0.111	0.118	0.118	0.095	0.108	0.181	0.075	0.098	0.125	0.182	0.660	0.125	0.081	0.062
0.078	0.073	0.095	0.151	0.145	0.158	0.118	0.141	0.253	0.161	0.238	0.295	0.381	0.690	0.200	0.112	0.066
0.128	0.138	0.142	0.242	0.238	0.250	0.208	0.225	0.325	0.355	0.395	0.450	0.452	0.715	0.275	0.141	0.071
0.202	0.381	0.225	0.371	0.368	0.380	0.310	0.375	0.458	0.442	0.471	0.495	0.525	0.755	0.361	0.181	0.081
0.402	0.465	0.420	0.391	0.491	0.508	0.550	0.550	0.606	0.481	0.500	0.521	0.565	0.752	0.435	0.268	0.112
0.482	0.511	0.495	0.471	0.542	0.600	0.728	0.740	0.754	0.501	0.519	0.532	0.580	0.771	0.589	0.350	0.123
0.530	0.524	0.522	0.507	0.575	0.618	0.763	0.780	0.797	0.520	0 535	0.550	0.620	0.789	0.673	0.404	0.135
0.540	0.534	0.535	0 517	0.591	0.720	0.790	0.815	0.850	0.530	0.550	0.563	0.680	0.805	0.742	0.495	0.148
0.551	0.545	0.546	0.525	0.608	0.757	0.795	0.822	0.859	0.540	0.561	0.575	0.750	0.820	0.794	0.558	0.161
0.595	0.558	0.557	0.537	0.622	0.785	0.796	0.824	0.863	0.545	0.572	0.588	0.791	0.833	0.832	0.592	0.180
0.578	0.569	0.568	0.549	0.639	0.809	0.796	0.825	0.969	0.548	0.582	0.599	0.820	0.846	0.865	0.616	0.200
0.593	0.580	0.580	0.560	0.651	0.830	0.800	0.830	0.876	0.550	0.591	0.611	0.842	0.000	0.889	0.635	0.220
0.608	0.596	0.593	0.570	0.669	0.847	0.811	0.839	0.883	0.553	0.603	0.625	0.868	0.000	0.910	0.651	0.238

is implied in the following property of $C(\tau)$: it is steep for the small values of τ and rapidly reaches high values. Its steepness is approximately proportional to $\tau \cdot \frac{dr}{d\lambda}$.

The limiting conditions used to obtain the above results actually do not greatly restrict the problem because there are data indicating that conditions I and II really exist in the case of natural formations [2, 3]. Conditions IV and V show certain advantages of the module-structure characteristics in the identification of objects that are similar. This is actually the basic problem underlying each similar algorithm.

The algorithm described in item A and the module-structure characteristics are applied in the following example: the set M consists of 34 reflective

characteristics of deciduous and coniferous vegetation as well as grass areas (Table 1). Each reflective characteristics is formed by 40 values of r at each 10 nm in the range of 400-800 nm. These data were taken from paper [4]. The coefficient from condition II is assumed to be 0.02. The application of the algorithm from item A for M shows that the thirty-four classes of M are not identified by means of two-element combinations for λ_i, but that this is possible in 2212 three-element combinations. The same algorithm applied for $C(\tau)$ shows that there exist 29 two-element combinations for the τ values, by means of which the total set M is recognized. As the possible three-element combinations in this case are 9880 and the two-element ones for τ are 190 [$C(\tau)$ is symmetric], the ratios $\frac{2212}{9880}$ and $\frac{29}{190}$ are similar in value Therefore, it can be stated that in this case $C(\tau)$ gives results which are by one order better than $r_j(\lambda_i)$.

It remains to prove the possibilities of the transforming functions C, C_k and K for a set consisting of a considerably larger number of classes.

References

1. Yanev, T., G. Astardgian, Ch. Nachev. A set of signs and taking a decision in structural analysis of one-dimensional objects. — In: IV International Symposium of Complex Systems, Information and Control. Varna, 1973.
2. Fu, K. S., D. A. Langrebe, T. L. Phillips. Informational processing of agricultural data obtained through distance measurements. — TIEP, 1968, N X.
3. Kondratiev J., A. A. Grigoriev, O. M. Pokrovsky. The informational contents of data from space distance indication parametres of environment and natural resources. Ed. Lenin University, Leningrad, 1975.
4. Krinov, E. L. The spectral reflective capacity of the natural formations. Acad. Sci., USSR, Moscow, 1947.

Дискриминантный анализ отражательных характеристик естественных природных образований, использующий минимальное число длин волн

Т. К. Янев, Д. Н. Мишев

(Резюме)

Рассматривается вопрос о выборе и минимизации необходимого числа длин волн при измерении коэффициента отражения природных образований. Решение этого вопроса позволяет осуществить идентификацию спектральных отражательных характеристик $r_j(\lambda_i)$ данного множества M, состоящего из j классов объектов O_j, $j = 1, \ldots N$.

BULGARIAN ACADEMY OF SCIENCES

SPACE RESEARCH IN BULGARIA, 1

Sofia · 1978

Optimization of a Parallelepiped Discriminant Function at a Multidimensional Analysis

T. K. Yanev

When effecting a classificational analysis of stochastic subjects O_j, $j=1,\ldots N$, presented in the multidimensional space $S=\{x_i\}$, $i=1,\ldots,n$, the choice of a criterion is a basic stage for the quality of the deciding rule (discriminant function). Often the sum of the error probabilities from the 1st and 2nd genders serves as such a criterion. The minimum value of the sum is attained by the Bayes criterion of the minimum risk. As we know [1], this procedure, though well elaborated methodologically, entails considerable calculation difficulties, especially when the number of classes C_k, $k=1,\ldots,M$, formed by O_j, is considerable. In this case, even the linearized Bayes procedures, or the linear discriminant functions lose their effect in general, because a great number of linear discriminant functions are needed [1].

The simplest approach is, of course, the one in which the discriminant function is defined by simple in form volumes in the multidimensional space S. Such could be, by way of example, multidimensional parallelepipeds, spheres, ellipsoids, and the like. In this instance, the deciding rules are simplified considerably, and in the case of the multidimensional parallelepiped they are reduced to a system of simple inequations. On account of such a simplification of the deciding rule, the value of the risk function R increases.

This paper treats the problem of optimization of the parameters of the constant limits (discriminant functions) of the classes in space S, in order to obtain a minimum value of R (Naturally, this minimum value is higher than the value which could be obtained by the Bayes discriminant procedure).

As we know [3], in the general case the risk function has the following form:

$$R=\int_{\Gamma}\sum_{k=1}^{M}\left[\sum_{m=1}^{M}p_m C_{mk} f(X/\mu_m)\delta(\gamma_k/X)\,dX\right], \tag{1}$$

where: $X(x_1, \ldots, x_n)$ is the current vector-realization, p_m is the a priori probability of the m-class subject appearance, $f(X/\mu_m)$ is the density of the probability of the m-class subject appearance in the volume $dX = \prod_{i=1}^{n} dx_i$,

$$C = \begin{vmatrix} C_{11} \ldots C_{1M} \\ \ldots\ldots\ldots \\ C_{M1} \ldots C_{MM} \end{vmatrix}$$

is a payment-off matrix with elements C_{km}, equal to the price of the error when relating the x to the m-class, at the k-class subject availability.

$\delta(\gamma_k/X)$ is a unit function, equal respectively to:

1, when X is in the region Γ_k of the k-class,

0, when X is in another region.

It is usually accepted that $C_{mm}=0$, and that condition will be taken into consideration in this paper later on.

Under the Bayes criterion of the minimum risk, regions Γ_k depend on the index m, i. e. $\Gamma_k = \Gamma_k(m)$, and are determined by the equation:

$$p_k C_{mk} f(X/\mu_k) = p_m C_{km} f(X/\mu_m). \tag{2}$$

Equation (2) shows that the minimum risk is attained by the introduction of flexible limits, depending on the pair of indices (k, m) of the comparable classes. This condition makes the analysis complicated because, in the general case, regions (m) are strongly nonlinear and multidimensional.

At constant limits and normal distribution $f/x/\mu/$, which we accept further on, equation (1) has the form:

$$R = \sum_{j=1}^{M} \sum_{k=1}^{M} C_{kj} p_k + \left[\frac{1}{(\sqrt{2\pi})^n} \sum_{j=1}^{M} \int_{a_{1j}}^{b_{1j}} \ldots \int_{a_{nj}}^{b_{nj}} \left\{ \sum_{\substack{k=1 \\ k \neq j}}^{M} p_k C_{kj} \frac{e^{-\frac{1}{2}(X-\mu_k)^T K_k^{-1}(X-\mu_k)}}{\sqrt{|K_k|}} - (M-1) C_{jk} p_j \frac{e^{-\frac{1}{2}(X-\mu_j)^T K_j^{-1}(X-\mu_j)}}{\sqrt{|K_j|}} \right\} dX \right] = T_1 + T_2, \tag{3}$$

$$I_2 = \frac{1}{(\sqrt{2\pi})^n} \sum_{j=1}^{M} \sum_{\substack{k=1 \\ k \neq j}}^{M} C_{kj} p_k \int_{a_{1j}}^{b_{1j}} \ldots \int_{a_{nj}}^{b_{nj}} \frac{\exp\left[-\frac{1}{2}(X-\mu_k)^T K_K^{-1}(X-\mu_k)\right]}{\sqrt{|K_k|}} dX, \tag{3a}$$

$$I_1 = \sum_{j=1}^{M} \sum_{\substack{k=1 \\ k \neq j}}^{M} C_{kj} p_k - (M-1) \sum_{j=1}^{M} \int_{a_{1j}}^{b_{1j}} \ldots \int_{a_{nj}}^{b_{nj}} \frac{\exp\left[-\frac{1}{2}(X-\mu_j)^T K_j^{-1}(X-\mu_j)\right]}{\sqrt{|K_j|}} dx, \tag{3b}$$

K — covariational matrix.

In the general case, the limits a_{ij} and b_{ij} of the multidimensional parallelepiped can change independently on one another. At the R optimi-

zation by (3) this means the introduction of $2n$ parameters of the optimization. Further on we will accept the following limiting conditions:

$$a_{ij} = \mu_{ij}(1-q), \tag{4}$$
$$b_{ij} = \mu_{ij}(1+q),$$

i. e. we accept that the limiting surface of the j-class is a parallelepiped which is centrally symmetric to the point described by the tip of the vector, μ_{ij}, and its magnitude changes with one and the same coefficient of proportion q along all the axes of the space S. Under this condition, it is seen in (3b) that I_1 is a monotonously decreasing function of q, when the values of μ_{ik}, K_k, M are fixed, because the normal distribution is positively defined in the multidimensional volume $(-\infty, \infty)^n$ and to each dq corresponds an increase of the integration region volume of the integral in (3b), and $dI_1 < 0$ is accordingly obtained.

Analogously, we obtain from (3a) that I_2 is a monotonously increasing function of q.

Also, the following limit relations follow from (3a) and (3b):

$$I_{1_{\min}} = \lim_{q\to\infty} I_1 = 0; \quad I_{2_{\max}} = \lim_{q\to\infty} I_2 = \sum_{j=1}^{M} \sum_{\substack{k=1 \\ j\neq k}}^{M} C_{kj} p_k$$

and therefore, because of monotonous change of I_1 and I_2, and since

$$R_{\max} = \lim_{q\to\infty} R = \lim_{q\to\infty} I_2 = R(q=0), \tag{5}$$

then relations (5) show that in the region $(-\infty, \infty)^n$ the risk function R has at least one minimum. The values of q, which correspond to $R_{\min}$, can be determined by the equation

$$\partial R/\partial q = 0. \tag{6}$$

In the relatively simple case, when signs x_i describing the subjects O_j of a given class are independent on one another, i. e. when the covariational matrix of the class is diagonal, the multiple integrals in (3) are given as a product of one-fold integrals, and a possibility is offered for condition (6) to be obtained by differentiation under the sign of a one-fold integral. Then we obtain for (6):

$$\frac{\partial R}{\partial q} = -\frac{1}{(\sqrt{2\pi})^n} \sum_{j=1}^{M} \sum_{\substack{k=1 \\ k\neq j}}^{M} C_{kj} p_k \sum_{l=1}^{n} \left\{ -\frac{[\mu_{lj}(1+q)-\mu_{lk}]}{\sigma_{kl}^3} \right. \tag{6a}$$

$$\left. \times \prod_{\substack{i=1 \\ i\neq l}}^{n} \left(\frac{1}{\sigma_{ki}} \exp \cdot \left\{ -\frac{1}{2}[\mu_{ij}(1+q)-\mu_{ik}]^2/\sigma_{ki}^2 \right\} \right) - \frac{\mu_{lj}(1-q)-\mu_{lk}}{\sigma_{kl}^3} \prod_{\substack{i=1 \\ i\neq l}}^{n} \left(\frac{1}{\sigma_{ki}} \exp \right. \right.$$

$$\times\left[-\frac{1}{2}\{\mu_{ij}(1-q)-\mu_{ik}\}/\sigma_{ki}^2\right]\Bigg\} \cdot \frac{1}{(\sqrt{2\pi})^n}\sum_{j=1}^{M}(M-1)C_{jq}p_j\sum_{i=1}^{n}2\left\{\frac{-\mu_{ij}q}{\sigma_{ji}^3}\prod_{\substack{l=1\\ l\neq i}}^{M}\frac{1}{\sigma_{jl}}\exp.\right.$$

$$\left.\times\left[-\frac{1}{2}\frac{(\mu_{ij}q)^2}{\sigma_{ji}^2}\right]\right\}.$$

It is obvious from (6a) that the direct determination of the dependence $R(q)$ by the equation (3) should probably prove to be easier, even in this simplified case, than the solution of (6a), or of (6) respectively. For that purpose it is appropriate to calculate the integrals in (3a) by the Monte Carlo method, which in this case offers considerable simplification, because the integration regions are simple volume-parallelepipeds orientated along the coordinate axes.

The deciding rule at constant limits, defined by a multidimensional parallelepiped, is reduced to a verification of the inequation system:

$$a_{ij}\leq x_i\leq b_{ij}, \quad i=1,\ldots,n, \quad j=1,\ldots,M, \tag{7}$$

where $X(x_1,\ldots,x_n)$ is a vector-realization, subject to classification.

If (7) is satisfied for certain j and for all i, it is accepted that x belongs to the j-class of the multitude M.

The mean risk function (averaged for all the meanings of j) is determined under this deciding rule by equation (3); it can be obtained also by (3) only for the j-class, though without summing along index j.

If the change of the limits a_{ij} and b_{ij} of the multidimensional parallelepiped occurs depending on more than one parameter, then equation (6) is transformed into a system of partial derivatives of R towards these parameters.

Of course, the deciding rule with constant limits can be applied and can be optimized for other relatively simple limiting surfaces, as for example a multidimensional sphere, an ellipsoid, etc. In this case inequation (7) would become more complicated. Some complications would also appear in the calculation of R by (3). It is possible that the complexity of the deciding rule should become commensurable with the linear deciding rules.

On account of the rather great simplification of the deciding rule at a multidimensional parallelepiped, the risk R at the classificational analysis increases. If an acceptable risk R_{acc} is given, this risk in the general case will be realized with the greatest number of signs, i. e. the dimensionality of S would be greatest, under a deciding rule based on a multidimensional parallelepiped. This compromise would probably be acceptable at considerable data files, where it could happen that it was more profitable economically to measure more signs x_i but needing considerably lesser time of computing analysis. In particular, such a situation can appear when studying the natural formations of the Earth surface according to spectral reflective characteristics. In that case, to obtain data by a greater number of wavelengths would involve a single complication of the equipment for obtaining reflective characteristics (increase in the number of channels for obtaining spectral information). This single complication of the design would

be compensated by its multiple applications in collecting and processing considerable data files.

Equation (3) shows that the risk function depends on the number M of the classes and increases with the increases of M. That is why it is convenient to introduce the quantity "relative risk" for the comparative analysis of different in volume sets of classes:

$$(8) \quad \xi = R/\sum_{m=1}^{M}\sum_{\substack{k=1\\k\neq m}}^{M}\int_{-\infty}^{\infty}\ldots\int_{-\infty}^{\infty}[p_m C_{mk} f(X/\mu_m) + p_k C_{km} f(X/\mu_k)]\,dx$$

$$= R/2\sum_{m=1}^{M}\sum_{\substack{k=1\\k\neq m}}^{M} C_{mk} p_m.$$

Taking into consideration equation (5), we find that ξ changes in the interval $0 \leq \xi \leq 0.5$. The value $\xi = 0.5$ corresponds to the maximum indeterminacy in the class identification. The same value is obtained not only when the region determining the limits of the classes is with a zero volume or, respectively, is infinitely great, but also when all the distributions are equal. In this case we also have complete indeterminacy.

The maximum indeterminacy is obtained also in the case when $M \to \infty$. This is due to the fact that in equation (3) the integral values tend toward zero, because in the constant volume of integration there is a part of the infinite normal multidimensional distribution which tends toward zero.

References

1. Libenson, M. H., A. Y. Hessin, B. A. Yanson. Automation of space image interpretation. Moscow, Energia, 1975.
2. Milenkiy, A. B. Signal classification in indeterminacy conditions. — Sovetskoe radio, Moscow, 1975.

Оптимизация параллелепипедной дискриминантной функции в многомерном анализе

Т. К. Янев

(Резюме)

При классификации стохастических объектов основным критерием точности классификации является функция риска. В настоящем работе исследована проблема минимизации функции риска, когда границы классов стохастических объектов принимаются за многомерные параллелепипеды. Процедура минимизации охватывает параметры этих параллелепипедов.

BULGARIAN ACADEMY OF SCIENCES

SPACE RESEARCH IN BULGARIA, 1

Sofia · 1978

Power Autocorrelative Function

T. K. Yanev

The spectral reflective characteristics (SRC) of the natural formations are obtained practically as a discrete sequence of values $r(\lambda_i), i=1, \ldots, n$ of the reflective index of the formation. This permits the SRC description through the vector tip $X(x_1, \ldots, x_n)$ in the finite multidimensional space with dimensionality n, in which the subject descriptive signs are $x_i \equiv r(\lambda_i)$. SRC are stochastic functions because of the natural dispersion of the formation parameters. This property of theirs necessitates the use of statistical probability methods of the SRC classification even when the measurement errors are so small as to be neglected. From the point of view of minimization of the probability R for an error of Ist gender ("omission"), or an error of 2nd gender (erroneous identification "false alarm"), most suitable proves to be the Bayes method of the minimum risk at the SRC classification analysis. In the general case, when the autocorrelative SRC matrix is not diagonal, the analytical conclusions become very difficult. But in some particular cases it is possible to formulate relatively simple criteria of the risk function R magnitude at the determination appurtenance of the vector-observation $X(x_1, \ldots, x_n)$ to one of the two classes — k or m. For instance, the risk function simplifies considerably at the following limiting conditions:

a) Signs x are independent (particularly $n=1$),

b) SRC of the two vector-realizations are connected with the relation: $r_m(\lambda)=(1+\Theta)r_k(\lambda)$, $\Theta=\text{const}\ll 1$.

c) k- and m-classes have normal distributions with parameters $\mu_{k_i}, \mu_{m_i} = (1+\Theta)\mu_{k_i}$, $\sigma_{k_i} = V\mu_{k_i}$, $\sigma_{mi} = V\mu_{k_i} = V(1+\Theta)\mu_{k_i}$, where μ_{k_i} is the mathematical expectation of $r_k(\lambda_i)$, and σ_{k_i} is the $r_k(\lambda_i)$ variance. The constant V is the variational index. As shown in [3], under these conditions the risk function R is measured with a normalized normal distribution having a coordinate equal approximately to

$$\eta = \Theta/V \tag{1}$$

(after neglecting the high powers of Θ).

As in that case, R is determined by the integral $\frac{1}{\sqrt{2\pi}} \int_{-\infty}^{\infty} e^{-\eta^2/2} dy$, $\eta<0$, then the value of R is smaller at a great absolute value of η.

Of course, these limiting conditions are quite strong (condition (b) in particular), but they provide a possibility for analytical conclusions through the criterion (1). They can serve as an orientation for the situation in the general case of the SRC nondiagonal covariance matrix.

The space of $X(x_1, \ldots, x_n)$ can be formed not only through $r(\lambda)$, but also by the $r(\lambda)$ transformations with a suitable operator. Such a transformation has justification of performance only when the risk function value could be reduced in the transformed space. Paper [3] shows that the autocorrelative transformations:

$$C_M(\tau_j) = \sum_{i=1}^{n} | r(\lambda_i) - r(\lambda_i + \tau_j) |, \quad \tau_j = \Delta\lambda \cdot j, \quad j = 1, \ldots, n/2, \quad \Delta\lambda = \lambda_{i+1} - \lambda_i = \text{const}, \tag{2}$$

$$C_k(\tau_j) = \sum_{i=1}^{n} [r(\lambda_i) - r(\lambda_i + \tau_j)]^2, \tag{3}$$

improve the risk function for the cases described by the limiting conditions (a), (b) and (c) with the increase of the $|\eta|$ value. The transformation (3) is given by Kolmogorov [1] and the transformation (2) is defined in [2].

This paper examines the generalization of (2) and (3), namely:

$$C(\tau_j) = \sum_{i=1}^{n} [| r(\lambda_i) - r(\lambda_i + \tau_j) |]^N, \quad N = 1, \ldots, \infty. \tag{4}$$

We shall accept equation (1) as an effectivity criterion of this transformation. The studies in paper [3] show that C_k from equation (3) leads to a smaller value of $|\eta|$ than C_M from equation (2). In the general case this justifies the examination of the ratio

$$\Omega = \frac{\eta_{N-m}}{\eta_N} = \frac{\Theta_{N-m} V_N}{\Theta_N V_{N-m}}. \tag{5}$$

Taking into consideration the limiting condition (b) and equation (4), we obtain the small parameter Q_n by the relation

$$C_m^{(N)}(\tau_j) = (1 + \Theta)^N C_K^{(N)}(\tau_j). \tag{6}$$

If we neglect the high powers of Θ in (6), we would obtain $\Theta_N = N\Theta$ and then

$$\Theta_N / \Theta_{N-m} = N/(N-m). \tag{7}$$

In order to study the V_{N-m}/V_N ratio it is necessary to determine the expressions for μ_{C_N} and σ_{C_N} of $C^{(N)}$ for an arbitrary N. This can be realized by the use of the definition equation (4) and of the dispersion equation of a normal distribution composition.

(8) $$y=\sum_i a_i x_i,$$

$$\sigma_y^2=\sum_i a_i^2\sigma_{x_i}^2 .$$

In equation (4) the lth realization r_l (λ_l) of a given class can be expressed as follows:

(9) $$r_l(\lambda_l)=\overline{r(\lambda_l)}+\Delta r_l(\lambda_l),$$

where $\overline{r(\lambda_l)}$ is the mathematical expectation of r in λ_l for the examined class. $r_l(\lambda_l+\tau_j)$ is expressed analogously:

(9a) $$r_l(\lambda_l+\tau_j)=\overline{r(\lambda_l+\tau_j)}+\Delta r_l(\lambda_l+\tau_j).$$

Taking into consideration that there follows from condition b) that $V\ll 1$, the high powers of Δr_l can be neglected and then we obtain after the substitution of (9) and (9a) in (4) in a first approximation:

(10) $$C_l^{(N)}\approx\sum_{i=1}^{n}[(\bar{x}_i-\bar{y}_i)^N+N(\bar{x}_i-\bar{y}_i)^{N-1}(\Delta x_{i_l}-\Delta y_{i_l})],$$

where it is marked for convenience: $x_i=r(\lambda_i)$, $y_i=r(\lambda_i+\tau_j)$.

It follows from equation (8) and (10) and condition b) that:

(11) $$\overline{C^{(N)}}=\sum_{i=1}^{n}(\bar{x}_i-\bar{y}_i)^N,$$

(12) $$\sigma_{C_N}^2=V^2N^2\sum_{i=1}^{n}(\bar{x}_i-\bar{y}_i)^{2(N-1)}(\bar{x}_i^2+\bar{y}_i^2).$$

The ratio V_N/V_{N-m} is expressed by equations (11) and (12) in the following way:

(13) $$\frac{V_N}{V_{N-m}}=\frac{N}{N-m}\sqrt{\frac{\left[\sum_{i=1}^{n}(\bar{x}_i-\bar{y}_i)^{N-m}\right]^2\left[\sum_{i=1}^{n}(\bar{x}_i-\bar{y}_i)^{2(N-1)}(\bar{x}_i^2+\bar{y}_i^2)\right]}{\left[\sum_{i=1}^{n}(\bar{x}_i-\bar{y}_i)^{2(N-m-1)}(\bar{x}_i^2+\bar{y}_i^2)\right]\left[\sum_{i=1}^{n}(\bar{x}_i-\bar{y}_i)^{N}\right]^2}}.$$

There follows from (5), (7) and (13) that the ratio (5) has the form

(14) $$\Omega=\sqrt{\frac{\left[\sum_{i=1}^{n}(\bar{x}_i-\bar{y}_i)^{N-m}\right]^2\left[\sum_{i=1}^{n}(\bar{x}_i-y_i)^{2(N-1)}(x_i^2+\bar{y}_i^2)\right]}{\left[\sum_{i=1}^{n}(\bar{x}_i-\bar{y}_i)^{2(N-m-1)}(\bar{x}_i^2+\bar{y}_i^2)\right]\left[\sum_{i=1}^{n}(x_i-\bar{y}_i)^{N}\right]^2}},$$

or it can be written by triple indices:

(14a) $$\Omega=\frac{\sum\limits_{i,j,k}(a_i^{N-m}a_j^{N-m}a_k^{2(N-1)}b_k)}{\sum\limits_{i,j,k}(a_i^{N}a_j^{N}a_k^{2(N-m-1)}b_k)}, \quad \begin{matrix} i=1,\ldots,n,\\ j=1,\ldots,n,\\ k=1,\ldots,n,\end{matrix}$$

$$a_i=|\bar{x}_i-\bar{y}_i|, \quad b_k=\bar{x}_k^2+\bar{y}_k^2.$$

In order to evaluate the effectivity of the N increase, it is necessary to examine the extremums of Ω with respect to N (for that purpose equation (14a) is suitable), and the extremum of the structure of $r(\lambda)$ (equation (14) suits the purpose). In particular, the following system should be solved:

(15a) $$\partial\Omega/\partial x_i=0,$$

(15b) $$\partial\Omega/\partial y_i=0, \quad i=1,\ldots,n,$$

(15c) $$\partial\Omega/\partial N=0.$$

There follows from (14) that (15a) and (15b) contain x_i and y_i in a symmetric manner, i. e. the results from (15a) will be valuable also for (15b). We obtain for (15a) in a developed form:

(16a) $$\frac{1}{2}\cdot\frac{\partial\Omega}{\partial\bar{x}_i}=\{\sqrt{A}B(N-m)(\bar{x}_i-\bar{y}_i)^{N-m-1}+A[(N-1)(\bar{x}_i-\bar{y}_i)^{2N-3}(\bar{x}_i^2+\bar{y}_i^2)$$
$$+(\bar{x}_i-\bar{y}_i)^{2(N-1)}\bar{x}_i]\}CD-\{C\sqrt{D}N(\bar{x}_i-\bar{y}_i)^{N-1}$$
$$+D[(N-m-1)(\bar{x}_i-\bar{y}_i)^{2(N-m)-3}\cdot(\bar{x}_i^2+\bar{y}_i^2)+(\bar{x}_i-\bar{y}_i)^{2(N-m-1)}\cdot\bar{x}_i]\}AB,$$

where

$$A=\left[\sum_{i=1}^{n}(\bar{x}_i-\bar{y}_i)^{N-m}\right]^2, \quad C=\sum_{i=1}^{n}(\bar{x}_i-\bar{y}_i)^{2(N-m-1)}\cdot(\bar{x}_i^2+\bar{y}_i^2),$$

$$B=\sum_{i=1}^{n}(\bar{x}_i-\bar{y}_i)^{2(N-1)}\cdot(\bar{x}_i^2+\bar{y}_i^2), \quad D=\left[\sum_{i=1}^{n}(\bar{x}_i-\bar{y}_i)^{N}\right]^2.$$

The sums A, B, C, D in (16a) are independent of the index i, and $\bar{x}_i$ as well as $\bar{y}_i$ takes part in the remaining part of the equation in an equal manner for the different values of the index i. Therefore, the system (16a) is reduced to a single equation, representing a polynomial of x. Still, if we take the difference $\bar{x}_i-\bar{y}_i$ by module (according to the definition equation (4)), then $\bar{y}_i$ participates symmetrically to x for each i and in all equations. That is why, the simultaneous satisfaction of (16a) and (16b) demands:

(17) $$\bar{x}_i=\bar{y}_i.$$

But it follows from the definition equation (4) that if (17) is fulfilled then $x=\text{const}$.

The derivative (15) is expressed in a developed form by the equation

$$(16b)\quad \frac{\partial\Omega}{\partial\bar{N}}=\frac{\sum_{i,j,k,p,q,r}\left[a_i^{N-m}a_j^{N-m}a_k^{2(N-1)}a_p^{N}a_q^{N}a_r^{2(N-m-1)}b_k^{2}l_n\frac{a_ia_ja_k^2}{a_pa_qa_r^2}\right]}{\left[\sum_{i,j,k}a_i^{N}a_j^{N}a_k^{2(N-m-1)}b_k\right]^2}=0.$$

$(i, j, k, p, q, r)=1, \ldots, n$.

Obviously (16b) is annulled also by the condition $x=\text{const}$. Therefore, Ω from (14a) has an extremum and it appears when $r(\lambda)=\text{const}$.

At $N\to\infty$ the sequence $\{(\bar{x}_i-\bar{y}_i)\}$, $i=1, \ldots, n$ tends to the sequence $\{0, 0, \ldots, 0, (\bar{x}_j-\bar{y}_j)_{max}\}$, $j=1, \ldots, K$, where K is the number of the biggest and equal in size differences $(\bar{x}_j-\bar{y}_j)_{max}$. That is why the conditions for an extremum of (14a) are realized at $N\to\infty$.

A direct verification can prove that the extremum defined by the system (15a), (15b) and (15c) is a maximum.

Conclusions

According to the results obtained, each power autocorrelative function, defined by equation (4), diminishes the risk function of equation (1) when its power index increases. But we should not forget that these results have been obtained under the following limiting conditions: $V\ll 1$, $r_k(\lambda)=(1+\Theta)r_m(\lambda)$, $\Theta\ll 1$. The increase of the power index N leads to an increase of the role of the neglected terms in the development of μ_{C_N}, σ_{C_N} and $(1+\Theta)^N$; for example, at $N>10$ their contribution in some cases could be higher than 30—40 per cent even when $V=0.05$ and $\Theta=0.05$. Nevertheless, at relatively small values of N, it is possible to look for an optimum of each concrete set of classes. It is probable that this optimum would be shifted towards the great values of N, when for each one of the M-classes there exists at least one wavelength λ, in which this class has the highest values of $r(\lambda)$, compared with the other classes.

If we take into consideration the higher powers of Δx and Δy in the expression for $C_l^{(N)}$ in equation (10), then the distribution of $C_l^{(N)}$ would not be a composition of normal distribution, therefore equations (11) and (12) would not be valuable as sufficient parameters of that distribution description. This would complicate considerably the analytical conclusions for the effectivity of transformations (4).

Notwithstanding the fact that the analytical conclusions of this paper are quite limited, they do provide grounds to expect good effectivity of transformation (4). The verification of this effectivity in the general case of multidimensional distributions should be realized as the file of primary information for $r(\lambda)$ has to be transformed into a file of power autocorrelative functions, according to (4), and the Bayes procedure of the minimum risk or some other convenient criteria should be applied to this file.

References

1. Kolmogorov, A. N. Energy scatter at local isotropic turbulence. — Comp. Rend. Acad. Sci. USSR, 32, 1941.
2. Yanev, T., G. Astardgyian, Ch. Nachev. Obtaining a multitude of signs and decision-making at the structural analysis of one-fold subjects. — In: IVth Polish-Bulgarian Symposium on Big Systems of Information and Management, Varna, X, 1973.
3. Yanev, T., D. Mishev. Discriminant analysis of natural formations by a minimum number of measurements in different wavelengths of the spectral reflective characteristics. — In: Cospar, Varna, VI, 1975.

Степенная аутокорреляционная функция

Т. К. Янев

(Резюме)

Исследованы свойства аутокорреляционной функции вида

$$C(\tau_j)=\sum_{i=1}^{n}[r(\lambda_i)-r(\lambda_i+\tau_j)]^m,$$

где m — целое положительное число, τ_j — шаг корреляции,
λ_i — независимая переменная, $r(\lambda_i)$ — зависимая переменная.

Показано, что применение $C(\tau_j)$ в классификационном анализе стохастических сигналов типа $r(\lambda_i)$ уменьшает функцию риска при нормальном распределении $r(\lambda_i)$.

BULGARIAN ACADEMY OF SCIENCES

SPACE RESEARCH IN BULGARIA, 1

Sofia · 1978

Fault Structures Obtained by Geological Interpretation of Space Images

H. B. Spiridonov, V. S. Djepa-Petrova

New trends in studying various natural phenomena and objects appear within the development of aero- and space methods of Earth investigations through outer space. Particularly great are the possibilities for the Earth sciences of geology, geomorphology, soil studies, hydrology, and the like. Space images processing provides for the accumulation of enormous quantities of statistical material which broadens our knowledge in the field of Earth sciences. Particularly great are the prospects revealed by the statistical processing of fault structures obtained by a visual method of geological interpretation of space images.

This paper uses space multizonal images provided by the American technological satellite ERTS-1 for the purpose of statistical processing of fault structures. The photographs were obtained in four spectral ranges: 0.5—0.6, 0.6—0.7, 0.7—0.8, and 0.8—1 μm, i. e. in the visible and the near-infrared regions of the spectra. The geographical coordinates of the photographic centre are: N 41°42/E 026°03; N 41°40/E 026°05. The space photograph comprises a surface of $S=33502$ sq. km. It embraces the South-Eastern part of the Bulgarian territory, the Eastern Rhodope Mountains included, as well as most of Western and Eastern Thrace, which are part of Greece and Turkey.

The Eastern Rhodope block, which is the subject of the geological interpretation, is part of the Rhodope Median Massif. Four structural complexes participate in its tectonic configuration, namely: Archaen, Proterozoic, Caledono-Hercynian and Alpine. They form analogous structural plans [2]. The Eastern Rhodope morphostructural block has been the theatre of intense tectonic manifestations, mostly of a hereditary nature [2]. The different lithostratigraphical complexes are affected by multiple faults, in which the sequential structural decomposition of the massif is reflected.

All the tectonic disturbances have been separated irrespective of the corresponding structural plans, during the interpretation of the space photographs. The fault disturbances have been mapped (Fig. 1) on the basis of

the geological fault structures interpreted (mainly on channels 5 and 7, with wavelengths 0.6—0.7 and 0.8—1.1 μm). The map obtained was compared with the available tectonic, geological, neotectonic, geomorphological, soil and seismo-tectonic maps. Analogous Greek and Turkish maps were also

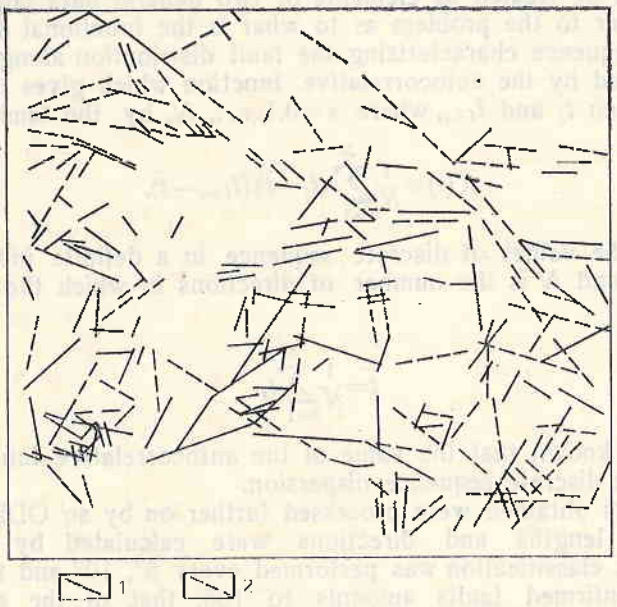

Fig. 1. Map of the fault structures obtained by the geological interpretation of the space images
1 — confirmed faults; 2 — suggested faults

used. Most of the tectonic structures, interpreted on the space images, confirmed the already known fault zones and faults. In addition, new structures unknown to the geological maps were identified. Together with the definite selection of most fault structures, a considerable number of them had provoked certain doubts. That is why these structures were divided conventionally into two categories: a) faults definitely identified on the space photographs, and b) suggested faults not definitely discerned on the space photographs. On the other hand, the space images embrace territories of neighbouring countries for which we are not in possession of detailed cartographical geological materials. This fact also contributed to adopting the decision for differentiating between the two fault categories.

The two fault structure categories — confirmed and suggested — obtained from the interpretation of the space multizonal photographs, were used for statistical processing with the specialized electronic system of automated digital recording for photogrammetric and cartographic information.

The set obtained with coordinates of the two fault-structure categories can be used further on for computer processing. For that purpose the essential indicators which characterize the multitude of faults are determined by the direction (d_i) and length (l_i) of the fault, where:

(1) $$d_i = \operatorname{arctg} |(Y_{2i} - Y_{1i})/(X_{2i} - X_{1i})|,$$

(2) $$l_i = \sqrt{(X_{2i} - X_{1i})^2 + (Y_{2i} - Y_{1i})^2},$$

For the purposes of mathematical statistics, direction (d_i) and fault length (l_i) can be treated as elements of two general data populations.

The answer to the problem as to what is the functional dependence in the discrete sequence characterizing the fault distribution along the direction can be obtained by the autocorrelative function which gives the statistical relation between t_i and $t_{i+\tau}$, where $\tau = 0.1, \ldots, N$, by the familiar formula:

(3) $$K(\tau) = \frac{1}{N} \sum_{i=1}^{N} (t_i - \bar{t})(t_{i+\tau} - \bar{t}),$$

where t_i are the values of discrete sequence in a definite interval at fault classification, and N is the number of directions in which the classification is performed.

(4) $$\bar{t} = \frac{1}{N} \sum_{i=1}^{N} t_i.$$

It is well known that the value of the autocorrelative function at $\tau = 0$ determines the discrete sequence dispersion.

The results obtained were processed further on by an ODRA computer. All the fault lengths and directions were calculated by formulae (1) and (2). A fault classification was performed every 5°, 10° and 15°. The total sum of the confirmed faults amounts to 165, that of the assumed ones being 80. Some additional data for computer processing are given in Table 1.

Table 1

Faults	Number n_i	Summary length/km L	Maximum length/km l_{max}	Minimum length/km l_{min}	Density $\varrho = \frac{L}{S}$ [km^{-1}]
Confirmed	165	1845.71	42.57	4.13	0.055081
Suggested	80	1261.88	37.75	4.98	0.03487

The classification results and the fault structure distribution are shown on histograms and fault rose (Figs. 2, 3). Both the histograms and the fault structure rose have been worked out at every 5°. The classification and the distributon of the two fault types have been effected in the range from 0° to 180°.

If we analyze thoroughly the fault distribution at intervals of 5° in the range indicated for the confirmed ones, and for the suggested faults — by histograms and the rose, we shall find considerable saturation (tips of the histograms) in the following directions: 0°, 25°, 40°, 50°, 90°, 105°, 125° and 175°. An interesting fault concentration may be observed in the North-Eastern quadrant in the range between 10° and 60° both for the confirmed and for the suggested faults. A constant fault background is present here and its tips are outlined in directions of 10°, 25°, 40°, 50°. The highest concentration for the faults suggested is in the same quadrant in a direction of 20°.

A particularly big saturation of faults is found in the interval from 90° to 95° and the concentration maximum is attained at 90°. If compared to (1) there would be almost full coincidence both along the amplitude of scattering (here it is of about 15°) and in the fault concentration in the

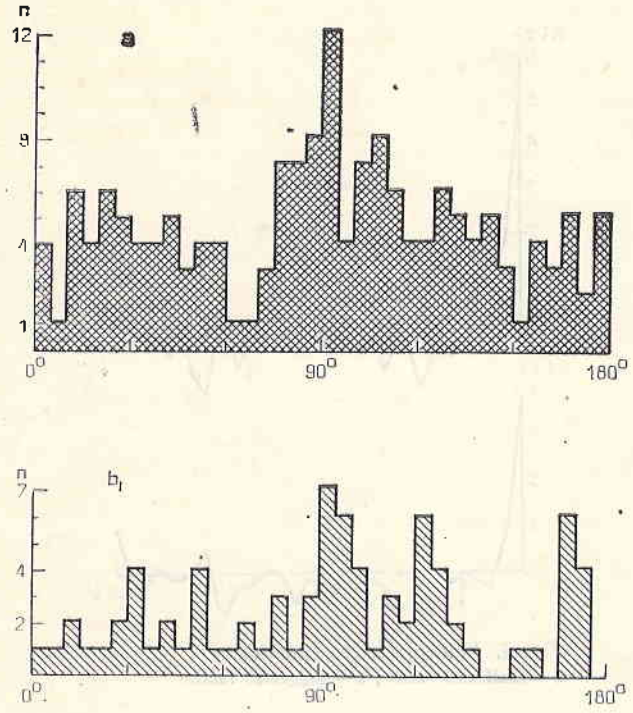

Fig. 2. Histograms :
a — confirmed faults ; b — suggested faults

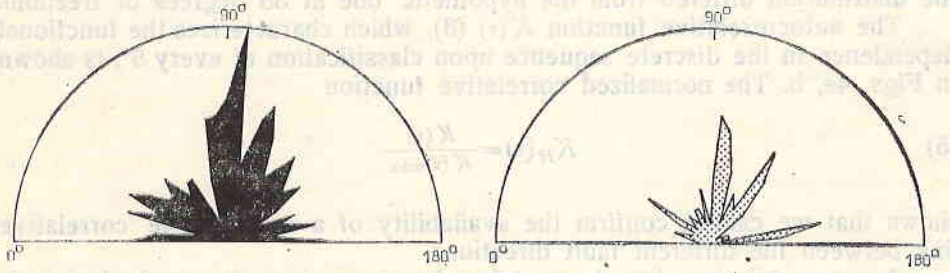

Fig. 3. Rose of the fault structures :
a — confirmed ; b — suggested

East-Western direction. This conclusion relates to both confirmed and suggested fault structures.

As far as the remaining interval concentrations in the North-Western quadrant are concerned, they completely correspond to the main fault structure with directions of 120°—130° and 150°—170° (1).

One basic problem arises here, namely: the determination of the specific distribution of the faults examined and the respective verification with the help of experimental data available. The histograms worked out (Fig. 2a, b) show mixed distribution. The verification of the uniform distribution

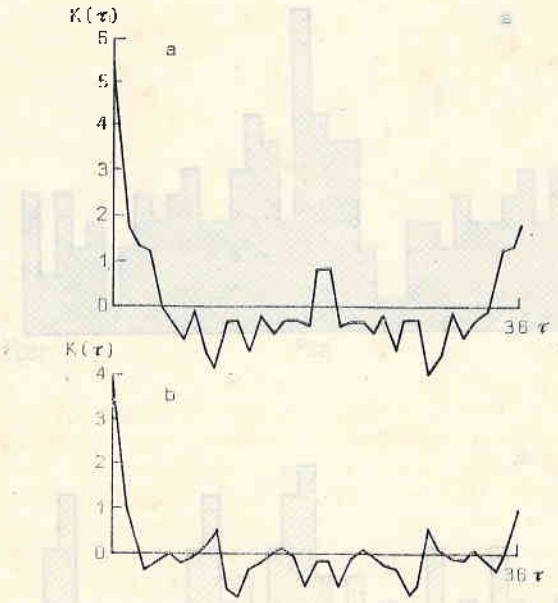

Fig. 4. Autocorrelative function:
a — confirmed faults ; b — suggested faults

availability was performed according to the X_i-square criterion (3) which had shown that with a probability higher than 0.995 we could confirm that the distribution differed from the hypothetic one at 35 degrees of freedom.

The autocorrelative function $K(\tau)$ (3), which characterizes the functional dependence in the discrete sequence upon classification at every 5°, is shown in Figs. 4a, b. The normalized correlative function

(5) $$K_H(\tau)=\frac{K(\tau)}{K(\tau)_{max}}$$

shows that we cannot confirm the availability of a considerable correlative link between the different fault directions.

A successful step has been taken by processing the geological fault structures obtained by the visual method of interpretation of the multizonal space images of the South-Eastern Bulgarian territory. Such a processing has not been carried out until now. A comparison with (1) shows that the interpreted fault structures reflect correctly the total distribution of the fault systems in the Eastern half of the Balkan Peninsula. This fact proves once again that the suggested program of processing fault disturbances has been correctly worked out and is being successfully interpreted.

References

1. Бончев, Е. Проблеми на българската тектоника. С., Техника, 1971.
2. Йовчев, И., А. Атанасов и др. Тектонски строеж на България, С., Техника, 1971.
3. Румшисткий, Л. С. Математическая обработка результатов эксперимента, М., Наука, 1971.
4. Spiridonov, H. B., D. Stoychev, M. Katskov. Results from the geological interpretation of space images of the East Rhodope mountains. — In: COSPAR, Varna, 1975.

Разломные структуры, полученные при геологическом дешифрировании космических изображений

Х. Б. Спиридонов, В. С. Джепа-Петрова

(Резюме)

В результате визуального структурного дешифрирования многозональных космических изображений, охватывающих Восточные Родопы, выделяются линейные разломные структуры. На основе этих структур составлена карта разломных нарушений. Полученные линейные структуры подразделяются на две категории: а) достоверно отдешифрированные разломы, и б) предполагаемые разломы. Эти две категории разломов используются дальше для статистической обработки специализированной электронной системой автоматической цифровой регистрации фотограмметрической и картографической информации. Распределение разломных структур исследуется методами математической статистики.

BULGARIAN ACADEMY OF SCIENCES

SPACE RESEARCH IN BULGARIA, 1

Sofia · 1978

Tentative Morphostructural Interpretation of Space Images of the Eastern Rhodope Mountains

I. N. Vaptsarov, H. B. Spiridonov

The People's Republic of Bulgaria has initiated organizational and practical activities on environmental studies through space means. Most interesting and promising results have recently been obtained in the interpretation of space photographs made for geological and geomorphological studies.

The information obtained has been assessed as unique in its specific features and in its considerable precision in the information on the geological and tectonic structure of the country, hence in the structural control of a number of exogenic and endogenic ore deposits.

The first results of the geological and the geomorphological interpretation of space images for a part of the Bulgarian territory were reported at the Plenary Meeting of COSPAR (Varna, 1975). The results of fault tectonics studies and their importance to establishing the size, position and characteristics of the block structures have been demonstrated [1]. The specific ring volcanic structures, genetically connected with the fault-block structure in the eastern part of the Rhodope region, have been selected.

This paper deals with some preliminary data about the structure of the above-mentioned territory, resulting from the morphological interpretation of the space images. The landscape method of interpretation, which makes it possible to establish the main features of the morphostructural characteristics of the region in order to determine the taxonomic differentiation of the principal and secondary morphostructures of the block type, has been used in this case. Aerial photographs and geological, geomorphological, topographic and tectonic maps, as well as field studies were also taken into consideration in order to obtain a complete characteristic and a more detailed description.

Space images obtained by the American satellite ERTS-1 were used as initial material. Most successful are the pictures obtained in the 5th and 7th channels with wavelengths of 0.6—0.7 μm and 0.8—1.1 μm. These photographs have served for the interpretation not only of the Eastern Rhodope morphostructure, but also for the neighbouring territories of Northern Greece and North-Western Turkey (Eastern Thrace).

The space images interpretation of the Eastern Rhodope area reveals certain features indicative of the deep structure of the Earth's crust. These features are manifested by the clearly outlined relief elements and the river network, and, particularly, by the abrupt landscape changes, the phototone of which is closely connected with the different morphostructures. The distinctive zones between the different morphostructures manifest themselves in different manners. In some cases they have linear contours, coinciding with the steep slopes of the flanks (e.g. along the Xanthi fault of the Aegean sea), whereas in other cases a phototone change is to be observed, due to the change in the type of rock complexes in the different morphostructures. The contour of the Pliocene and Quaternary morphostructures appear on the space images most clearly. It is much more difficult to select the morphostructures formed during the Paleogene, and those of recent times, involved in an intensive uplift. In some cases their detection on the space photographs becomes easier because of the presence of linearly orientated ring volcanic structures. Some complications appeared in the boundary parts, especially in inherited depressions, where the different typological landscape units are not of a linear nature but have a complex configuration. The space images interpretation was made with the help of additional interpretation of relief features: orientation of the river network, direction of the watersheds, slightly observable changes of the phototone, and also with the help of all the available geological, geomorphological, tectonic, soil and similar maps, as well as by ground-based field studies.

The interpretation of the space photographs established not only the main morphostructures which reflect the deep structure of the Earth's crust in the Eastern Rhodope region, but also the secondary structural forms embraced by the main morphostructures. This concerns both the positive and the negative morphostructures.

Based on the different relief features and the landscape (density of relief dismemberment, valley-river network plan, lineamentary manifestation reflected in the outlines of ridges and river valleys, anomaly sectors in watershed configuration, and the landscape zones), the following main morphostructures have been established (Fig. 1):

I. Central-Eastern Rhodope low and middle-mountain domed block uplift, composed of crystalline rocks of the pre-Hercynian basement.

II. Marginal, inherited or inversed in recent times, late Alpine depressions, characterized by low-mountain, hill-ridge or valley relief, representing the alluvial-pluvial foot of the mountain morphostructures.

The Central-Eastern Rhodope domed block uplift takes a median place between the main morphostructures. It manifests itself as an independent unit with linear contours and relatively monotonous middle and low-mountain relief with moderate erosional dismemberment. The river-valley network is adapted to its configuration, as the main rivers are of the encircling type (Arda and Kroumovitsa) or of radial type, orientated from its central part to the periphery (the Bjala reka river, the rivers flowing toward the Aegean Sea, etc.).

To the East, the Central-Eastern Rhodope domed block uplift is limited by clear-cut slope flanks, well observable on the space photograph. The northern boundary is relatively clear, too. To the west (to the Momchil-

grad depression), this uplift is outlined by a series of oval volcanogenic structures. To the east, the block uplift is distinguished from the "Ergene" depression by its more dark-grey uneven phototone. Here the boundary is of a complex type (broken), and follows approximately the margin between

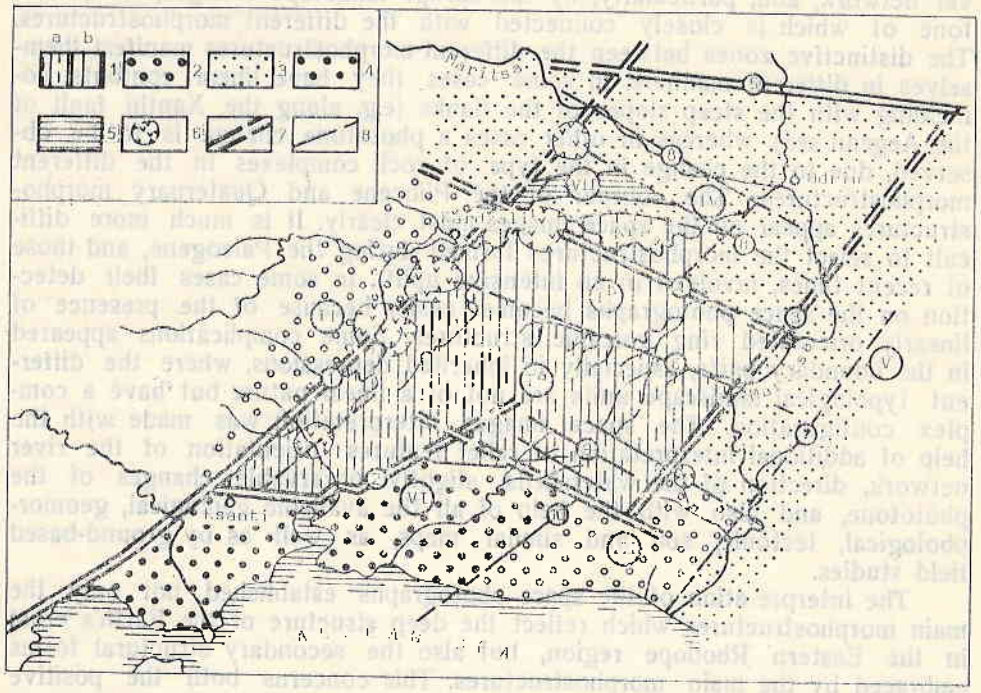

Fig. 1—Morphostructural scheme of the Eastern Rhodopes

Main morphostructures: 1—Central Eastern Rhodopian Arc — block uplift (I): 1^a Southern block, mid-mountainous; 1^b—Northern block, low-mountainous; 2—peripheral depressions with Late Alpine deposits of inverse development in the Neogene-Quaternary with Upper Paleogenic sediments and volcanics; Momchilgrad morphostructure with low-mountainous and hilly relief (II), Dimotica morphostructure with similar relief (III); 3-peripheral depressions with Late Alpine deposits with inherited development, with Upper Paleogenic and Neogenic sediments: Maritsa heterogenic morphostructure with hilly and plane relief (IV); "Ergene" morphostructure with hilly and plane relief (V); 4—peripheral depression with Late Alpine sediments of Pliocenic and Quaternary deposits; Aegean morphostructure with lowland relief (VI).
Second-range morphostructures: 5—Ibredjack horst within the Maritsa depression; 6—ring volcano-structures

Fault structures: 7—first range: Xanthi-Kroumovgrad fault (1); Gjumjurdjina fault (2); Eastern Thrace fault (3); Kamidol fault (4); Maritsa fault (5); 8—second-range faults; Bjala reka faults (6); Dimotica fault (7), Harmanli fault (8), Muglenik fault (9), Tirnava fault (10)

the crystalline basement and the Upper Paleogene and the Neogene-Quaternary sediments which fill the depression.

The Central-Eastern Rhodope domed uplift is unevenly delevelled. It comprises two clearly distinguished blocks: Southern and Northern. The Southern middle mountain block is deeply dismembered by a dense river network. Its avarage altitude is between 1,000 m and 1,200 m. The Northern block is less uplifted, a moderately dismembered low-mountain type with an average altitude of 750-800 m. Both morphostructures are separated by the Bjala reka dislocation, to which the Bjala reka valley is also orientated [2]. This dislocation, according to the space photographs, continues in a western direction.

From all the marginal late Alpine depressions, most clearly expressed is the Momchilgrad depression which has a complex configuration of a heterogeneous type, manifested in the contemporary relief and successfully interpreted on the space photographs. It comprises a relatively monotonous, slightly dismembered relief of sedimentary-tufogenic deposits, ring contours of volcanogenic structures, and isolated top parts of the intragraben horsts.

The Low Thracian depression (Ergene), which appeared in Alpine time with thick deposits of the Neogene-Pleistocene age, according to the available data, is demonstrated as a well expressed independent morphostructure. This morphostructure is characterized by a slight dismemberment clearly observable on the space photographs.

More to the south of the Eastern Rhodope block morphostructure a superimposed young Aegean depression can be distinguished, particularly compensated by Neogene and especially by Pleistocene alluvial-proluvial deposits. The boundary between the Eastern Rhodope morphostructure and the Aegean depression is represented by a normal fault.

To the East of the Aegean depression, the Dimotikon morphostructure with an inverse development during the neotectonic epoque is satisfactorily outlined. It comprises clearly depicted secondary block and ring volcanic morphostructures with a characteristic radial river network.

The Maritsa depression is distinguished to the north of the Eastern Rhodope domed uplift. This is a complexly built heterogeneous morphostructure. It comprises several linear elongated negative and positive secondary morphostructures in a north-western direction, which agree with the plan of the hydrographic network. The linear orientation of the structural forms in a north-western direction is closely connected with the diagonal network of the fault zones. The Harmanli fault zone is most clearly observed on the space photographs. The component block-fault morphostructures within the limits of the Maritsa depression form a different phototone landscape which can be clearly observed on the multizonal space images.

All the morphostructures of the eastern part of the Rhodope massif are of a block type and are separated from one another by faults with north-western, north-eastern and sublatitudinal direction, clearly distinguished on the space photographs. The subparallel faults form sets with a constant and definitely determined direction. Some of the faults show fragmentary activation, not only in space but also in time, testified by the geological studies, i. e. they are long-living faults with an ancient set up, as e. g. the faults of Eastern Thrace, Xanthi-Kroumovgrad, Maritsa, etc. Some of them are related to the igneous activity during the Alpine tectono-magmatic cycle, accompanied by base metal mineralizations: Zvezdel-Galenit, Madjarovo, Lozen and other ore fields and zones.

The advantages obtained from the space photographs interpretation for the purposes of the morphostructural studies of the Eastern Rhodope Mountains are beyond dispute. They can be used to distinguish the main morphostructures which can be further studied in a more detailed manner by other methods as well, field studies included.

A positive assessment can also be made of the interpretation of faults with the aid of space photographs.

References

1. Spiridonov, H. B., D. Stoychev, N. Katskov. Results from the Geological Interpretation of Space Images of the East Rhodope Mountains. — In: COSPAR, Varna, 1975.
2. Боянов, Ив., Б. Маврудчиев, Ив. Вапцаров. Върху структурно-формационните особености на част от Източните Родопи. — Изв. Геолог. и-т, XII, С. БАН, 1963.

Предварительная морфоструктурная интерпретация космических изображений Восточных Родоп

И. Н. Вапцаров, Х. Б. Спиридонов

(Резюме)

В настоящей работе излагаются предварительные представления о структурном строении Восточных Родоп, полученные в результате дешифрирования морфоструктур космических изображений. При решении поставленной задачи использовались космические изображения, полученные от американского технологического спутника ЕРТС-1. Самыми удачными оказались снимки, сделанные в диапазон 0,6—0,7 μm и 0,8—1,1 μm.

Дешифрирование космических изображений в обхвате Восточньх Родоп позволяет выявить признаки, свидетельствующие о глубинном строении земной коры и раскрывающиеся в ясно очерченных линейных элементов рельфа и сети рек, особенно в резких сменах ландшафта, чей фототон тесно связан с различными морфоструктурами.

На основании различных признаков рельфа и ландшафта выделены следующие главные морфоструктуры:

1) Центрально-восточнородопское низко- и среднегорное сводово-блоковое поднятие, сложенное кристаллическими породами догерцинского фундамента.

2) Периферийные, унаследованные или инверсные в новейшее время позднеальпийские депрессии, имеющие низкогорный, холмисто-грядовой или низинный рельеф, представляющие аллювиально-пролювиальные подножия горных морфоструктур.

BULGARIAN ACADEMY OF SCIENCES

SPACE RESEARCH IN BULGARIA, 1

Sofia · 1978

On the Utilization of the Spheric Ion Traps in Floating Potential Regime of Their Analyzing Grids

S. K. Chapkunov

The floating potential regime of the outer analyzing grid of the three-electrode spheric ion trap is of a great interest and reveals possibilities for a broad application of this type of sensor during direct space-probe measurements. A possible application of this operation regime is the employment of the spheric ion trap as a measuring device of ion (electron) density in the composition of a specialized satellite complex for low frequency and very low frequency measurements. In that case, the supply of any kind of oscillations to the outer parts of the satellite sensor is not recommended because even the disturbances through the general source of feeding in this frequency range will discredit the measurements. On the other hand, when applying a linearly changing voltage to the analyzing outer grid of the trap — to the point of the voltampere characteristics at which the potential of the plasma (the outer grid has a floating potential) corresponds to a current determined by the ions contained around the trap, and when we know this current the ion concentration can be determined directly. That is why this regime is to be preferred in combined magnetic and electrostatic measurements (see [1]), where the experimental purity depends on the absence of impeding factors — plasma-induced potentials in the case.

The aim of the article is to examine the conditions under which the three-electrode spherical ion trap may be applied as a measurer of the ion concentration, under conditions of floating potential of the analyzing electrode of the transducer.

The necessity of regime control of the floating potential is apparent, i. e., it is necessary to measure the isolated outer grid potential of the trap with respect to the satellite body. But in order to have such a control it is necessary to know the limits of that potential change.

In the ideal case (a definite floating potential of the absolutely isolated outer grid from the satellite body) the following circumstance will be operative: $i_e = i_i$, i. e.:

(1) $$a_i e n_i S_i V_0 \left(1 - \frac{2e\varphi_f}{M_i V_0^2}\right) = a_e e n_e S_e \cdot \frac{\overline{V_e}}{4} \exp\left(\frac{e\varphi_f}{kT_e}\right).$$

In (1) the quantities relating to the ion composition of plasma are denoted by indices i, the index e is used for those related to the electron component, a is the portion of the corresponding current due to the punching of the grids, S is the accumulation surface for the corresponding charged particles, M_i is the ion mass, V_0 is the velocity of satellite movement, and φ_f is the floating potential.

The above equation takes into consideration the fact that $V_i < V_0 \ll V_e$, i. e. the average satellite velocity exceeds the thermal ion velocity and is insignificant compared to the corresponding average electron velocity. Because of that the ion current has a purely conventional specifics (does not depend on the ion temperature), while the electron current is thermal, i. e. it does not depend on the satellite velocity — therefore $S_i = \pi r^2$, $S_e = 4\pi r^2$ which is a direct sequence of the above circumstance (r is the radius of the trap outer grid).

If α_1 and α_2 are the trasparency indices of the inner and outer grid of the trap, then:

$a_i = 1 - a_2$ the part of the ions that will fall on the envelope;

$a_e = 1 - a_2 + a_2(1 - a_2) = 1 - a_2^2$ the part of the electrons that will fall on the envelope.

Moreover, quantity $\frac{V_0 M_i}{2} = e\varphi_{\text{ret}}$ where φ_{ret} is the retarding potential of the corresponding M_i type ions. The main thermal velocity of electrons is $\overline{V_e} = \left(\frac{2kT_e}{m_e}\right)^{1/2}$, then equation (1) takes the form:

(2) $$V_0\left(1 - \frac{\varphi_f}{\varphi_{\text{ret}}}\right) = \frac{1}{2}(1 + a_2) \cdot \left(\frac{2kT_e}{m_e}\right)^{1/2} \exp\left(\frac{e\varphi_f}{kT_e}\right).$$

In the general case we obtain

(3) $$\ln\left(1 - \frac{\varphi_f}{\varphi_{\text{ret}}}\right) = A_1 + A_2 \cdot \varphi_f$$

where A_1 and A_2 are constants, depending on V_0 and T_e. The examination of this dependence is of interest since it is closely connected with the orbital data of the satellite. This will probably be done in a future study.

As our main purpose is to study the real conditions under which our trap will operate, we have to find out the influence of the real resistance in the potential measurer connected to the outer grid. Obviously, this resistance R_{In} connected between the trap lattice and the satellite body will influence the outer grid potential approach to the subject potential. This is due to the current being generated in the measurer by the difference $\varphi_f - \varphi_S$ (φ_S — satellite potential). The current ring is closed through the plasma surrounding the satellite and the trap, so that its value is determined also by the current carriers concentration in the vicinity of the subject (specifically, by the dynamic resistance of the sphere and the contact resistances trap-plasma and satellite-plasma). The influence of the real input measuring resistance, when neglecting the contact resistances, is calculated by the expression:

$$(4)\qquad \ln\left\{1-\frac{\varphi_f}{\varphi_{ret}}-\frac{\varphi_f-\varphi_S}{R_{in}+\dfrac{\varphi_{ret}}{(1-a_2)en_iS_iV_0}}\cdot\frac{1}{(1-a_2)en_iS_iV_0}\right\}=A_1+A_2\varphi_f.$$

The member $\dfrac{\varphi_{ret}}{(1-a_2)en_iS_iV_0}$ has ohm dimensionality and is plasma resistance in a concrete case (familiar composition and concentration). Equation (4) takes the form (3) when the trap envelope is isolated ($R_{in}\to\infty$). Upon short circuit ($R_{in}=0$) φ_f equalizes with φ_S, and equation (4) becomes an equation of satellite potential (without taking the photoeffect into consideration). But as the dependence which is used to represent the ion current is valid only for relatively low body potential (under 1 volt), the above equation cannot be used to determine the satellite potential.

We are analyzing below the R_{in} influence for a concrete case: $V_0=7.25$ km/s; $T_e=2500°$K (ionospheric satellite with circular orbit, flying at an altitude of about 400 km over the Earths' surface) (Table 1).

When $R_{in}=10^8$ ohms we use dependence $\varphi_S\approx\dfrac{k\cdot T_e}{e}\ln\left(\dfrac{T_eM_i}{T_im_e}\right)^{1/2}$ to determine the potential φ_s. We adjust the concentration values and the respective temperatures of the charged particles to correspond to altitudes at which the given type of ions is predominant.

The last column of Table 2 shows the percentage error, compared to the case when $R_{in}\to\infty$. We see that for concretely selected conditions the error does not exceed 5 per cent. Within the concentration decrease the status is preserved, as T_i, or T_e respectively, increases. Obviously, in controlling the floating potential in the upper atmosphere, an input resistance of the measurer of an order of 10^8 ohms is completely sufficient to obtain unspoiled results. As indisturbed conditions for concentration measurements exist only when the trap does not measure within the satellite trace, it is clear that in the general case it is necessary to use two identical ion traps which have to work either simultaneously or in temporal sequence.

Table 1: $R_{in}\to\infty$

Transforming ion	φ_{ret} [V]	φ_f [V]	φ_f/φ_{ret}
O^+	4.4	—0.705	—0.160
He^+	1.1	—0.625	—0.57
H^+	0.275	—0·512	—1·87

Table 2: $R_{in}=10^8$ ohms

Transforming ion	φ_s [V]	n_i [cm^{-3}]	φ_f [V]	% error
O^+	—1.18	10^6	—0.708	0.43
He^+	—1.1	10^4	—0.650	4.15
H^+	—1.1	10^4	—0.525	2.35

The preliminary results of the ion concentration measurements from the "Intercosmos-14" satellite confirm the logic presented above for the influence of R_{in}.

Upon recording the ion collector current I_k of the trap with a floating potential of the outer grid, the ion concentration can be determined by using the dependence:

$$n_i = \frac{I_k}{\alpha_1 \alpha_2 \pi r^2 e V_0 (1 - \varphi_f/\varphi_{ret})}. \tag{5}$$

Table 1 shows that neglecting the term $(1-\varphi_f/\varphi_{ret})$ leads to an error increasing with the mass decrease of the recorded ions. Notwithstanding the fact that equations (1)÷(4) have been deduced without taking the ion thermal velocities into account (whose influence increases within the mass weight decrease), it is clear that (5) is closer to the actual situation than the accepted φ_f/φ_{ret}.

References

1. Fahleson, V. et al. Radio Science, 6, 1971, 2, 233—245.

Использование сферических ионных ловушек в режиме плавающего потенциала анализирующей решетки

С. К. Чапкынов

(Резюме)

В настоящей работе предложен метод для определения ионной концентрации по данным, полученным от сферических ионных ловушек, у которых внешняя решетка находится под плавающим потенциалом. Рассмотрены условия работы ловушки при плавающем потенциале и определенном воздействии реального сопротивления между внешним электродом ловушки и поверхностью спутника. Предложено аналитическое выражение для определения ионной концентрации, в котором неизвестными являются коллекторный ток, плавающий и задерживающий потенциалы ловушки.

BULGARIAN ACADEMY OF SCIENCES

SPACE RESEARCH IN BULGARIA, 1

Sofia · 1978

Electrophotometric Equipment for Ground-Based Studies of Airglow Emissions from the Upper Atmosphere

M. M. Gogoshev, S. K. Chapkunov

1. Introduction

The spectrum of airglow emissions from the upper atmosphere contains a continuum of atomic lines and molecular bands. The intensity of these lines and bands is very variable. First of all, there is an essential difference between day and night glow. This difference is due to the photodissociation and photoionization and to the related excitation which is observed only during the day. The night emissions are mainly products of recombination processes. The intensity of the emissions is also a function of the geographic and geomagnetic latitudes, and of the solar and geomagnetic activity. Consequently, the intensity of the optical emissions changes within broad limits. For example, the red oxygen line with a length of 6300Å at calm conditions during the night has an intensity of 20-60 Rayleighs approximately [1, 2]. Upon geomagnetic activity, however, the intensity is highly increased. In subauroral regions this intensity can reach a value of 10^8R [3]. Some other lines, e. g. the nitrogen 5199Å--5202Å, have extremely low intensity, always in the limits of 1 to 10 R [4]. Such low values has also the hydrogen line H_α [5]. This big range of emission variations leads to great difficulties at the construction of the equipment for their simultaneous measurement. Let us note here that the simultaneous measurement of the emissions can be made with a spectrograph or a spectrometer. The spectrograph cannot, however, give the time variations of the intensity which are very important for explaining the physical processes of the glow. The spectrometer has a low spectral resolution and low sensitivity.

It is known that the best time resolution and a good spectral resolution is achieved by electrophotometric equipment with filters used to measurements of the atmospheric emissions. An essential defect of this equipment is, however, the limitation of the set of simultaneously measured spectral bands and lines. With the electrophotometers referred to in the litera-

ture and used for this purpose, only 3—5 lines are usually measured. Besides that, every line is measured by two filters, so that for one photometer designed for measuring 5 separate lines the number of the filters is 10, and if we also add the two necessary positions for the dark current and one for calibration, we shall have 13 positions. Any further increase in the number of the filters is of no avail, as the time interval for one full cycle is greatly increased and consequently the emissions measured cannot be compared.

The present paper describes electrophotometric equipment for investigation of some nocturnal atmospheric optical emissions, as carried out in the Central Laboratory for Space Research at the Bulgarian Academy of Sciences.

2. Function and Basic Requirements on the Equipment

As stated above, the simultaneous measurement of a large set of emissions is impossible. With the electrophotometer made in our laboratory it is possible to measure three emissions simultaneously: the nebular red oxygen 6300Å line, the auroral green oxygen 5577Å line and the first negative system of N_2^+ about the 4278Å line. As for the choice of these three lines, we are proceeding from the following considerations:

1. The red oxygen 6300Å line is emitted in the *F* region at the aeronomic reactions and at the outer corpuscular interaction as well, and it is an important indicator for the processes in this region.

2. Part of the green oxygen 5577 Å line is also emitted at analogous processes with a line 6300Å in the *F* region (about 20 per cent), but an essential part of it comes from the *F* region, appearing in this way as an indicator of the dynamic phenomena in the *F* region. The excitation of the first negative system of N_2^+, as shown in [6], is also connected with the precipitation of corpuscules which ionize N_2 and at the same time provoke the excitation of the first negative system of N_2^+. In this manner we have two lines which are excited in aeronomic processes and by the precipitating corpuscules, and also one emission excited only by precipitating corpuscules (4278Å). Naturally, this provides for a very good separation of the aeronomic processes from those connected with corpuscular bombardment, while on the other hand the comparison between the red and green lines makes it possible to distinguish the pure aeronomic reactions from those provoked by dynamic processes.

The basic demands involved in the construction of the equipment are as follows:

A) To provide a possibility of measuring under a clear sky, with good spectral resolution, the emissions of 6300Å, 5577Å and 4278Å.

B) The threshold sensitivity for each one of the emissions should be of the order of 5 Rayleighs.

C) The measuring range should be from 5 to 1000 R.

D) The equipment should be capable of operating at temperature differences of 0° to 45°C and at humidity of up to 90 per cent.

E) It should consist of separate compact blocks which are easy to transport and install.

F) The electron block should be designed as a separate unit with its independent power supply, for which the possible variations in the supply voltage must also be taken into account.

G) The visual angle should be in the range of 3 to 6 degrees (the measurements are determined by the heterogeneous structure of the glowing region).

H) The equipment should not be sensitive to blows and vibrations.

3. Block Diagram and Description of the Equipment

Fig. 1 shows the individual blocks of the equipment. The basic block is an electrophotometer, designed on the basis of a colorimeter (Fig. 2). Its function is to receive the light flux and to make the corresponding selection of each one of the measured lines. The high voltage of the photomultiplier (PEM) is obtained by the block HUS and the processing of the signal received is performed by a direct-current amplifier, after which it is registrated by a recorder. More details about the electronic part of the equipment are given in part 3.2 of the Description.

3.1. Electrophotometer

Fig. 2 shows the block diagram of the electrophotometer, and Fig. 3 presents its principal groups. The basic tube of the equipment (18) is a double-one ensuring the regular thermal regime of the filters and photomultiplier. The disk with the filters has eight positions (Fig. 4). The first six of them are engaged with the interferential filters, the seventh one is intended for measurement of the dark current (here the light flux from the objective is cut out), and in the eighth position (^{14}C) the radioactive source — R_s is placed, by which a dynamic control of the sensitivity of the

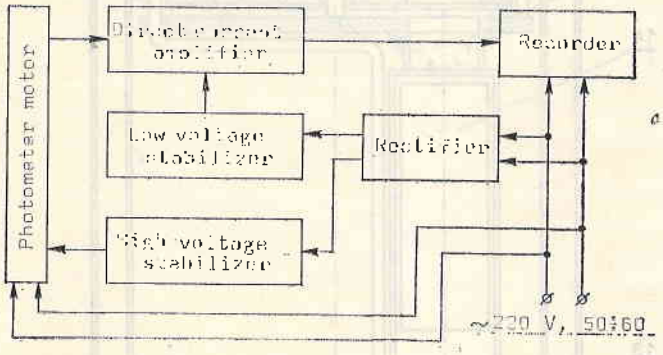

Fig. 1

equipment is achieved. The intensity of each emission is measured by two filters. The first one is centered on the measured line and the second one is used to measure the spectral background. Each filter is fitted separately in the disk, and after that it is corrected by the optic system of the device

in order to take the exact position at which the investigated spectral line is allowed to pass. Table 1 presents the filters used in the equipment and their principal parameters.

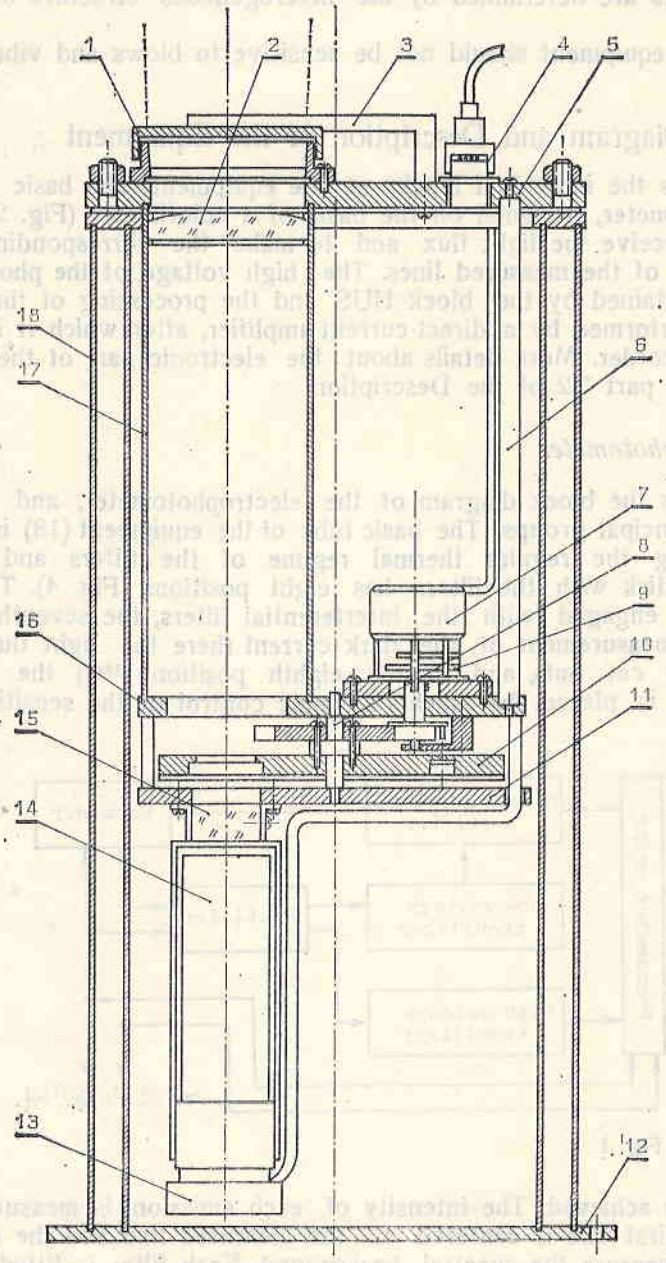

Fig. 2

A photomultiplier FEU-79 is put in a special tube (14), filled with any substance ensuring very efficient magnetic screening. This photomultiplier is one which has the best characteristics out of ten similar photomultipliers. The voltage divider (13), filled with high-quality ohmic resistors, is applied directly to the legs of the photomultiplier.

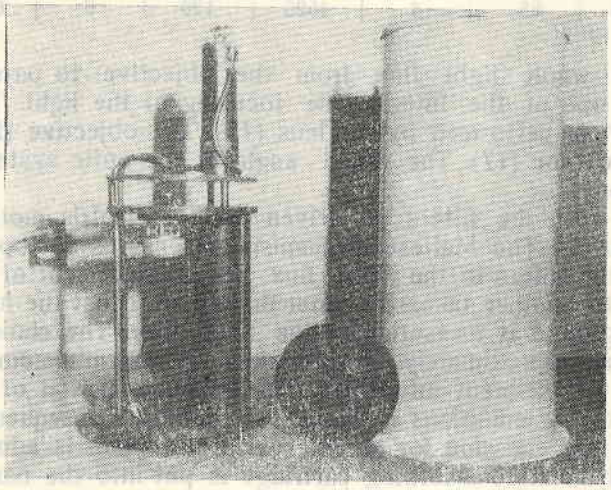

Fig. 3

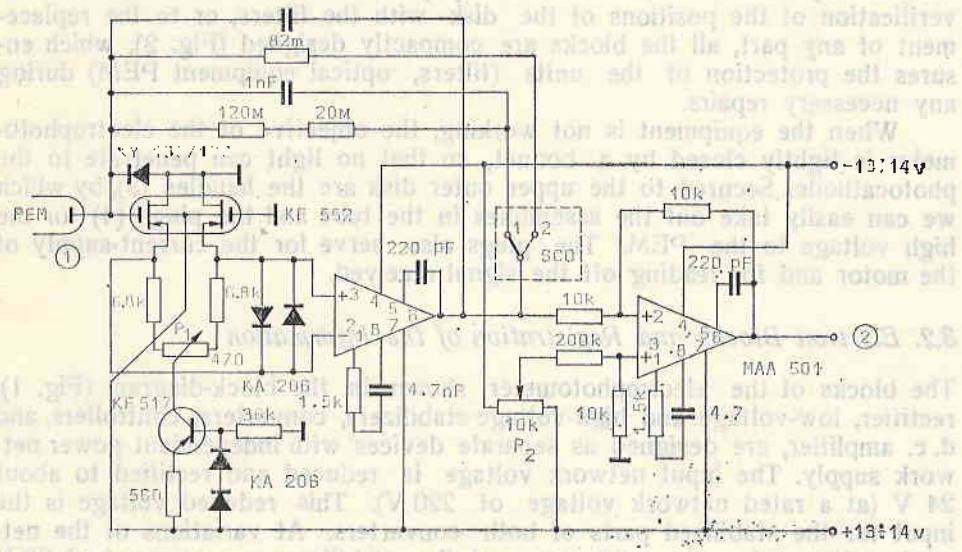

Fig. 4

The optic system of the electrophotometer consists of a single-lens objective (2), 80 mm in diameter, focal distance 300 mm. The disk with the filters (10) is placed in the focal plane of the objective. This makes it pos-

Table 1

No.	Line Å	Δλ Å	No.	Line Å	Δλ Å	No.	Line Å	Δλ Å
1	5577	80	3	4270	110	5	6300	65
2	5495	85	4	4525	120	6	6220	80

sible for the whole light flux from the objective to pass successively through each one of the filters. The focusing of the light flux on the cathode of PEM is performed by the lens (15). The objective (2) is placed in a special optic tube (17). The visual angle of the optic system is 5°, satisfying condition *G*.

The disk with the filters is driven by the electric motor (7) and the reduction gear (9). The Maltese mechanism (8) ensures a stop of 50 s for each one of the filters in the light flux. The displacement of the disk from one position to another takes 5 s. Immediately after that the intensity of the spectral background is measured by the next filter. The choice of the two-minute interval, approximately, is determined by the minimum period of the variations of the different intensities. The minimum period of the variations of each one of the emissions is about 10 minutes. Consequently, averaging the values of the emission for an interval of 1—2 min is admissible.

A special moisture-absorbing cartridge is put into the basic tube of the equipment filled with silica gel, and it can be changed easily and quickly without any need to dismantle the equipment. With a view to eventual verification of the positions of the disk with the filters, or to the replacement of any part, all the blocks are compactly designed (Fig. 2), which ensures the protection of the units (filters, optical equipment PEM) during any necessary repairs.

When the equipment is not working, the objective of the electrophotometer is tightly closed by a bonnet, so that no light can penetrate to the photocathode. Secured to the upper outer disk are the handles (3), by which we can easily take out the assemblies in the tube and the plugs (4) for the high voltage to the PEM. The plugs also serve for the current-supply of the motor and for leading off the signal received.

3.2. Electron Blocks and Registration of the Information

The blocks of the electrophotometer shown in the block-diagram (Fig. 1), rectifier, low-voltage and high-voltage stabilizers, converters, controllers, and d. c. amplifier, are designed as separate devices with independant power network supply. The input network voltage is reduced and rectified to about 24 V (at a rated network voltage of 220 V). This reduced voltage is the input for the stabilized parts of both converters. At variations of the network voltage of up to ± 20 per cent the stabilizers ensure constant 20 V at the output, with coefficient of stabilization of about 4000. A separate low voltage (for the d. c. amplifier) and a high voltage (for the photomultiplier) are provided on account of the necessity for the high stabilized rated voltage of 1750 V to be regulated within $\pm$ 100 V. In this way, for each photomultiplier from the series FEU-79 we can choose the most suit-

able high-voltage supply, thereby ensuring maximum sensitivity of the FEU-79. The characteristics of the high-voltage stabilizer, of the converter and of the rectifier are given in [10].

The diagram of the low-voltage stabilizer, converter and rectifier does not differ from the one described in [11]. It provides a supply of ± 13 V for the d. c. amplifier. The d. c. amplifier, whose diagram is shown in Fig. 4, is used to amplify the current from the anode of the photomultiplier and to transform it into voltage for the recording voltmeter. The maximum variations of the intensity of the signal lead to a maximum output signal of about ± 12 V. The determination of the zero output level in the absence of any signal is performed by a potentiometer of 10 K, connected to the not inverted input of the second operational amplifier. The sensitivity of the whole amplifying feedback can be altered to about 30 per cent from the rated one by switching the key shown in Fig. 4 from position 1 to position 2.

In general, the diagram in Fig. 4 differs from the one described in [11] by the presence of a diode KY 130 at the input of the field-effect transistor KF 552. This diode has the following function: at a normal signal from the photomultiplier the voltage at the gate of KF 552 is still positive with respect to the zero bar. The diode is switched to a non-passing direction and its inner resistance is of the order of giGaohm, so that it does not influence the coming signal. At a strong lighting of the photocathode of FEU-79 the diode KY 130 is released and preserves the input cascade of the amplifier.

A recording voltmeter of the H 340 type is used for registration of the signal received. As far as it is necessary for the adjustment of its measurement range in the limits of the output voltage from the direct current amplifier (the maximum deviation of H 340 is $+12$ V), additional thermostable resistor is put in the electrical diagram of H 340. The registration of the information is performed continuously during the observation.

Having processed in this way the data obtained during one night and having entered it in Table 2, we can obtain the relative intensity of every line as a function of time. The relative intensity is determined by formula (1):

$$I_{rel} = \frac{N_{emiss.} - K_i N_{backgr.}}{N_{rs}}. \tag{1}$$

The value of K_i for every line showing the ratio of the transmitting capacities of each one of the two filters are given by

$$A = \int_{\lambda_1}^{\lambda_2} r_i \, d\lambda \tag{2}$$

$$K_i = \frac{A_{emiss.}}{A_{backgr.}}. \tag{3}$$

The coefficients K_i are determined experimentally in the following way. We admit a constant signal through both filters (for example, reflected and

diminished solar radiation), and the ratio between the indications of the two filters gives the value of K_i in formula (1).

The dynamic control of the sensitivity of the equipment is achieved by a standard radioactive source (^{14}C), selected in such a manner that its value

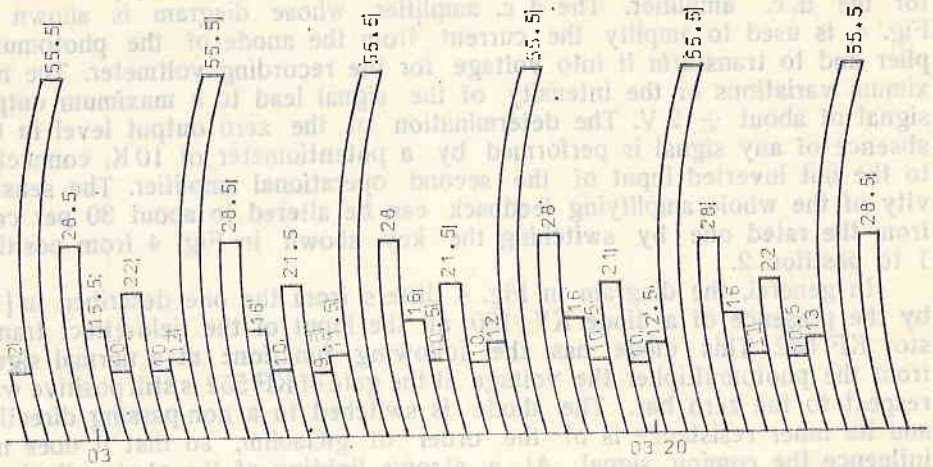

Fig. 5

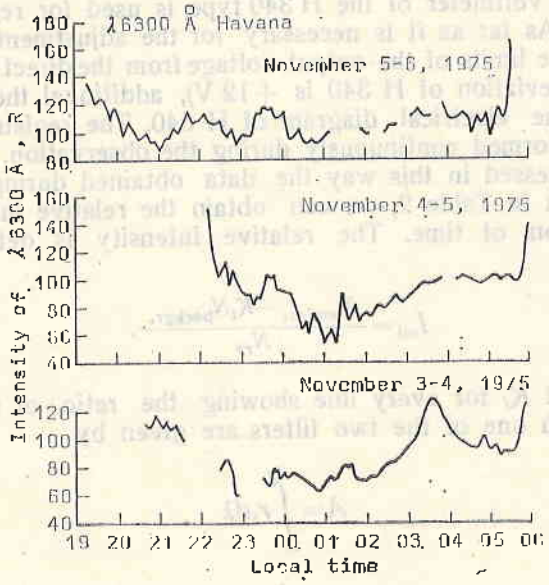

Fig. 6

shall be in the middle of the scale of the recorder. The eventual changes in the sensitivity during operation are corrected by the R_s coefficient in formula (1).

4. Measurements of Optical Emissions by the Equipment

The light flux coming from the objective passes through each one of the filters and reaches the cathode of PEM. The photo-current is transmitted to the amplifier and is registered by the recorder H 340. Fig. 5 shows part of the registration of the atmospheric emission. Each one of the lines measured is designated. The registration was carried out on October 16/17, 1975, in the Observatory at Stara Zagora.

The value of a given line, registered on the band, is measured above the level of the dark current (Fig. 5). The values for the intensity of the line 5577 A can be estimated from the data given in Fig. 1.

5. Absolute Calibration of the Equipment

The transformation of the relative values of the emissions to the absolute values is a very difficult proposition in view of the fact that the equipment operates almost at its threshold sensitivity, where the fluctuations of the background exercise an essential influence. The methods given in [1, 7, 8, 9] are used in the absolute calibration of the equipment.

In addition to the absolute calibration we also carried out simultaneous observations of the same emission by another electrophotometer which had been used for such purposes over a long period of time. In this way we obtained a correct calibration of the equipment.

Fig. 6 shows an example taken from our first observation near Havana in Cuba.

Acknowledgements. We wish to express our sincere gratitude to Professor K. Serafimov for his great interest and valuable help in the course of this work.

References

1. Гогошев, М. М. Кандидатска дисертация. С., БАН, 1973.
2. Gogoshev, M. Planetary and Space Sciences, 23, 1975, 305.
3. Trutce, I. L. Planetary and Space Sciences, 16, 1968, 1, 140.
4. Chamberlain, J. Physics of the Aurora and Airglow. New York—London, 1961.
5. Фишкова, Л., Г. Маркова. Астрон. циркуляр, АН СССР, 1958, 196.
6. Dalgarno, A. Ann. Geophys., 20, 1964, 1.
7. Гогошев, М. М., Т. Райчев. Известия на Секция астрономия. С., БАН, V, VI, 1973.
8. Мартинов, Д. Курс практической астрофизики. М., 1967.
9. Fishkova, L., G. Markova, Bull. Abast. Astrophys. Observ. No 24, 1939.
10. Chapkunov, S. Compt. rend. Acad. Bulg. Sci., V, 28, 1975.
11. Chapkunov, S., M. Petrounova. Compt. rend. Acad. Bulg. Sci., V, 29, 1976.

Наземная электрофотометрическая станция для исследования оптических эмиссий высокой атмосферы

М. М. Гогошев, С. К. Чапкынов

(Резюме)

Рассмотрены некоторые механизмы генерации оптических эмиссий высокой атмосферы и данны их интенсивности. Описана блок-схема, которая включает в себя электрофотометр, электронный блок и регистратор информации. Методика измерения, калибровки и получения данных подробно дискутируется в работе.

BULGARIAN ACADEMY OF SCIENCES

SPACE RESEARCH IN BULGARIA, 1

Sofia · 1978

Using Airglow Emissions for the Diagnostics of Some Magnetospheric-Ionospheric Influences

1. The Oxyen Emission λ 6300 $\AA$

M. M. Gogoshev

1. Introduction

It has recently been established that the ionosphere is only part of a significantly larger plasma envelope around the Earth, which is called plasmasphere. More accurately, the ionosphere is the nearest to the earth-crust layer, where the absolute concentration of neutrals, electrons and ions is considerably higher than in the other regions. Considering the ionosphere in this way as part of the magnetosphere, we come to a new stage in the ionospheric investigations, i. e. to investigations of the dynamic couplings between the magnetosphere and the ionosphere. Now it is necessary to revise our previous concepts, and first of all that on the conditions of the disturbed ionosphere which is to be seen in connection with magnetospheric-ionospheric interactions. For example, we could show the ionospheric storms which were studied before by statistical methods mainly, in the mid- and low ionosphere. It has been realized in the past few years that a geomagnetic storm consists of separate elementary storms or substorms, and now it is possible to investigate and explain the physical nature of the ionospheric disturbances. The precipitation of corpuscules in the ionosphere was considered as a direct consequence of the solar flares, and not as a purely magnetospheric process caused by the flare.

Different methods are used in the diagnostics of the magnetospheric-ionospheric interactions, by which the conditions of the ionosphere and the magnetosphere are studied separately while at the same time we are looking for the relations between them. In general, we could classify these methods in two main groups. To the first group, that of ground methods, belong all classical investigations of the ionosphere and magnetosphere used during the last few decades. In the second group of methods, which may be called space methods, the investigations are carried out directly in space by equipment on rockets and artificial satellites. Direct measurements are

thus taken of the structural parameters of the plasma concentrations of electrons, ions and neutrals, in addition to temperature measurements. Here belong also the measurements of the various dynamic characteristics such as drift, wind, diffusion, etc. Electric and magnetic fields in the plasma, as well as various other processes are also measured by space methods.

It should be pointed out, however, that the classification of these methods in two groups is a very conventional one. An essential part of the structural and dynamic parameters of the ionosphere and magnetosphere can be obtained independently by any one of the two methods. A typical example is the measurement of the electron density by ground methods and by various rocket and satellite methods.

We know that the investigation of the neutral optical emissions of the near-space plasma provides a vast amount of information about the complicated physicochemical processes which take place in this medium. In the auroral zone in particular, the investigation of the atmospheric emissions is the basic source of information for studying the interaction between the corpuscules and the ionospheric plasma.

The purpose of this paper is to show the opportunities offered by the investigation of the atmospheric emissions for discovering the magnetosphe-

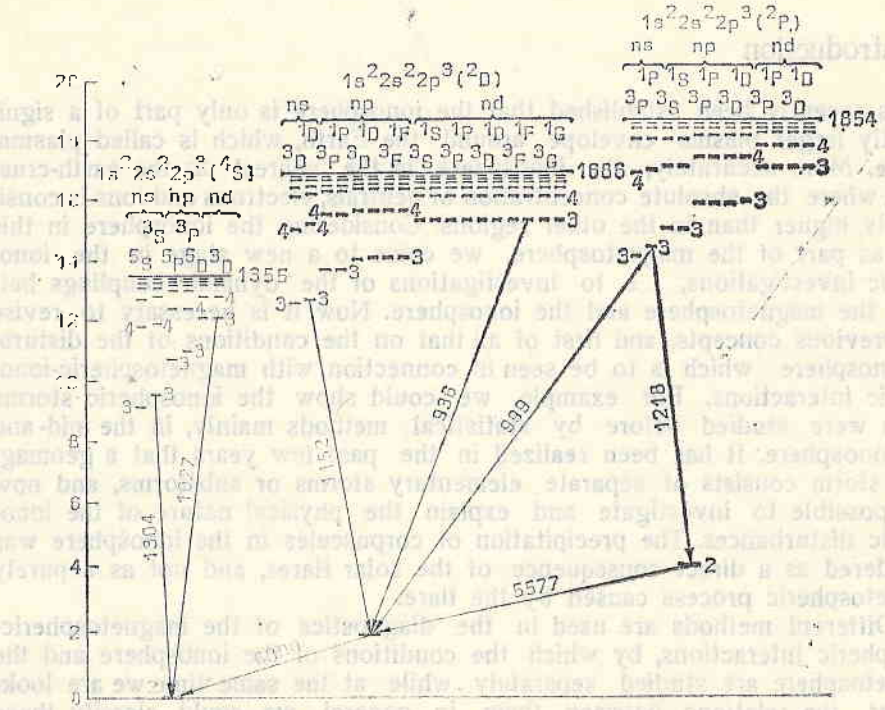

Fig. 1. Energetic terms of the oxygen atoms

ric-ionospheric relations, mainly as regards the subauroral regions — mid- and low latitudes. The aurorae will be discussed to the extent to which they are connected with the optical emissions over mid- and low latitudes.

2. Excitation of the Oxygen Emissions

As is well known, in the intermediate $E-F$ and F regions, i. e. that part of the ionosphere which is in direct contact with the magnetosphere, the oxygen atoms are the basic components of the plasma. For that reason, let us consider the ways of excitation of the oxygen atoms. Fig. 1 presents the diagram of the basic energetic terms of the oxygen. It shows that the nearest to the basic term (^3P) and, consequently, most easily excited terms are ^1D (energy of excitation 4.17 eV). The restoration of the atom from an excited state to the normal is achieved by the transition $^3P—^1D$, at which the red oxygen triplet λ 6300 Å, λ 6364 Å and λ 6391 Å is emitted, and the transition $^1D—^1S$ leads to the emission of the so-called auroral line with a length of 5577 Å.

2.1. The red oxygen line λ 6300 Å

The first line of the triplet with a length of 6300 Å is significantly more intensive compared with the second and third lines, and it is the one usually quoted. This line, called nebular line because of its large propagation in the nebulas, holds an important place among all airglow emissions. (Later on we shall explain its popularity.) The basic mechanisms leading to excitation of the term ^1D and, consequently, to emission of λ 6300 Å have been thoroughly treated in [1—6]. These mechanisms are the following:

2.1.1. By chemical reactions

The two basic reactions playing an essential role in this process are the dissociative recombinations of O_2^+ and NO^+:

$$(1)\qquad O_2^+ + e \longrightarrow \begin{cases} O(^1D) + O(^3P) \\ O(^1S) + O(^3P) \\ O(^1D) + O(^1D) \\ O(^1D) + O(^1S) \end{cases} \qquad \alpha_D(O_2^+)$$

$$(2)\qquad NO^+ + e \longrightarrow \begin{cases} O(^1D) + N(^4S) \\ O(^3P) + N(^2D) \\ O(^3P) + N(^4S) \end{cases} \qquad \alpha_D(NO^+)$$

The above reactions reveal that the dissociative recombination of O_2^+ is considerably more productive than that of NO^+. It has been theoretically and experimentally established that at each act of recombination of O_2^+ at least one of the oxygen atoms has a term ^1D, while the efficiency of reaction (2) is by one order lower, i. e. at ten recombinations of NO^+ at least one oxygen atom has a term ^1D.

The dissociative recombinations (1) and (2) have a very high rate. The rate constant of the first reaction $\alpha_D(O_2^+)$ is equal to 2×10^{-7} cm^3 s^{-1}, that of second reaction being 4×10^{-7} cm^3 s^{-1} [7]. Naturally, at such high rates

of dissociation of O_2^+ and NO^+ the reserves should be depleted, but this does not actually happen. This situation explains the great importance of the ion-exchange reactions in the physics of E and F ionospheric regions, by which the stocks of molecular ions are continuously replenished.

$O(^1D)$ can be obtained also at triple collision, i. e. at a reaction of the following type:

$$O(^3P)+O(^3P)+O(^3P) \longrightarrow O(^1D)+O_2, \tag{3}$$

but the above reaction is not very probable in reality because of the need of very high absolute densities of O in the $E-F$ and F regions which actually do not exist.

The reaction

$$N(^2D)+O(^3P) \longrightarrow N(^4S)+O(^1D) \tag{4}$$

plays an essential role in the deactivation of the excited nitrogen whose life-time, before emitting, is about 26 hours. On the other hand, the quantity of $N(^2D)$ is small, and this leads to insignificant production of $O(^1D)$ by this reaction.

The same refers to the reaction:

$$O^+(^2D)+O(^3P) \longrightarrow O^+(^4S)+O(^1D), \tag{5}$$

which is very effective at high altitudes.

2.1.2. Dissociation of O_2 according to the reaction:

$$O_2(X^3\Sigma_g^-)+h\nu \longrightarrow O(^3P)+O(^1D). \tag{6}$$

The solar ultraviolet quantum taking place in this reaction is from the Schumann-Runge's continuum. Naturally, this reaction is valid only when the upper atmosphere is lightened directly by the Sun.

2.1.3. Direct electron collision

$$O(^3P)+e \longrightarrow O(^1D)+e. \tag{7}$$

An essential part of the red line emission is emitted by the above mechanism, mainly during the day. This mechanism plays a definite role in some extreme cases during the night pre-dawn enhancement, SAR arcs, etc.

Let us see which electrons could take part in reaction (7) for the excitation of the term ^1D. No doubt, these electrons should have energy $E>2$ eV. In Fig. 2 the number of the atoms $O(^1D)$ are taken from [26], which number could be produced by one electron with energy E, at different values of the parameters of the fractional ionization $R=N_e/[0]$.

Let us now see where in the ionosphere could there appear electrons with energy in the range of $2\div 100$ eV.

a) Photoelectrons. The observations show that the essential part of the day emission of λ 6300 Å is due to excitation by ambient photoelectrons, produced in consequence of the absorption of the short-wave solar radiation. At certain particular conditions the photoelectrons play a role during the night as well. For example, at mid-geomagnetic latitudes in winter, the

intensity of the red line in the north hemisphere shows a sharp increase before the local dawn. This phenomenon, observed for the first time by Barbier in 1959 [3], was interpreted by Cole [8] as an effect of the photoelectrons arriving from the magneto-conjugate regions (MCR), where the Sun has already lightened the local ionosphere.

b) Superthermal electrons. The energy of these electrons is more than 2 eV. At daylight conditions, the high-energy end of the Maxwell distribution of the electrons is passing to and melting with the spectrum of the photoelectrons. During the night an insignificant part of the ambient electrons possess energy of over 2 eV. No doubt, this small part and the curve of the Maxwell distribution depends on the electron temperature T_e. The higher the T_e, the higher the contribution of the local thermal electrons to the excitation of λ 6300 Å. Let us note here that it is precisely by the superthermal electrons that some magnetospheric influences on the ionosphere are achieved, as can be detected by the red line. The heating of the ambient electron gas can be achieved by Cole thermal conductivity along the field lines, by dissipation of the energy in the *F*-region of iono-cyclotron waves generated in the magnetosphere, and by some other ways.

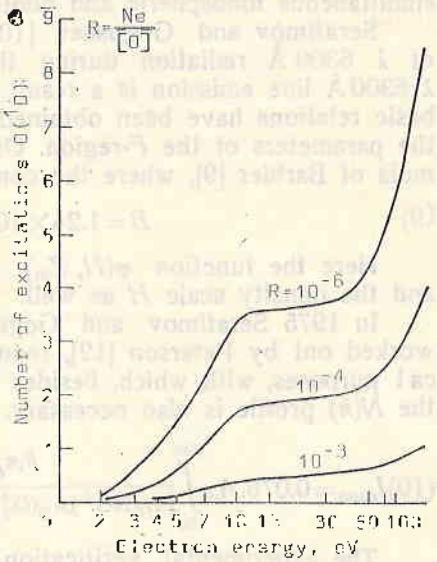

Fig. 2. Excitation of O(^1D) by electrons

c) Secondary electrons obtained at the precipitation of electron and proton fluxes.

It is well known that the precipitating electron and proton fluxes from the magnetosphere provoke ionization of the atmospheric components. The secondary electrons obtained in this way take part in the elastic and non-elastic collisions, causing the rise of the neutral and ion temperature, and to a higher degree, that of T_e. At the non-elastic collisions, the vibrational terms of N_2 and O_2 are excited with higher efficiency, also that of ^1S and especially ^1D, for which a very small quantity of energy is necessary. In actual fact, at the aurora the excitation of the oxygen emissions is performed mainly by secondary electrons.

2.2. The red emission at calm conditions

The main generative mechanism of the λ 6300 Å line during the night is the dissociative recombination of O_2^+, according to reaction (1). Barbier and Glaume [9] obtained a semi-empirical relation between the intensity of the 6300 Å line and the ionospheric parameters at calm conditions, which is presented by the following formula:

(8) $$I_{6300}=B(f_0F)^2\exp.\left[-\left(\frac{h'F-200}{H}\right)\right],$$

where f_0F is the critical frequency of the layer F, $h'F$ is the height of the layer, H is the density scale, while B and C are constants determined at simultaneous ionospheric and photometric observations.

Serafimov and Gogoshev [10] presented in 1972 a generalized theory of λ 6300 Å radiation during the night. According to this theory, the λ 6300 Å line emission is a result of the dissociative recombination. Some basic relations have been obtained between the emission of this line and the parameters of the F-region. One of the relations is reduced to the formula of Barbier [9], where the constant B already has a physical meaning;

(9) $$B=1.24\times10^4\,.\,k_1[O_2]_{300}\varphi(H, Z_m).$$

Here the function $\varphi(H, Z_m)$ comprises the half-width of the layer Z_m and the density scale H as well.

In 1975 Serafimov and Gogoshev [11] improved the similar formula worked out by Peterson [12], reducing it to a convenient form for practical purposes, with which, besides the atmospheric model, the knowledge on the $N(h)$ profile is also necessary. This formula is:

(10) $$I_{6300}=0.076.A.\varepsilon\int_{150}^{500}\frac{k_1\alpha_D(NO^+)\,.\,\alpha_D(O_2^+)\,.\,[O_2]N_e^2\,dh}{\{\alpha_D(NO^+).\alpha_D(O_2^+).N_e+\alpha_D(O_2^+).k_3[N_2]+\alpha_D(NO^+).k_1[O_2]\}(A+K[N_2])}$$

The experimental verification of formula (10), carried out by simultaneous ionospheric and photometric observations, has shown that it provides values about the intensity of the red line emission which are the nearest to those registered experimentally. By tracing the evolution of the connections between the red oxygen line and F-region parameters, our aim was to show that by the photometric observations of the λ 6300 Å emission during the night we can very well control the basic processes in the F-region. The accuracy of the photometric data exceeds that of the radiophysical measurements. For example, a change of 5—6 per cent, and even less, of the electron concentration in the F-region cannot be detected by vertical sounding, while changes of only 2 per cent in N_e can be detected by photometric measurements of the λ 6300 Å line.

2.3. The red oxygen emission at geomagnetic activity

2.3.1. Strong storms in the aurora zone

Observations of the red line emission, carried out over a period of many years at the Observatory of Stara Zagora, Bulgaria [4], at the Observatory of Abastumani, USSR [13] and at the Observatory of Zvenigorod, USSR [14] have shown that the mean night intensity of the red line emission, with the exception of the twilight periods, is within the limits of 20—100 R, under conditions of low geomagnetic activity ($K_p<2$). The increase in geomagnetic activity leads immediately to a sharp rise in the λ 6300 Å emission intensity. Trutce [15] obtained a relation between D_{st} variations of the geomagnetic field and the abnormal rise in the red line intensity. This relation is the following:

(11) $$\log I_{6300} = \beta D_{st} + 2 \times 10^{-2} F - 3.17,$$

where F is the flux of the solar radio-radiation with a length of 10.7 cm (10^{-22} W/m^{2}Hz), and β is a constant depending on the geomagnetic latitude. This relation makes it possible to estimate the total planetary flux of energy in the ionosphere by the intensity of the λ 6300 Å line, depending on the strength of the geomagnetic storm. For example, during the strong geomagnetic storm on 11 February 1958, at $D_{st} = 409\,\lambda$, the energy of the red line was about 300 erg/cm^2 s.

Let us note here that the above relation is valid for geomagnetic storms at which $D_{st} > 100\,\gamma$ and at geomagnetic latitudes of more than 40°. This important formula no doubt reflects a definite generative mechanism which is valid only for subauroral zones and also for a definite region of the magnetosphere. The action of this mechanism is insignificant during weaker geomagnetic storms ($D_{st} \leq 100\,\gamma$) and the observed increase in the intensity of the red line must be explained in another manner. The most probable cause for excitation of the 6300 Å line, at strong geomagnetic storms, is the heating of the F-region and the rise of T_e. In this case, as we have shown above, there is an increase in the quantity of the superthermal electrons exciting the 6300 Å line. We shall have, of course, electrons with energy over 4.16 eV which could excite the green oxygen line as well, but they would be few and, contrary to the assertion of Krassovsky [16], the green oxygen line should have a very low intensity. Our calculations show that the intensity of the red line, obtained by the thermal mechanism, should be by four orders higher than that of the green line. The same ratio has actually been observed during the geomagnetic storm on February 11, 1958, and this confirms the existence of the thermal mechanism. We must add, however, that the cause of the heating of the electron gas in this case remains unknown.

2.3.2. SAR-arcs

A full review of the observations of SAR-arcs and their generative mechanisms is given in [17]. In general, these arcs are observed over mid-latitudes (Fig. 3) at a height of about 400 km. Their length is several thousand kilometres and their width is several hundred kilometres. They have an intensity of between 100 and 1000 Rayleighs. The most important fact is that the red arcs are observed in that region of the atmosphere where the plasmapause is projected. We assume that the basic generative mechanism is related to the appearance of the ion-cyclotron waves in the zone where the asymmetric ring current is spread out in the plasmapause region. The dissipation of the energy of these waves in the F region leads to heating of the electron gas and to the corresponding glowing of the atmosphere by the red emission. The exact determination of the height (by vertical sounding) can provide very good information about the nature of these electro-magnetic waves, taking into consideration the fact that they transmit their energy to the electron gas depending on the free path of the electron.

2.3.3. Increase of the red line emission over mid- and low latitudes

The absence of a sufficient number of stations in the equatorial zone and in the low latitudes makes it impossible for us to assess exactly the behaviour of the 6300 Å emission during the geomagnetic disturbance. In general, the satellite observations have shown that at about 10—15°, on both sides of the magnetic equator, there exist regions (arcs) with elevated intensity of the red oxygen line. (These are the familiar regions of higher electron concentration related to what is known as the equatorial anomaly.) It is difficult to maintain that they are connected with the magnetospheric processes and with the ring current, and that they depend on the geomagnetic activity.

In 1973, through the observations carried out at the Bulgarian station of Stara Zagora, quasiperiodical oscillations of the intensity of the λ6300 Å line were discovered with an average period of 90 minutes during the main phase of a geomagnetic storm (Fig. 4) [18, 19]. Later on Vlassov and Romanovsky [20] pointed out that the observations at the Observatory of Stara Zagora were the first confirmation of the existence of the theoretically predicted oscillations with such period, which, in their opinion, are due

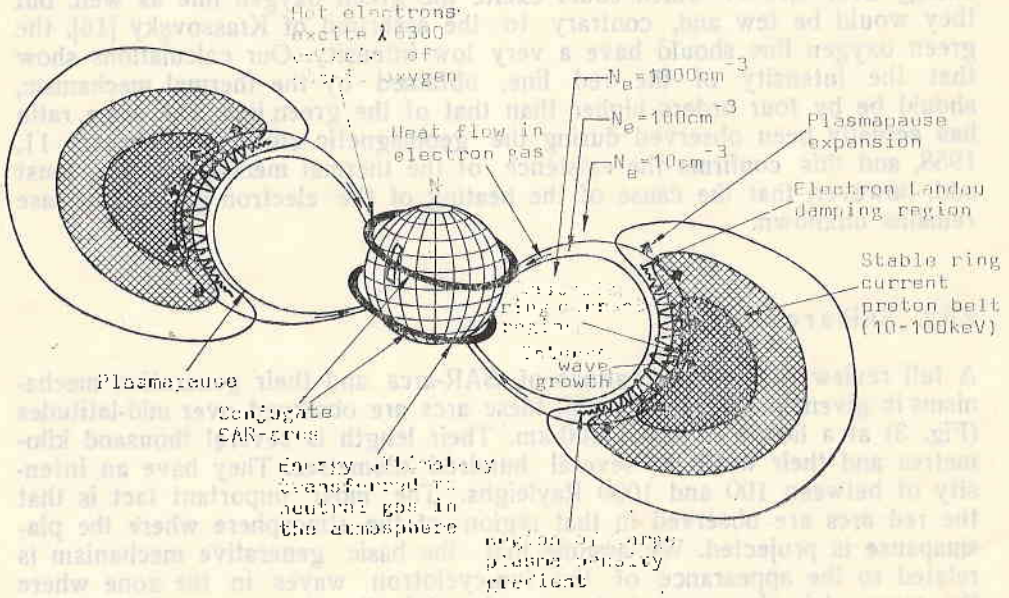

Fig. 3. Schematic diagram of the magnetosphere and the regions in which the SAR-arcs are excited

to changes in ion concentrations in the F region during the geomagnetic storm. Comparing the above observations of the atmospheric emissions with those of the geomagnetic field (at the station in the oval — Leirvogur and at the station of Panagyurishte), and also with the data from the ionosphe-

ric station of Sofia, Gogoshev, Serafimov, Gogosheva and Kazakov [21, 22] have shown that:

a) The time and the periods of the wave oscillations of the glowing are connected with the substorms in the polar region.

b) The height of the F-layer has pulsated synchronously with the substorms.

c) As a consequence of that, the dissociative recombination, by which the observed oscillations could be explained quantatively, has been changed.

d) The assumption that electric fields with intensity of 5—10 mV/m are generated during the substorm in the mid-latitudes, tallies very well with the experimental data.

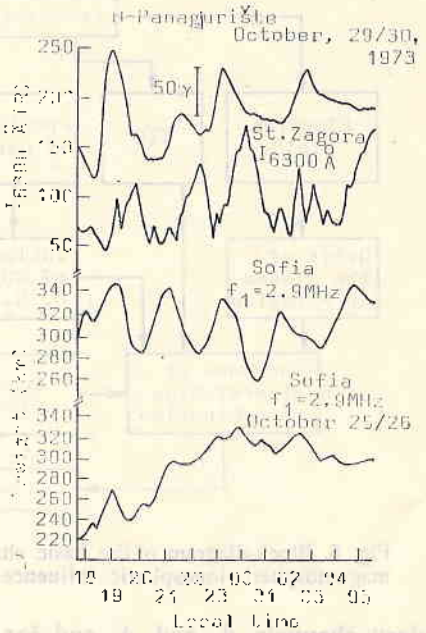

Fig. 4. An example for substorms in the mid-latitude ionosphere

Another example of emission, increase over the mid-latitudes is the case which occurred on September 18/19, 1974. After a comparatively strong geomagnetic storm during the period of 14—17 September, a normalization of the geomagnetic field was observed. During the even ing hours on September 18/19, however, there was a single and isolated sub-storm. About one and a half hours after that the Observatory at Stara Zagora registrated a sharp increase of the intensity of the λ 6300 Å line reaching 600 R. At the same time, the ionograms at the station in Sofia showed the presence of ionospheric heterogeneity, which strongly intensified the dissociative recombination and hence the glowing of the red line [23]. It is assumed that the generator of these moving heterogeneities is located in the polar region, perhaps it coincides with the auroral oval and increases during geomagnetic activity [24].

3. Conclusion

The influences of the magnetosphere on the mid- and low latitude ionosphere which culminate in a rise of the red oxygen line intensity as a final result, are presented in Fig. 5. It shows that the increase in the λ 6300 Å line can be achieved through four channels which we denote by the letters A, B, C, D. Naturally, with one single observation only of the λ 6300 Å line it is impossible to solve this system of equations with four unknown quantities. Therefore, other observations are to be carried out, parallel with the observations of the red line. First, we must carry out ionospheric observations of the F region, by which several structural parameters can be measured, such as N_e, for example. Through N_e we could immediately control the most important channel A (dissociative recombination). Let us assume

that the influx of λ 6300 Å emission is passing through the channel A. This channel consists of four secondary channels (A_1, A_2, A_3, A_4). The measured ionospheric data are quite enough for comparison and control of the secon-

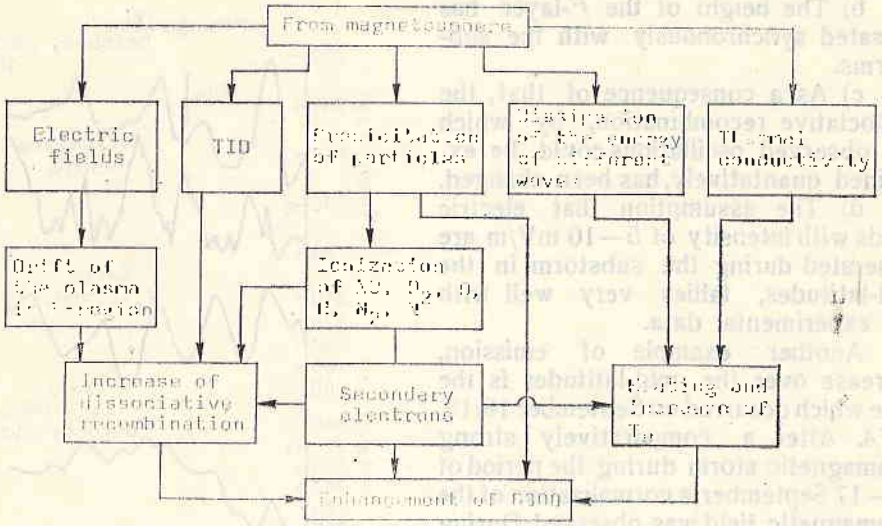

Fig. 5. Block-diagram of the basic channels for excitation of the λ 6300 Å line under magnetospheric-ionospheric influence

dary channels A_1 and A_2 and for their sufficient discrimination at the same time. If channels A_1 and A_2 are not operating we must check the connections A_3, A_4 and B, C, D as well. No doubt, there exists a definite connection between channels B, C, A_3 and A_4 which is unknown. We only know that the channels B, C, A_1 and A_2 are operating simultaneously. By way of a qualitative explanation, we could only say that A_1, A_2 and C, for mid-latitudes, are much weaker than B.

The channel C can be controlled in the following way: It is well known that the precipitation of corpuscules leads to ionization of N_2 and, at the same time, to the excitation of the first negative system of N_2^+. By observations of the lines λ 3914 Å or λ 4278 Å we can provide a qualitative estimation of the flux of particles and, consequently, of the influx into the channels B, A_3 and A_3. Additional information for channel B can be obtained by parallel observations of some bands of N_2 and O_2, which are excited only by secondary electrons. Consequently, the unknown channel is only D, which can be determined by observations as the difference between the observed values of λ 6300 Å emission and the estimated influx of A, B and C. This difference can immediately give us information about the electron temperature T_e, by using the graph in Fig. 6 [25].

In addition to the analysis given in section 3, the use of a photometric station can be recommended for the ground diagnostics of the magnetospheric-ionospheric influences by the atmospheric emissions, in which station the atmospheric emissions λ 6300 Å, λ 3914 A and one of the bands of N_2

or O_2 are measured. In addition, the use of an ionospheric station also is recommended, as it can give the basic structural parameters of the F region, with the same time resolution.

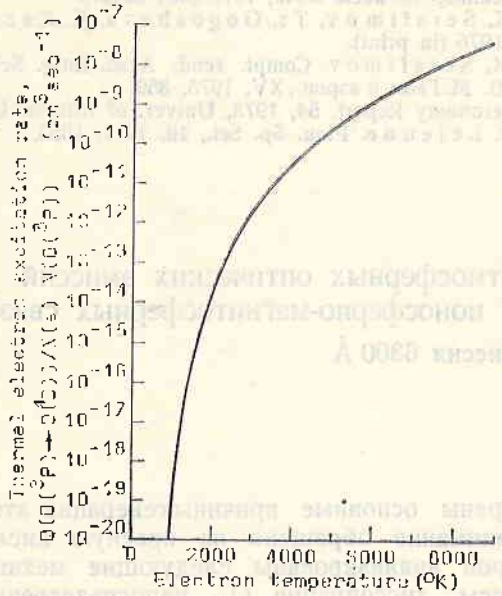

Fig. 6. Excitation of the red oxygen emission depending on the electron temperature

Acknowledgements. The author is very grateful to Professor K. Serafimov for his interest and valuable comments on this paper, and to K. Kazakov and Ts. Gogosheva for helpful discussions in the course of this work.

References

1. Бейтс, Д. Р. Физика верхней атмосферы. Под ред. на Дж. Ратклиф. М., 1963.
2. Чембърлейн Дж. Физика полярных сияний и излучение атмосферы. М., 1963.
3. Barbier, D. In Geophysique extérieure, New York — London, 1963, 182.
4. Гогошев, М. М. Кандид. дисерт., ЦЛКИ—БАН, 1973.
5. Серафимов, К., М. Гогошев. Теория на светенето на нощното небе при дисоциативна рекомбинация. Юбилеен научен сборник на Астрономическата обсерватория, Стара Загора, 1972.
6. Акасофу, С. И., С. Чапман. Солнечно-Земная физика, М., 1975.
7. Серафимов, К. Физика средней атмосферы. С., БАН. 1970.
8. Cole, K. D. Ann. Geophysique, 21, 1965, 156.
9. Barbier, D., J. Glaume. Planet. and Sp. Sci., 9, 1962, 133.
10. Serafimov, K., M. Gogoshev. Compt. rend. Acad. Bulg. Sci., 25, 1972, 197.
11. Serafimov, K., M. Gogoshev. An exact method for determination of the 6300 Å oxygen emission by the Use of $N(h)$ Profiles. Preprint presented at COSPAR, Varna, 1975.
12. Peterson, V. L., Ann. Geophys., 24, 1968, 101.
13. Fishkova, L. M., Yu. D. Mateshvili. Report of XV General Assembly of IUGG Moskow, 1971.
14. Трутце, Ю. Л. Доклад на XV Асамблея на ИАГА, М., 1971.
15. Трутце, Ю. Л. В: Полярные сияния и свечение ночного неба, М., 1973, 5.
16. Красовски, В. И. Штилы и штормы в верхней атмосфере. М., Наука, 1971.

17. Rees, M. N., R. G. Roble. Reviews of Geophys. and Space Physics, 13, 1975, 201.
18. Gogosheva, Ts., M. Gogoshev. Compt. rend. Acad. Bulg. Sci., 27, 1974, 1659.
19. Kazakov, K., M. Gogoshev. Compt. rend. Acad. Bulg. Sci., 28, 1975.
20. Vlasov, M. N., Yu. A. Romanovsky. Report at XVIII COSPAR, Varna, 1975.
21. Гогошева Цв., К. Серафимов, М. Гогошев. Сборник доклади на VII Ленинградски семинар по косм. лъчи, 1976 (под печат).
22. Gogoshev, M., K. Serafimov, Ts. Gogosheva, K. Kazakov. Planetary and Sp. Sci., 24, 1976 (in print).
23. Gogoshev M., K. Serafimov. Compt. rend. Acad. Bulg. Sci., 29, 1976 (in print).
24. Шамунькина, В. М. Геом. и аэрон., XV, 1975, 359.
25. Mantas, G. P. Aeronomy Report, 54, 1973, Univer. of Illinois, Urbana.
26. Dalgarno, A., G. Lejeune. Plan. Sp. Sci., 19, 1971, 1653.

Использование атмосферных оптических эмиссий для диагностики ионосферно-магнитосферных связей

1. Кислородная эмиссия 6300 Å

М. М. Гогошев

(Резюме)

В работе рассмотрены основные причины генерации атмосферных эмиссий. Особенное внимание обращено на красную кислородную линию 6300 Å, для которой анализированы следующие механизмы генерации: химические процессы, диссоциация O_2, непосредственные электронные удары и диссоциативная рекомбинация. В работе также рассмотрены причины излучения линии во время магнитосферных смущений и в авроральных красных дугах. Сделано предложение для диагностики ионосферно-магнитосферных связей посредством измерения атмосферных оптических эмиссий.

BULGARIAN ACADEMY OF SCIENCES

SPACE RESEARCH IN BULGARIA, 1

Sofia · 1978

On the Differential Rotation and the Figure of Celestial Bodies*

T. R. Tilchev

1. Introduction

The differential rotation of the celestial bodies is a topical problem. Attempts to explain this phenomenon have been made by Kalitzin [1], Clement [2], Rubashev [3], Menzel [4], Fessenkov and others. Lichkov [5] considers the rotation of the Earth's envelopes (nucleus, mantle, litosphere, hydrosphere and atmosphere) with different angular velocities. The differential rotation is clearly observed in the Sun, Jupiter, Saturn and in our Galaxy.

The purpose of this work is to provide a reasonable solution to this important problem, taking into consideration the fact that *gravitation* is the principal factor in this phenomenon.

2. Description of Model

We first consider the celestial body in its earliest stage of evolution, representing it by the following idealized model. We assume that the body consists of elementary layers with equal eccentricity. The body may be homogeneous or with increasing density toward the centre, according to any law. The viscosity is neglected: we assume that at the extremely high temperature of the young celestial body the viscosity is equal to zero. The figure of this ideally elastic body is determined by the action only of gravitation and of the centrifugal force, and it is assumed to be an oblate ellipsoid of rotation. Our model is very near to the structure of the stars from the early spectral classes and that of neutron stars, described by Shklovskiy [6], whose superfluid matter, deprived of viscosity, is of an ellipsoidal equilibrium configuration.

*For open discussion

3. Methods and Results

1. We use Newton's condition of equilibrium:

$$P - E_0 = F_0, \text{ [7]}$$

in its generalized form

(1) $$P - E_\varphi = F_\varphi \cos\varphi,$$

or

(2) $$E_\varphi + F_\varphi \cos\varphi = P,$$

(see Fig. 1)

where P is the weight of the polar column with length b (the polar semi-axis), E_0 is the weight of the equatorial column with length a (the equatorial semi-axis), F_0 is the sum of the centrifugal forces of the particles (elementary layers) of the equatorial column, E_φ is the weight of the column with latitude φ and with length c, equal to the radius-vector of the ellip-

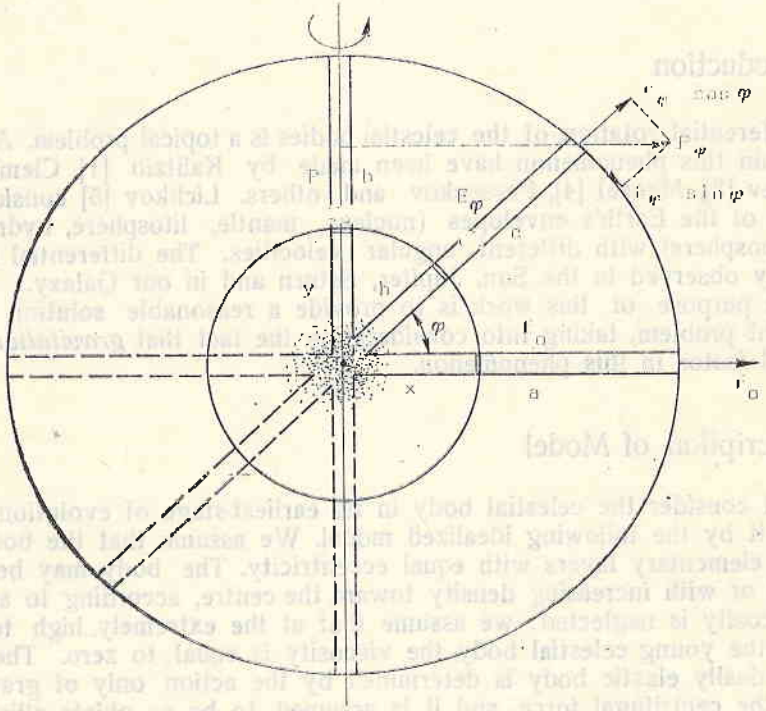

Fig. 1

soidal surface of the body: $c = ab/\sqrt{a^2 \sin^2\varphi + b^2 \cos^2\varphi}$, $F_\varphi \cos\varphi$ is the sum of the radial components of the centrifugal forces of the elementary layers of the column E_φ. The cross-section of both columns connecting the centre of the celestial body with the pole and with any point on the surface with

latitude $0° \leq \varphi \leq 90°$, is equal to unity. We must add that P, E_φ, F_φ, E_φ and $F_\varphi \cos\varphi$ are considered as *scalar* quantities.

We take the law of Legendre-Roche [8] for the density alteration in its common form:

$\bar{\varrho} = \varrho[1-\alpha(x/R)^z]$ — for alteration of the average density of the compound ellipsoids of the body;

$\varrho_s = \varrho[1-\beta(x/R)^z]$ — for alteration of the surface density of the compound ellipsoids, or of the compound elementary layers (envelopes) of the body, where ϱ is the density in the centre of the body.

At $z=0$ and $\alpha=\beta$ the body is homogeneous. Giving different values to the constants z, α and β we could represent an infinite number of celestial bodies, from homogeneous ones to such with strongly increasing density to the centre, i. e. with an inner structure similar to Roche's model.

We express the condition of equilibrium (2) of the celestial body by the following integral equation:

$$(3)\qquad \int_0^c G\frac{(4/3)\pi x^2 y\varrho[1-\alpha(h/c)^z]\varrho[1-\beta(h/c)^z]}{h^2}dh+\int_0^c \omega_h^2 h\cos^2\varphi\varrho[1-\beta(h/c)^z]\,dh$$

$$=\int_0^b G\frac{(4/3)\pi x^2 y\varrho[1-\alpha(y/b)^z]\varrho[1-\beta(y/b)^z]}{y^2}dy,$$

where x and y are the semi-axes of the attracting compound ellipsoid, h is the distance from the centre of the body to the surface of the attracting ellipsoid at latitude φ; $h=xy/\sqrt{x^2\sin^2\varphi+y^2\cos^2\varphi}$, ω_h is the angular velocity of the elementary zonal layer at a distance h from the centre, with latitude φ. The expression

$$(4/3)\pi x^2 y\varrho[1-\alpha(h/c)^z]=(4/3)\pi x^2 y\varrho[1-\alpha(y/b)^z],$$

in equation (3), is the mass of the attracting ellipsoid and the expression $\varrho[1-\beta(h/c)^z]dh=\varrho[1-\beta(y/b)^z]\,dy$ is the mass of the elementary layer in columns c and b. The equalities $h/c=y/b=x/a$ in the above expressions follow from the equality of the eccentricity of the elementary ellipsoidal layers (envelopes) of the body: $\sqrt{(a^2-b^2)/a^2}=\sqrt{(x^2-y^2)/x^2}$.

In equation (3) the attraction of the elementary layer in the columns is expressed simply by Newton's law of gravitation, but with sufficient exactness, as the attracting mass of rapidly rotating celestial bodies is assumed to be concentrated toward the centre, and the form of slowly rotating celestial bodies is almost a spherical one. This is confirmed by the accuracy of the final results.

The following proportion obviously exists with the homogeneous celestial body:

$$(4)\qquad \frac{\omega_0^2 a}{\omega_0^2 x}=\frac{G(4/3)\pi a^2 b\varrho(1-\alpha)/a^2}{G(4/3)\pi x^2 y\varrho(1-\alpha)/x^2},$$

which expresses the equality of the ratios of the centrifugal and gravitational accelerations at the surface and at any distance to the centre of the

body. Here the centrifugal force and the attraction are changing linearly to the centre, where they are equal to zero. Proportion (4) expresses the inner condition of equilibrium of the homogeneous celestial body.

For a celestial body presented by our idealized model with increasing density to the centre, according to Legendre-Roche's law, however, proportion (4) should take the form

$$\frac{\omega_0^2 a}{\omega_x^2 x} = \frac{G(4/3)\pi a^2 b\varrho(1-\alpha)/a^2}{G(4/3)\pi x^2 y\varrho[1-\alpha(x/a)]^2/x^2}, \tag{5}$$

as for the inner equilibrium of such a body the centrifugal force and the attraction to the centre must also change with the distance to an equal degree. Here $\omega_x > \omega_0$.

Proportion (4) appears as a particular case of proportion (5). Actually, at $z=0$ and $y=xb/a$ we have $\omega_x=\omega_0$.

At latitude φ proportion (5) has the following form:

$$\frac{\omega_\varphi^2 c\cos\varphi}{\omega_h^2 h\cos\varphi} = \frac{G(4/3)\pi a^2 b\varrho(1-\alpha)/c^2}{G(4/3)\pi x^2 y\varrho[1-\alpha(h/c)^2]/h^2}, \tag{6}$$

where ω_φ is the angular velocity of the elementary zonal layer on the surface of the body, with latitude φ.

From the equalities $(a^2-b^2)/a^2=(x^2-y^2)/x^2$, $c=ab/\sqrt{a^2\sin^2\varphi+b^2\cos^2\varphi}$, $h=xy/\sqrt{x^2\sin^2\varphi+y^2\cos^2\varphi}$ and proportion (6) we have: $x^2=y^2a^2/b^2$, $h^2=c^2y^2/b^2$, $y=hb/c$ and $\omega_h^2=\omega_\varphi^2(c^2-ah^2)/(c^2-ac^2)$.

Substituting the above values of x^2, h^2, y and ω_h^2 in equation (3), followed by simplification and integration, we obtain

$$\frac{G(4/3)\pi a^2 b\varrho(1-\alpha)}{c} + \omega_\varphi^2 c^2\cos^2\varphi = \frac{G(4/3)\pi a^2 b\varrho(1-\alpha)}{b}, \tag{7}$$

where $\varrho(1-\alpha)$ is the average density of the body.

Introducing the mass of the celestial body, we obtain

$$GM/c + \omega_\varphi^2 c^2\cos^2\varphi = GM/b, \tag{8}$$

from where

$$t_\varphi = 2\pi c\cos\varphi\sqrt{\frac{cb}{GM(c-b)}}, \tag{9}$$

where $t_\varphi = 2\pi/\omega_\varphi$ is the rotational period of the elementary zonal layer at a distance c from the centre, at latitude φ.

2. The same result (9) is also obtained from the equation

$$V_\varphi + U_\varphi = V_p, \tag{10}$$

which at $V_p=\text{const}$ describes an equipotential surface. Here V_φ is the inner gravitational potential, in our model, of a point on the surface with latitude φ, i. e. the work for the transport of unit mass from the centre to the sur-

face with latitude φ which is different from $\int_c^\infty \frac{GM}{h^2}dh$, V_p is the inner gravitational potential of the pole which is also different from $\int_b^\infty \frac{GM}{y^2}dy$, and U_φ is the potential of the centrifugal force at latitude φ, at the corresponding acceleration of the rotation to the centre.

Equation (10) which also expresses the condition of equilibrium of the celestial body, in our model, can be presented in the following integral form:

$$(11)\qquad \int_0^c \frac{G(4/3)\pi x^2 y\varrho\,[1-\alpha(h/c)^2]}{h^2}\,dh+\int_0^c \omega_h^2 h\cos^3\varphi\,dh$$

$$=\int_0^b \frac{G(4/3)\pi x^2 y\varrho[1-\alpha(y/b)^2]}{y^2}\,dy.$$

From Equation (11) we obtain, in a similar way, formula (9).

Equations (2) and (10) are equivalent. Newton's concept of "weight" of the column, expressed as $E_\varphi - F_\varphi\cos\varphi$, corresponds to the inner potential at the same latitude, namely: $V_\varphi + U_\varphi$.

3. In our model, Newton's condition of equilibrium (2) can be expressed as follows:

$$(2')\qquad E_\varphi/n+F_\varphi\cos\varphi/n = P/n,$$

where $n\geq 1$. At $n\to\infty$ we can write

$$(2'')\qquad \frac{GM(c/n)\varrho_s}{c^2}+\frac{4\pi^2 c\cos^2\varphi(c/n)\varrho_s}{t_\varphi^2}=\frac{GM(b/n)\varrho_s}{b^2},$$

or $$(2''')\qquad GM/c+4\pi^2c^2\cos^2\varphi/t_\varphi^2=GM/b,$$

from where formula (9) is directly obtained.

Formula (9) describes the differential rotation of the celestial bodies in our model.

4. Particular Cases of the Law (9)

At $\varphi = 0°$ formula (9) takes the form

$$(12)\qquad t_0 = 2\pi a\sqrt{\frac{ab}{GM(a-b)}}.$$

Formula (12) can also be written as:

$$(a-b)/b = F/E,$$

where $F=\omega_0^2 a$ and $E=GM/a^2$, i. e. the *second* flattening of the celestial body is equal to the ratio of the centrifugal and gravitational accelerations, measured at the equator.

Similar results had been obtained by.
Newton: $(a-b)/a=5F/4E$ and
Huygens: $(a-b)/a=F/2E$ [7].

It is very important to note here that formula (12) can be obtained directly from the proportion

$$GM/r^2-GM/a^2=k\omega_0^2 a,$$

at $k=1$ and $r^2=ab$, where r is the radius of the ideally elastic celestial body at $\omega=0$. The relation $r=\sqrt{ab}$ is a consequence from Hooke's law and can be demonstrated experimentally, by axial rotation of an elastic and isotropic sphere.

At $(a-b)/a=1/2$ formula (12) takes the form

$$t_0=2\pi a\sqrt{\frac{a}{GM}}. \tag{14}$$

Formula (14) is the mathematical expression of Kepler's third law, for circular orbits. Actually, the equatorial particles of some stars from the early spectral classes B, A and F, which have very rapid axial rotation and in which the centrifugal force at the equator is almost equal to the attraction, are rotating as small planets, according to (14). The flattening $(a-b)/a$ of these stars must be almost equal to 1/2.

5. Verification of the Results

At the following values of the mass and semi-axes of the Earth (considered ideally elastic, as a whole): $M=5.98\times10^{27}$ g, $a=6378.245\times10^5$ cm, and $b=6356.863\times10^5$ cm (the ellipsoid of Krassovsky), formula (12) gives the following value for the rotational period of the Earth (more exactly for the period of the earth-crust): $t=87384$ s $=24.27$ h, with a relative error of about 1.4 per cent. At the same values of M, a and b of the Earth, Newton's theorem gives $t=27.18$ h, and that of Huygens gives $t=17.19$ h.

Formula (12) gives the rotational periods of the other planets as well, at the correct values of their masses and semi-axes. It appears to be the most exact, compared with the similar results of Newton, Huygens, Claitaut [7] and that of Radau — Darwin [9] which is quite unfit for the planets of the Jupiter type.

As the density of the Earth increases toward the centre, where the temperature is higher and the viscosity lower, we should have, according to (12) an acceleration of the rotation of its inner layers. This is in agreement with the conclusions of Munk and Macdonald [10] and of Lichkov [5].

At the following values for the mass, the equatorial radius and the rotational period at the equator of the Sun, namely: $M=1.99\times10^{33}$ g, $a=695500\times10^5$ cm, and $t_0=25\times86164$ s, formula (12) gives the following value for the polar radius of the Sun: $b=695485\times10^5$ cm. At these values for a and b we obtain $(a-b)/a=2.15\times10^{-5}$. It is interesting to note that our theoretically determined value for the oblateness of the Sun is of the same order as that of Dicke: 5×10^{-5} [11], found experimentally.

At the following value for the density in the centre of the Sun: $\varrho = 120$ g/cm^3 [4], formula (12) gives a significant acceleration of the rotation of the inner layers of the Sun. This is in agreement with the conclusions of Dicke [11], Roxburgh [12], Fessenkov and other scientists that the inner layers of the Sun rotate more rapidly than the outer layers.

The mechanical energy of the differentially rotating layers of the celestial body is no doubt turning, at the friction between the layers, into thermal and other kinds of energy. This enormous source of energy must be taken into consideration in the solution of some astrophysical and planetary problems. For example, the total thermal flux from Jupiter is 2.5 times that which the planet receives from the Sun (from measurements made by Pioneer 10). This enigmatic phenomenon can be explained by the differential rotation of Jupiter, according to (9) and (15).

At the above values for the mass and semi-axes of the Sun, represented by our ideal model, formula (9) gives the following results for the rotational periods, in days, of the zonal layers of the photosphere of the Sun:

Table 1

φ	0°	30°	50°	70°	80°	85°
t_φ	25.0	24.9	24.8	24.5	22.6	17.5

As can be seen from the above Table, for a celestial body whose figure is an ideal ellipsoid, with viscosity equal to zero, formula (9) gives a "polar acceleration" of rotation. Actually, analyzing the line profiles of stars on the upper main sequence, Stoeckly [2] has concluded that these stars rotate more rapidly at the pole than at the equator. This is in agreement with our theoretical results, as the viscosity of these stars, which have a very high temperature, is negligible and their figure is almost an ideal ellipsoid of rotation.

On the other hand, as also noted by Stoeckly, stars on the lower main sequence, such as the Sun, possess an "equatorial acceleration". This phenomenon, observed also at the Sun, Jupiter and Saturn [1, 13, 4] could be explained by the action (influence) of the viscosity, a factor which should be taken here into account. The influence of the viscosity is, no doubt, reflected in the change of the periods of rotation of the zonal layers, in the change of the equipotential surface of the body and, consequently, in the change of the figure of celestial body.

Taking into account the integral influence of the viscosity, formula (9) should be written in the following form, for the older celestial bodies:

$$t_\varphi = 2\pi c_x \cos\varphi \sqrt{\frac{c_x b}{GM(c_x - b)}}, \tag{15}$$

where c_x is the radius-vector of the deformed figure of the celestial body and $b = GMat_0^2/(GMt_0^2 + 4\pi^2 a^3)$, from formula (12).

Equation (15) may be written as follows:

$$4\pi^2 b \cos^2\varphi c_x^3 - GMt_\varphi^2 c_x + GMt_\varphi^2 b = 0, \tag{16}$$

where the unknown quantity is c_x.

Taking the values of Kerrington [13] for the observed rotational periods of the sun-spots and zonal layers on the photosphere of the Sun, in days, and, at the corresponding latitudes, calculate the value of c_x by (16) and the difference $c-c_x$, in kilometres, where $c=ab/\sqrt{a^2\sin^2\varphi+b^2\cos^2\varphi}$ is the radius-vector of the ideal ellipsoidal surface of the photosphere, we obtain the following results:

Table 2

φ	0°	10°	20°	30°	40°	50°	60°	70°	80°	85°	90°
t_φ	25.0	25.2	25.6	26.3	27.3	28.6	30.2	32.1	34.3	35	∞
$c-c_x$	0.0	0.2	0.6	1.13	1.78	1.4	1.32	0.76	0.32	0.18	0.0

As can be seen from Table 2, the figure of the photosphere of the Sun is outlined as a very slightly deformed ellipsoid with maximum difference of $c-c_x\simeq 1.78$ km at $\simeq\pm 40°$ from the ideal ellipsoidal surface.

As we see, the observed "equatorial acceleration" of the Sun, which is also a puzzle, comes as a direct consequence of the deformation of the equipotential surface of the photosphere, caused by the viscosity.

The results of the calculations of c_x by (16) and the difference $c-c_x$, in metres, for the Earth (earth-crust), with the accepted values of M, a, b and $t_\varphi - t_0 = 86164$ s, are given in Table 3.

Table 3

φ	0°	10°	20°	30°	40°	45°	50°	60°	70°	80°	90°
$t_\varphi = t_0$		t_0	t_0	t_0	t_0	t_0	t_0	t_0	t_0	t_0	t_0
$c-c_x$	0.0	3.0	13.5	27.4	28	29	28	20	12	1.7	0.0

Table 3 shows that the *common* figure of the Earth is outlined as a slightly deformed spheroid with maximum difference $c-c_x\simeq 29$ metres at $\simeq\pm 45°$ from the ellipsoidal surface. As is well known, the average deviation of the so-called normal spheroid of Clairaut from the surface of the two-axial ellipsoid of rotation, with the same semi-axes, is about 20 m [14].

All the above calculations are done in the system of units CGS.

The stratification (formation of bigger zonal layers) of the celestial body in the course of evolution, from the surface to the centre and from the equator to the pole is due, as we assume, to the viscosity and to the tendency of the particles of the body to rotate according to law (9). Such zonal layers are clearly seen in the atmosphere of Jupiter and Saturn, rotating with different angular velocities. In the Earth's upper atmosphere we also observe zonal layers and "jet streams", circulating from west to the east with a greater angular velocity.

Thanks to the great viscosity, the particles of the Earth's crust are rotating with equal (or almost equal) angular velocity. In the atmosphere of the Earth and that of the other planets, however, where the viscosity is much smaller, we have differential rotation. In the upper atmosphere of the

Earth, where the specific factors in the low atmosphere (relief, unequal heating of the Earth's surface on land and sea, at the equator and at the poles) do not play any role, we observe zonal winds of high velocity. It has been discovered by artificial satellites that the atmosphere at a height of 200–300 km rotates 1.3 times more rapidly than the Earth's crust [15]. A similar phenomenon is observed in the solar atmosphere [13]. We also know that the velocity of the uninterrupted general transport of the air and vapour masses from west to the east is higher than the velocity of the Earth's crust rotation. All these phenomena cannot be explained by the thermal factor only. Obviously, at the regular rotation of the zonal layers in the upper atmosphere of the planets and the stars, according to (9) and (15), the main role is played by gravitation, as at the orbital circulation of the planets, according to Kepler's laws.

Formula (15) can be written as follows:

$$V_\varphi^* = \sqrt{\frac{GM(c_x - b)}{c_x b}}, \tag{16}$$

where V_φ^* is the linear velocity of the zonal layers and zonal winds.

$$V^*_{\text{relative}} = V_\varphi^* - 465 \text{ m/s} \times \cos\varphi.$$

6. Conclusion

The result (9), obtained by different methods of research, which very well describes the differential rotation of the young celestial bodies, can be interpreted as a common law operating under ideal conditions, in which gravitation only is playing the main role. The particular cases (12) and (14) of this law confirm its veracity and importance. Formula (12) is most simple and most exact, compared with the similar classical and contemporary results. The precision with which it gives the rotational period of the Earth can be explained by the great elasticity of the Earth, as a whole.

The result (15), where the influence of the viscosity is taken into account, could be successfully used, as we have shown, for determination of the common figure of the older celestial bodies, and for the explanation of their specific differential rotation.

We could give by means of (9) and (15) or (16) a qualitative explanation of the *general circulation* and the *dynamics* of the upper atmosphere of the Earth and other planets, assuming that the flattening $(a-b)/a$ of their compound envelopes increases with the height.

The experts in this subject could see, I believe, the significance of the results obtained in astrophysics and geophysics.

Acknowledgements. I am very grateful to Dr. M. Gogoshev and to Professor K. Serafimov for their kind support and to engineer Tihomir Dimitrov for valuable discussions in the course of this work.

References

1. Kalitzin, N. S. On the rotation and the figure of celestial bodies. — Astronomische Nachrichten, 286, 1962, 4, 157.
2. Clement, M. J. Differential rotation in stars on the upper sequence. — Astroph. Journal, 156, 3, Part 1, 1963.
3. Рубачев, Б. М. Проблемы солнечной активности. М., 1964, 289.
4. Menzel, H. D. Our Sun. Harvard Univ. Press, Cambridge, Mass., 1959, 102, 103.
5. Личков, Б. Л. Земля во Вселенной, геогр. серия. М., Мысл, 1964, 156.
6. Шкловский, И. С. Звезды, их рождение, жизнь и смерть. М., Наука, 1975, 315, 313.
7. Clairaut, A. Théorie de la figure de la Terre, tirée des principes de l'hydrostatique. Moscow, Acad. Sci. USSR, 1947, 263, 267 (in Russian).
8. Магницкий, В. А. Внутреннее строение и физика Земли. М., Недра, 1965, 266.
9. Kuiper, G. P., B. M. Middlehurst. Planets and satellites. The Univ. of Chicago Press, 1961, 152.
10. Munk, H. W., Macdonald, T. F. Gordon. The Rotation of the Earth. Moscow, Mir, 1964, 164, 307 (in Russian).
11. Dicke, R. H. Gravitation and the Universe, American Philosophical Society, Philadelphia, 1970, 52.
12. Roxburgh, I. W. Agenda and draft reports. — IAU. Prague, 1967, 29.
13. Шаронов, В. В. Солнце и его наблюдения. М., Гостехиздат, 1953, 34, 36.
14. Тверской, П. Н. Курс по геофизика. С., Наука, 1951, 63, 34.
15. Наблюдения на изкуствените спътници на Земята. С., БАН, 1968, 7, 141.

О дифференциальном вращении и фигуре небесных тел

Т. Р. Тилчев

(Резюме)

В этой статье дается теоретическое обоснование гипотезы автора о дифференциальном вращении небесных тел, опубликованной в журнале „Астрономише Нахрихтен" профессором Никола Ст. Калициным [1]. Предложено оригинальное решение проблемы дифференциального вращения и фигуры небесных тел. Сформулированный общий закон действует при идеальных условиях. Тем не менее этот закон довольно хорошо описывает наблюдаемые явления в реальной природе. Первый частный случай этого закона сравнивается с подобными результатами Ньютона, Гюйгенса и Клеро. Второй частный случай является идентичным с третьим законам Кеплера для круговых орбит.